

Maneuverability of a Container Ship under Various Loading Conditions

(様々な荷状態におけるコンテナ船の操縦性能に関する研究)

ANDI NADIA HIMAYA

Doctor Thesis

Submitted in Fulfillment of the Requirements
for the Degree of Doctor of Philosophy

June 2023

Graduate School of Advanced Science and Engineering
Transportation and Environmental Systems Program
Hiroshima University, Japan

ABSTRACT

A container ship navigates under various loading conditions in the daily voyage. Although the trim and draft effects on the resistance and propulsive performances are of concern, more research is required on their effect on the maneuverability. It is important for the ship control and safe navigation. In this study, KCS container ship was the subject ship which had 3600 TEU loading capacity. The model ship with the 1/75.24 scale ratio was used for the experiment. The five types of loading conditions were studied, i.e., full-load draft/even keel, shallow draft/even keel, deep draft/even keel, full-load draft/bow trim and full-load draft/stern trim. They were determined as not-significant different loading conditions, which might have been commonly experienced by container ships due to the different volume and arrangement of containers in daily voyages. This study aims to investigate the effect of various loading conditions, i.e., various draft and trim conditions, on the container ship's maneuverability by conducting free-running tests to measure the maneuvering motions and captive model tests to clarify the hydrodynamic forces. Every test was under those five loading conditions and comparative analysis was performed. CFD was conducted to explain the mechanism of the change of the course stability. The simulation-based study was also presented to study the maneuvering motion and course-keeping performance under wind disturbance.

ACKNOWLEDGEMENTS

First and foremost, the author wishes to express her highly gratitude to her academic supervisor, Associate Prof. Dr. Masaaki Sano, for his valuable guidance, advice and encouragement during the period of 5 years living and studying in Hiroshima University, everything is deeply appreciated. The author appreciates Prof. Dr. Hironori Yasukawa knowledge and advice in completing the author's master and doctoral course.

The author also wants to take the opportunity to thank colleagues in the laboratory of Department of Marine Transportation and Environmental Systems Engineering, especially to Mr. Okuda, Mr. Hachiya, and Mr. Suzuki for their assistance, guides, and patience throughout the years. The author also wishes to thank friends and colleagues in University, Ms. Htut, Ms. Du, and Ms. Song, for their friendship and patience for 5 years studying in Hiroshima University.

Last but not least, the author wants to thank her family for their love, support, patience and care throughout the years in Japan.

List of Contents

	Page
ABSTRACT	i
ACKNOWLEDGEMENTS	ii
List of Figures	vi
List of Tables	x
Abbreviations	xi
Nomenclatures	xii
1 Introduction	1
1.1 Background	1
1.2 Objective and outline of the study	3
2 Maneuvering Mathematical Model of Ship	5
2.1 Coordinate systems	5
2.2 Motion equations	5
2.3 Formulation of hydrodynamic forces and moments	6
2.3.1 Hull force	7
2.3.2 Propeller force	7
2.3.3 Rudder force	8
2.3.4 Wind force	9
3 Subject Ship	11
3.1 Principal dimensions of the subject ship	11
3.2 Loading conditions of the subject ship	12
3.3 Design of the over deck objects in the real scale	13
3.4 Estimation of wind forces and moments in the real scale	16
4 Experimental Study: Free-running Model Test	18
4.1 Outline of free-running model test	18
4.2 Turning test results	19
4.2.1 Turning trajectory and its indices	19
4.2.2 Time series of motions	22

4.3	Zig-zag test results	23
4.3.1	Times series of motion	23
4.3.2	Overshoot angles	24
5	Experimental Study: Captive Model Test	26
5.1	Outline of captive model tests	26
5.2	Rudder force test results	27
5.2.1	Maneuvering force by steering	27
5.2.2	Parameters for rudder normal force	29
5.2.3	Hull and rudder interaction coefficients	30
5.3	Flow straightening results	32
5.4	OTT and CMT results in Hiroshima University tank	33
5.4.1	Maneuvering forces	33
5.4.2	Linear hydrodynamic force derivatives for ship	35
5.4.3	Discussion on course stability	36
5.5	OTT and CMT results in JFREA tank	40
5.5.1	Hydrodynamic force derivatives for hull	40
5.5.2	Effective wake fraction in maneuvering motion	43
6	Numerical Analysis: Mechanism of Course Stability	45
6.1	Outline of CFD application	45
6.1.1	Computational domain and boundary conditions	45
6.1.2	Calculation condition	47
6.2	Validation of the hydrodynamic force linear derivatives	47
6.3	Effect of draft on hydrodynamic forces and course stability	48
6.3.1	Longitudinal distribution of the sway force	48
6.3.2	Visualization of flow and pressure field	49
6.4	Effect of trim on hydrodynamic force and course stability	51
6.4.1	Longitudinal distribution of the sway force	51
6.4.2	Visualization of flow and pressure fields	52
7	Simulation Study: Maneuvering Simulation	55
7.1	Parameters and coefficients used for simulations.	55
7.2	Validation of the maneuvering mathematical model	56

7.3	Real-scale maneuvering simulations	60
7.3.1	Straight motion	60
7.3.2	Turning motion	61
7.3.3	Zig-zag maneuver	64
8	Simulation Study: Course-keeping Simulation Under Wind Disturbance	66
8.1	No true wind condition	66
8.2	Influence of the ship speed and true wind angle	67
8.3	Influence of trim and draft conditions	68
8.4	PD control designed to maintain the straight course	70
8.5	Equilibrium state under wind	70
8.5.1	Influence of the apparent wind speed under the constant ship speed	71
8.5.2	Influence of the ship speed under the constant apparent wind speed	72
8.5.3	Influence of loading condition under the constant ratio of the apparent wind and ship speeds	73
8.5.4	Discussion of the equilibrium state based on the polar chart	75
9	Conclusion	79
	References	82
	Appendix A	86
	Appendix B	87

List of Figures

	Page
2.1 Coordinate systems for maneuvering of a ship	5
3.1 Side view of the 1/75.24 KCS model	11
3.2 Body plan of KCS ship	12
3.3 Image of KCS with loading containers: S-EK (left), EK (middle), EK with visualization of the containers inside (right)	14
3.4 Weight of containers on each tier at each bay for EK	15
3.5 Comparison of the weight distribution of containers in the longitudinal direction among the five loading conditions	15
3.6 Estimated wind force and moment of the subject ship with respect to the apparent wind angle	17
4.1 Photo of the marine dynamic basin for free-running model test	18
4.2 Trajectories during the $\pm 35^\circ$ test on the draft (left) and trim series (right)	20
4.3 Comparison of the advance (left) and tactical diameter (right) between $\pm 35^\circ$ T for each loading condition	20
4.4 Advances and tactical diameters during $\pm 35^\circ$ T: draft series (top) and trim series (bottom) ·	21
4.5 Time series of the non-dimensional yaw rate, hull drift angle and roll angle in $+35^\circ$ T: draft series (top) and trim series (bottom)	22
4.6 Time series of the heading and rudder angles during $\pm 10^\circ$ Z: draft series (top) and trim series (bottom)	24
4.7 Time series of the non-dimensional yaw rate, hull drift angle and roll angle in $+10^\circ$ Z: draft series (top) and trim series (bottom)	24
4.8 1 st and 2 nd overshoot angles for the $\pm 10^\circ$ Z test: draft series (left) and trim series (right) ···	25
5.1 Non-dimensional sway force and yaw moment in the rudder force test depending on the draft series (top) and the trim series (bottom)	28
5.2 Y'_δ (left) and N'_δ (right) among draft-series and trim-series conditions	29
5.3 Comparison of ε , κ and k_x in draft series (left) and trim series (right)	29
5.4 Analysis result of rudder normal force coefficient (F'_N) for EK	30
5.5 Comparison of t_R , a_H and x'_H in draft series (left) and trim series (right)	31

5.6	Analysis of hull-rudder interaction coefficients for EK	32
5.7	Comparison of γ_R in draft and trim series	33
5.8	Analysis results of lateral inflow velocity to rudder for EK	33
5.9	Non-dimensional sway force and yaw moment for pure sway motion (top) and pure yaw motion (bottom) depending on draft	34
5.10	Non-dimensional sway force and yaw moment for pure sway motion (top) and pure yaw motion (bottom) depending on trim	35
5.11	Linear hydrodynamic force derivatives, course stability index, and its component terms: draft series (left) and trim series (right)	40
5.12	Comparison X'_H, Y'_H and N'_H between measured data and the fitting line for EK	41
5.13	Comparison of derivatives of lateral force (Y) and yaw moment (N) in draft series (upper) and trim series (bottom)	42
5.14	Comparison of Y'_ϕ and N'_ϕ in the draft series (left) and trim series (right)	43
5.15	Comparison of w_{P0} in draft and trim series	44
6.1	Computational domain (left: Bird's eye view; right: Enlarged view of the hull at the midship)	46
6.2	Longitudinal distribution of the sway force for the pure sway case of $\beta = 6^\circ$ depending on the draft	49
6.3	Contours of the pressure coefficients over the hull surface for the pure sway case of $\beta = 6^\circ$ depending on the draft	50
6.4	Illustration of the area aside the hull where the streamlines pass through (draft series)	50
6.5	Streamlines colored by the flow speed passing near the fore shoulder of the face-side hull in the case of $\beta = 6^\circ$ depending on the draft	51
6.6	Longitudinal distribution of the sway force for the pure sway case of $\beta = 6^\circ$ depending on the trim	52
6.7	Contours of the pressure coefficients over the hull surface for the pure sway case of $\beta = 6^\circ$ depending on the trim	53
6.8	Illustration of the area aside the hull where the streamlines pass through depending on the trim	53
6.9	Streamlines colored bby the flow speed passing around the bilge of the back side in the case of $\beta = 6^\circ$ depending on the trim	54

7.1	$\pm 35^\circ$ turning trajectories of each loading condition	57
7.2	Comparison of $\pm 35^\circ$ turning trajectories among draft-series conditions (upper) and trim-series (lower) between the free-running experiment and simulation	58
7.3	Comparison of A_D/L and D_T/L in $\delta = \pm 35^\circ$ turning	58
7.4	Comparison of time histories of ψ and δ of $10^\circ/10^\circ$ zig-zag maneuvers between experimental and calculation	59
7.5	Comparison of time histories of ψ and δ of $-10^\circ/-10^\circ$ zig-zag maneuvers between experimental and calculation	59
7.6	Comparison of overshoot angles of $\pm 10^\circ$ zig-zag maneuvers	60
7.7	Trajectories of $\delta = \pm 35^\circ$ turning in the real scale	62
7.8	Comparison of advanced and tactical diameter of $\delta = \pm 35^\circ$ turning between the real-scale and model-scale ship	63
7.9	Time histories of the roll angle of $\delta = +35^\circ$ turning in the real scale	63
7.10	Time histories of ψ and δ of $\pm 10^\circ/\pm 10^\circ$ zig-zag maneuvers in the real scale	64
7.11	Comparison of overshoot angles of $\pm 10^\circ/\pm 10^\circ$ zig-zag maneuvers between the real-scale and model-scale ship	65
8.1	Influence of the rudder control gains on the convergence of the heading angle when keeping the course under no true wind	67
8.2	Influence of the ship speed and true wind angle on the states of EK when keeping the course under wind	68
8.3	Comparison of the states while course keeping by PD control among the draft series, i.e., EK, S-EK and D-EK under wind; $U_w = 9.26$ (m/s) and $\psi_w = 90$ ($^\circ$)	69
8.4	Comparison of the states while course keeping by PD control among the trim series, i.e., EK, TB and TS under wind; $U_w = 9.26$ (m/s) and $\psi_w = 90$ ($^\circ$)	69
8.5	Comparison of the hull drift angle, rudder angle and trajectory of EK while course keeping by the PD control for yaw motion (in black) and the PD control for yaw and lateral displacement (in red) under wind; $U_w = 9.26$ (m/s) and $\psi_w = 90$ ($^\circ$)	70
8.6	Equilibrium states of EK sailing at $U_0 = 6$ (kt) under different apparent wind speeds, i.e., $U_{aw}/U_0 = 1,2,3$	71
8.7	Equilibrium states of EK sailing at different ship speeds, i.e., 6, 12, 24 (kt), under the apparent wind speed, i.e., $U_w = 9.26$ (m/s)	72
8.8	Equilibrium state of EK, S-EK and D-EK (draft-series) and EK, TB and TS (trim-series)	

	sailing at $U_0 = 6$ (kt) under the same apparent wind speed, i.e., $U_w = 9.26$ (m/s) which corresponds to $U_{aw}/U_0 = 3$	75
8.9	Polar chart of the equilibrium states of EK, S-EK and D-EK (draft series) in various combinations of the true wind and ship speed	76
8.10	Polar chart of the equilibrium states of EK, TS and TB (trim series) in various combinations of the true wind and ship speed	77

List of Tables

	Page
3.1 Principal dimensions of KCS	11
3.2 Principal dimensions of propeller and rudder	12
3.3 Loading conditions for the model-scale KCS used in the experiment	13
3.4 Loading conditions for the real-scale KCS	13
3.5 Position of the center of the gravity, \overline{GM} and radius of gyration in the roll and yaw moments	16
3.6 Representative parameters related to the windage area for each loading condition	16
4.1 Model self-propulsion points under the different loading conditions	19
4.2 Advances and tactical diameters during the $\pm 35T$ test	19
4.3 Overshoot angle for the $\pm 10Z$ tests	25
5.1 Thrust deduction factor	26
5.2 Rudder force coefficients	28
5.3 ε, κ and k_x in five different loading conditions	30
5.4 Hull-rudder interaction coefficients in five different loading conditions	31
5.5 Flow straightening coefficient (γ_R) in five different loading conditions	32
5.6 Linear hydrodynamic force derivatives defined at midship	36
5.7 Linear hydrodynamic force derivatives defined at the center of gravity, course stability index and its components terms	37
5.8 Hull hydrodynamic derivatives on maneuvering in five different loading conditions	41
5.9 Hull hydrodynamic derivatives related to heel angle ϕ in five different loading conditions	43
5.10 Parameters for expressing wake fraction in maneuvering motion	44
7.1 Radius of roll gyration including added mass component in five different loading conditions for the model-scale ship	56
7.2 Added mass coefficients in five different loading conditions	56
7.3 Number of propeller revolution (n_p) in five different loading conditions	61
B.1 Each coefficient for every variable	89

Abbreviations

AIS	Automatic Identification System
CAL	Calculation
CFD	Computational Fluid Dynamic
C.G	Centre of gravity
CMT	Circular Motion Test
DOF	Degree of Freedom
D-EK	Deep – Even Keel, with deep draft
EK	Even Keel in full load condition
FEU	Forty-feet Equivalent Unit
IIHR	Iowa Institute of Hydraulic Research
IMO	International Maritime Organization
ITTC	International Towing Tank Conference
JFREA	Japan Fisheries Research Education and Agency
KCS	KRISO Container Ship
MMG	Maneuvering Modeling Group
MSC	Maritime Safety Committee
MSPP	Model self-propulsive performance
OSA	Overshoot Angle
OTT	Oblique Towing Test
PCC	Pure Car Carrier
PD	Proportional Derivative
RHS	Right-hand side
S-EK	Shallow – Even Keel, with shallow draft
TB	Trim by Bow
TEU	Twenty-feet Equivalent Unit
TS	Trim by Stern
VLCC	Very Large Crude Carrier

Nomenclatures

Greek symbols

α_R	effective inflow angle to the rudder (rad)
β	hull drift angle at midship, $\beta = \tan^{-1}(-v_m/u)$ (rad)
β_P	geometrical inflow angle to propeller
β_{0w}	hull drift angle in equilibrium
η	ratio of propeller diameter to rudder span ($= D_P/H_R$)
δ	rudder angle (rad)
δ_{0w}	rudder (check helm) angle in equilibrium
γ_R	flow straightening coefficient
Λ	rudder aspect ratio
κ	an experimental constant for expressing u_R
∇	displacement volume of ship (m^3)
ψ	ship heading (rad)
ψ_0	intial ship heading angle
ψ_{aw}, ψ_w	apparent and true wind angles
ρ	water density ($kg\ m^{-3}$)
ρ_a	air density
ϕ	roll angle
ϕ_{0w}	roll angle in equilibrium
ε	ratio of wake fraction at propeller and rudder positions ($= 1 - w_R)/(1 - w_P)$) (-)

Roman symbols

A_D	advance (m)
A_F, A_L	projected frontal and lateral windage areas
A_R	rudder area including horn (m^2)
a_H, t_R, x_H	rudder-hull interaction factors
$a_i, \gamma_{ij}, C_{CF}, C_{YLI}$	Parameters to estimates wind forces/moments
a_z	vertical acting point of added mass in sway
B	ship breadth (m)
B_R	averaged rudder chord length (m)

C_b	block coefficient
$C_{MC}, H_c, H_{BR}, A_{OD}$	parameters related to windage area
D	ship depth (m)
D_P	propeller diameter (m)
D_T	tactical diameter (m)
d	ship draft (m)
d_a	draft at after perpendicular of the ship (m)
d_f	draft at fore perpendicular of the ship (m)
F_N	rudder normal force (N)
f_a	rudder lift gradient coefficient
\overline{GM}	metacentric height (m)
g	gravitational acceleration
H_R	rudder span (m)
I_x, I_z	moment of inertial of ship roll and yaw
I_{zG}	moment of inertia of ship around the center of gravity (kg m ²)
J_P	propeller advanced ratio
J_{xx}, J_{zz}	added moment of inertia in roll and ya
K_T	propeller thrust open water characteristics
$K_{0,1,2}$	coefficients of K_T
$K_{\dot{\phi}}, K_{\dot{\phi}\dot{\phi}}$	roll damping coefficients
\overline{KG}	height of C.G. of ship from keel
k_x	flow acceleration rate due to propeller
k_{xx}, k_{zz}	radius of gyration in roll and yaw
L/L_{PP}	ship length between perpendiculars (m)
L_{OA}	ship length overall
l_R	effective longitudinal coordinate of rudder
L_{wl}	ship length waterline (m)
m	ship's mass (kg)
m_x, m_y	added mass in surge and sway
η_P	number of propeller revolution (rps)
$o - xyz$	horizontal body axis coordinate system
$o_0 - x_0y_0z_0$	space fixed coordinate system

P	propeller pitch ratio
R'_0	resistance coefficient
r	yaw rate (rad s^{-1})
\dot{r}	yaw acceleration (rad s^{-2})
S	wetted surface area of ship without a rudder and horn (m^2)
t	time (s)
t_P	thrust deduction factor
U	ship speed
U_0	initial ship speed
U_{aw}, U_w	apparent and true wind velocities
u, v_m	surge and sway velocities at midship
u_R, v_R	axial and lateral inflow velocity components to rudder, respectively (m s^{-1})
w_P	wake fraction at propeller position in maneuvering motions
w_{P0}	wake fraction at propeller position in straight moving
w_{Pmin}, C_0	coefficients of wake behaviour against β_P
X, Y, N, K	surge/sway force and yaw/roll moments
$X_{aw}, Y_{aw}, N_{aw}, K_{aw}$	wind forces and moments
X_H, Y_H, N_H	hull forces and moments
X_P	propeller
X_R, Y_R, N_R	rudder forces and moments
X'_{vr}, Y'_v, N'_r etc.	hydrodynamic force derivatives
x_G, z_G	coordinate of the center of gravity of a ship (m)
x_P, z_P	coordinate of propeller
z_H, z_R	coordinates of vertical acting point of hull and rudder forces

Chapter 1

Introduction

1.1 Background

Maneuverability is defined as the ability of a ship to change its course. It is an important factor to understand, along with some aspects, such as stability. International Maritime Organization (IMO) [1], addressed the guidelines for ship maneuver, which is recommended for every ship to improve navigation safety.

We know that marine transportation, such as container ships is the prime means of global trade. A container ship transferring numerous containers must stow them in the proper slots considering many factors, such as handling efficiency, stability, and hull strength due to weight distribution. Various algorithms, e.g., Delgado et al. [2], Chou and Fang [3], and tools e.g., Aye et al. [4], have been developed and assist with this task. Because the number of container cargo depends on the market, this can affect the displacement or draft of the ship. Optimizing the trim for improved fuel efficiency is another important consideration these days. Thus, a container ship navigates under various loading conditions (i.e., trim and draft combinations), and research is needed on the relationship between the ship's attitude and hydrodynamics. However, most previous works on trim and draft have focused on their effects on the resistance and propulsive performances. Few studies have considered their effect on maneuverability, which is important for ease of ship control and safe navigation.

Because the interest in trim is expected, many studies have not limited themselves to container ships. For example, Lyu et al. [5] presented a potential-based trim optimization method for minimizing wave-making resistance using an original hull model. Sun et al. [6] used computational fluid dynamics (CFD) to calculate model-scale resistance curves for various drafts and trims. They developed a trim optimization program converted to real-scale engine power and verified their approach by conducting a sea trial of a real 4250-TEU container ship. Gao et al. [7] and Islam and Soares [8] also used CFD to predict the resistance of a container ship. The latter obtained some insights into the trim mechanism, which they associated with the pressure distribution around the hull. Optimizing the trim can also be expected to affect the self-propulsion performance positively, and there have been studies on this topic. For example, Larsen et al. [9] performed model tests and CFD to examine the factors that affect the vessel's propulsive power under different trim conditions. Hirata et al. [10] conducted a full-scale trial

to study the trim effect on the maneuverability of an electric propulsion ship equipped with two azimuth thrusters, and it was shown that the aft trim improves the course stability. Reichel et al. [11] proposed predicting the required power under trim conditions and developed a decision support tool for the proper trim. Vasileva [12] did similar work with a very large crude carrier model as Larsen et al. [9] and discussed the effect of a bow bulb close to or intersecting the free surface. Sogihara et al. [13] conducted model tests for the various draft and trim combinations of vehicle carriers and container ships. They found that trim by the bow could reduce the brake power of a fine ship at low speed in the case of a shallow draft, but no trim condition was optimum for a full-load draft. Thus, the above studies show that the trim has been discussed mostly regarding its effect on energy efficiency or straight running. Few works have focused on the effect of the trim on maneuverability.

Meanwhile, the draft effect on the maneuverability has been discussed but commonly focused on the difference in maneuverability between the full load in service and the ballast load in sea trials. For example, Inoue et al. [14] compared the maneuvering performance between full-load and ballast-load conditions for each container ship and tanker ship through the mathematical model-based simulation. Kijima et al. [15] proposed approximation formulas for the coefficients in that mathematical model. Kose et al. [16] and Sannomiya et al. [17] also studied hydrodynamic forces and maneuvering characteristics between them, and Sannomiya et al. [18] developed a simplified formula to estimate the full-load maneuverability from the ballast-load one. Thus, previous studies mainly aimed to investigate the effect of a drastic change in the draft (i.e., from full load to ballast load) on maneuverability. However, as mentioned first, because a container ship daily experiences draft changes that are not necessarily drastic but may be sensitive, we think there is a room for a systematic study on the effect of draft on the maneuverability as well as the effect of trim.

Furthermore, few studies have been conducted on wind's effect on maneuverability. In general, the effect of wind on a ship's motion characteristics is significant. The effect of wind on maneuverability is one of the important considerations for container ships because it has a large windage area due to a large number of containers on the deck. Such as phenomenon recently happened on late March 2021, the Suez Canal obstruction accident in Egypt [19]. It is said that a strong wind was a significant cause of the course deviation and grounding. For example, Zhou et al. [20] quantitatively analysed and estimated the impacts of external conditions (wind and current) on ship behavior in ports and waterways based on AIS data. Regarding studies on ships' motion under the wind, Yoshimura and Nagashima [21] discussed

the maneuvering motion of a PCC through the free-running model test and simulation in the uniform wind. Hasegawa et al. [22] discussed the comparison of the course-keeping ability of a PCC when installing a normal rudder and a high-lift rudder in windy conditions. Nagarajan et al. [23] developed the mathematical model of a VLCC and carried out full-scale course-keeping simulations under gusting wind conditions. Paroka et al. [24] also simulated to discuss the wind effect on the ship maneuverability of an Indonesian ro-ro ferry in a steady wind. Im and Tran [25] estimated the equilibrium state of the behavior of a training ship under the influence of wind. Some other numerical studies have also been performed so far (e.g., [26],[27]). Since a container ship has a large windage area due to the large number of containers on the deck, it has also been a major research target. Andersen [28] investigated a post-Panamax container ship through a series of wind tunnel tests. Janssen [29] presented RANS CFD simulations of wind loads on a container ship and validated them with Andersen [28]. Seok and Park [30] also numerically studied the effect of the presence of the superstructure on the resistance, trim, and sinkage of an 8000 TEU-class container ship. As seen from those references, although there have been many studies so far, most studies have only focused on one loading condition, and no studies have discussed the effect of the combination of the loading condition and wind on manoeuvring performance. It has become interesting to discuss both combinations and their effect on the maneuverability furthermore.

1.2 Objective and Outline of the Study

The objective of this study is to determine the effect of trim and draft combinations on the container ship's maneuverability and the influence of wind disturbances on maneuverability. Since the authors found that the change of course stability was highly sensitive to the loading conditions, it is interesting to change the course-keeping performance, which is the most fundamental factor for navigation safety, by considering both hydrodynamic forces acting on the hull underwater and aerodynamic force on the hull/containers above water simultaneously.

Firstly, Chapter 2 described the KCS container ship used as a subject ship along with the coordinate system used and the formulation to be solved for the hydrodynamic forces and moments. In Chapter 3, the principal dimensions of the KCS container ship, along with the installed propeller and rudder, were listed. Five loading conditions were set to present the draft conditions/draft series and trim conditions/trim series. KCS was designed to load an 1800 FEU dry container, which is also illustrated; wind force is described in this chapter.

In order to achieve the objective, free-running model tests were conducted in the Marine Dynamic Basin at the Fisheries Technology Institute of Japan Fisheries Research and Education Agency (JFREA), Japan, as described in Chapter 4. Continuation from Chapter 4, captive model tests were conducted to grasp the hydrodynamic force characteristics and described in Chapter 5. The model tests were conducted in the towing tank at Hiroshima University and the marine dynamic basin of JFREA.

In Chapter 6, a numerical analysis of CFD was performed to understand the mechanism of the course stability. The hydrodynamic forces acting on the ship with propeller and rudder in pure sway and yaw motions were calculated by CFD, which is supplied with OpenFOAM ver.5.0 by the open-source CFD toolbox. The effect of draft and trim conditions on maneuverability was explained by the longitudinal distribution with a hull drift angle, followed by consideration of flow and pressure fields.

In Chapter 7, a simulation study for maneuvering was discussed. The parameters used for the maneuvering simulations are listed, and the mathematical model is validated. Continuously, in Chapter 8, a simulation study for the course-keeping performance under wind is discussed here. The course-keeping simulation was executed with self-propulsion considering with or without the wind disturbance. The equilibrium state under wind disturbance is discussed as well. Finally, the conclusion of this research is given in Chapter 9.

Chapter 2

Maneuvering Mathematical Model of Ship

2.1 Coordinate systems

The coordinate systems used in this study are shown in Figure 2.1. The space-fixed coordinate system is denoted as $o_0 - x_0y_0z_0$, where the x_0y_0 plane coincides with the still water surface and the z_0 -axis is vertically downward. The horizontal body axis coordinate system is denoted as $o - xyz$ where the origin o is located at the midship on the still water surface, the x -axis is considered towards the bow, the y -axis towards the starboard, and the z -axis vertically downward. The heading angle ψ is defined as the angle between the x_0 and x -axis, δ is the rudder angle, ϕ is the roll angle and r is the yaw rate. G represents the position of center of gravity of the ship, which is expressed as $(x_G, 0, z_G)$. u and v_m denote the velocity components at the midship for surge and sway in x and y directions, respectively. β is the drift angle at the midship, and U is the total velocity calculated by $\sqrt{u^2 + v_m^2}$.

Regarding wind terms, U_w and U_{aw} are the true and apparent wind velocities, respectively. ψ_w and ψ_{aw} are defined as the true and apparent wind angles from the x_0 -axis.

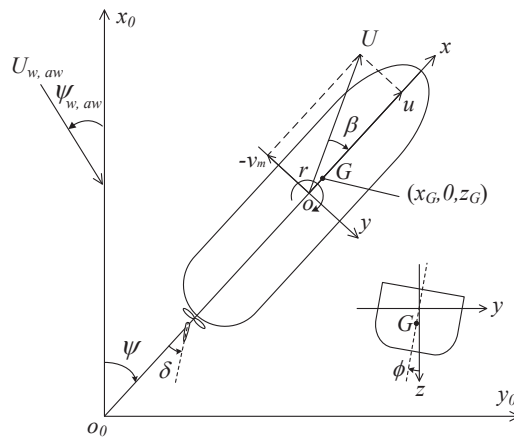


Figure 2.1: Coordinate systems for maneuvering of a ship

2.2 Motion equations

Mathematical models for maneuvering based on the MMG-model framework. The motion equations with respect to the surge, sway, yaw, and roll motions are defined in the equations as follows.

$$\left. \begin{aligned} (m + m_x)\dot{u} - (m + m_y)v_m r - mx_G r^2 + mz_G r \dot{\phi} &= X \\ (m + m_y)\dot{v}_m(m + m_x)ur + x_G m \dot{r} - (m_y a_z + mz_G)\ddot{\phi} &= Y \\ (I_{zz} + J_{zz} + mx_G^2)\dot{r} + mx_G(\dot{v}_m - z_G \ddot{\phi} + ur) &= N \\ (I_{xx} + J_{xx} + mz_G^2)\ddot{\phi} - (m_y a_z + mz_G)\dot{v}_m - mz_G(x_G \dot{r} + ur) &= K \end{aligned} \right\} \quad (2.1)$$

where m denotes the ship mass. I_{xx} and I_{zz} denotes the moment inertia for the roll and yaw around the midship, respectively. m_x and m_y denotes the added masses of the x -axis direction and y -axis direction, respectively. J_{xx} and J_{zz} denotes the added moment of inertia for yaw and roll moment, respectively. a_z is the vertical acting point of the lateral added mass component m_y . Moreover, in the right-hand side, X is the surge force without the added mass component. Y is the lateral force without the added mass component. N is the yaw moment around the midship without the added moment of inertia component, and K is the roll moment around the x -axis without the added moment of inertia component. Additionally, the dot (\cdot) notation indicates the ordinary differential with respect to the time (t).

2.3 Formulation of hydrodynamic forces and moments

The hydrodynamic forces and moments are formulated as follows:

$$\left. \begin{aligned} X &= X_H + X_R + X_P + X_A \\ Y &= Y_H + Y_R + Y_A \\ N &= N_H + N_R + N_A \\ K &= -Y_H z_H - Y_R z_R - mg\overline{GM}\phi + K_{\dot{\phi}}\dot{\phi} + K_{\phi\dot{\phi}}\dot{\phi}|\dot{\phi}| + K_A \end{aligned} \right\} \quad (2.2)$$

Each of the subscripts in the right-hand side H , P , R , and A denote the hull, propeller, rudder, and wind respectively. In terms of the roll moment, the first and second terms denote the roll moment owing to the hull sway force and rudder normal force where z_R and z_H are the vertical acting points of them from G . $K_{\dot{\phi}}$ and $K_{\phi\dot{\phi}}$ are the roll damping coefficients.

2.3.1 Hull force

Surge force (X_H), lateral force (Y_H) and yaw moment (N_H) around midship acting on ship hull could be express as follows:

$$\left. \begin{aligned} X_H &= (1/2)\rho LdU^2 X'_H(v'_m, r', \phi) \\ Y_H &= (1/2)\rho LdU^2 Y'_H(v'_m, r', \phi) \\ N_H &= (1/2)\rho L^2 dU^2 N'_H(v'_m, r', \phi) \end{aligned} \right\} \quad (2.3)$$

where ρ is the water density, L is the ship length, and d is the ship draft. The prime (') means non-dimensional so that v'_m denotes the non-dimensional lateral velocity ($v'_m \equiv v_m/U$), and r' denotes non-dimensional yaw rate ($r' \equiv rL/U$). X'_H , Y'_H , and N'_H are expressed as follows:

$$\left. \begin{aligned} X'_H(v'_m, r', \phi) &= -R'_0 + X'_{vv}v_m'^2 + X'_{vr}v'_m r' + X'_{rr}r'^2 + X'_{vvvv}v_m'^4 \\ &\quad + X'_{v\phi}v'_m \phi + X'_{r\phi}r' \phi + X'_{\phi\phi}\phi^2 \\ Y'_H(v'_m, r', \phi) &= Y'_v v'_m + Y'_r r' + Y'_{vvv}v_m'^3 + Y'_{vvr}v_m'^2 r' + Y'_{vrr}v'_m r'^2 + Y'_{rrr}r'^3 \\ &\quad + Y'_\phi \phi + Y'_{vv\phi}v_m'^2 \phi + Y'_{rr\phi}r'^2 \phi + Y'_{v\phi\phi}v'_m \phi^2 + Y'_{r\phi\phi}r' \phi^2 \\ N'_H(v'_m, r') &= N'_v v'_m + N'_r r' + N'_{vvv}v_m'^3 + N'_{vvr}v_m'^2 r' + N'_{vrr}v'_m r'^2 + N'_{rrr}r'^3 \\ &\quad + N'_\phi \phi + N'_{vv\phi}v_m'^2 \phi + N'_{rr\phi}r'^2 \phi + N'_{v\phi\phi}v'_m \phi^2 + N'_{r\phi\phi}r' \phi^2 \end{aligned} \right\} \quad (2.4)$$

where X'_{vv} , Y'_v , N'_v , etc called the hydrodynamic derivatives on maneuvering. X'_H is expressed as an even polynomial function of v'_m , r' and ϕ . R'_0 denotes the hull resistance. Y'_H and N'_H are expressed as odd polynomial function of them.

2.3.2 Propeller force

Surge force due to the propeller (X_P) is expressed as follows:

$$X_P = (1 - t_p)T \quad (2.5)$$

where t_p is the thrust deduction factor. The propeller thrust T is written as:

$$T = \rho n_p^2 D_p^4 K_T (J_P) \quad (2.6)$$

where n_p is the number of propeller revolution and D_p is the propeller diameter. The propeller thrust open water characteristic K_T is expressed by the following equation.

$$K_T(J_P) = k_2 J_P^2 + k_1 J_P + k_0 \quad (2.7)$$

k_2 , k_1 , and k_0 are coefficients representing K_T , which is approximately expressed as the 2nd polynomial function of propeller advance ratio J_P .

$$J_P = \frac{u(1-w_P)}{n_P D_P} \quad (2.8)$$

where w_P in the equation is the effective wake fraction at the propeller position. It is assumed to change according to the maneuvering motion and expressed as a function of geometrical flow angle to the propeller β_P as follows:

$$w_P = (w_{P0} - w_{Pmin}) \exp(C_1 \beta_P^2) + w_{Pmin} \quad (2.9)$$

Here, $\beta_P \equiv \beta - l'_P r' + z'_P \dot{\Phi}'$. l_P and z_P are the longitudinal and vertical coordinates, respectively, of the propeller positions. w_{P0} is the effective wake fraction during the straight running. C_0 and w_{Pmin} are the coefficients representing the wake behaviour against β_P .

2.3.3 Rudder force

Hydrodynamic forces generated by the rudder (X_R, Y_R, N_R) are expressed as:

$$\left. \begin{aligned} X_R &= -(1 - t_R) F_N \sin \delta \cos \phi \\ Y_R &= -(1 + a_H) F_N \cos \delta \cos \phi \\ N_R &= -(x_R + a_H x_H) F_N \cos \delta \cos \phi \end{aligned} \right\} \quad (2.10)$$

where t_R , a_H , and x_H are parameters representing the interaction between the hull and the rudder. The rudder normal force F_N is expressed as follows.

$$F_N = 1/2 \rho A_R f_a (u_R^2 + v_R^2) \sin \left\{ \delta - \tan^{-1} \left(\frac{u_R}{v_R} \right) \right\} \quad (2.11)$$

In the equation, A_R denotes rudder area and f_a denotes rudder lift gradient coefficient. u_R is the propeller accelerated axial inflow velocity at the rudder and expressed as follows.

$$u_R = \varepsilon u (1 - w_P) \sqrt{\frac{D_P}{H_R} \left\{ 1 + \frac{k_x}{\varepsilon} \left(\sqrt{1 + \frac{8K_T}{\pi J_P^2} - 1} \right) \right\}^2 + \left(1 - \frac{D_P}{H_R} \right)} \quad (2.12)$$

where k_x is the flow acceleration rate and ε means ratio of wake fraction between the rudder and propeller position. u_R is the longitudinal inflow velocity and v_R is the lateral inflow velocity considering the flow straightening coefficient γ_R , which reduce the geometrical inflow angle during maneuvering, and it is expressed as follows.

$$v_R = U \gamma_R (\beta - l'_R r' + z'_R \dot{\phi}) \quad (2.13)$$

where l'_R is the effective longitudinal coordinate of the rudder position.

2.3.4 Wind force

Fujiwara et al. [31] proposed a method to estimate the longitudinal and lateral wind forces and yaw and roll moments for various ships based on the form-related parameters of the ship. It was developed through regression analysis using many winds tunnel experimental data from many wind tunnels. In their reference, the validation was conducted by comparing the estimated value with those of other methods and proved that the standard error against the experimental data was smaller than that of the others. It is considered a practical method of estimating the wind forces and moments. Its use is recommended by the ITTC [32] in case of unavailability of wind tunnel measurements. For example, the lateral wind force Y_W , is calculated by the following equation: The 1st term on the RHS expresses the lateral component of the crossflow drag, and the 2nd term expresses that of the lift and induced drag.

$$Y_A = \frac{1}{2} \rho_a U_{aw}^2 A_L \left\{ C_{CF} \sin^2 \psi_{aw} + C_{YLI} (\cos \psi_{aw} + \frac{1}{2} \sin^2 \psi_{aw} \cos \psi_{aw}) \sin \psi_{aw} \cos \psi_{aw} \right\} \quad (2.14)$$

where

$$C_{CF} = \alpha_0 + \alpha_1 \frac{A_F}{BH_{BR}} + \alpha_2 \frac{H_{BR}}{L_{OA}}, \quad C_{YLI} = \pi \frac{A_L}{L_{OA}^2} + \begin{cases} \gamma_{10} + \gamma_{11} \frac{A_F}{L_{OAB}} \\ \gamma_{20} + \gamma_{21} \frac{A_{OD}}{L_{OA}^2} \end{cases} \quad (2.15)$$

where ρ_a is the air density. Some ship's form-related parameters are used, that is, A_F : projected frontal area above waterline, A_L : projected lateral area above waterline, H_{BR} : height to top of superstructure, A_{OD} : lateral projected area of superstructure and containers on the deck, L_{OA} : ship length overall, α_i and γ_{ij} where i, j take 0, 1, or 2: regression parameters. The details of the method to estimate the wind forces and moments are explained in Appendix B.

Chapter 3

Subject Ship

The KCS container ship (FORCE and IIHR,2008) [33] was used to investigate the maneuvering performances.

3.1 Principal dimensions of the subject ship

For this study, the real-scale length between perpendiculars was 230 (m). This ship has a propeller with a diameter of 7.9 (m) and a semi-balanced horn rudder with height of 9.9 (m). A 1/75.24 scale-model was used. The side view of the hull model is present in Figure.3.1, and Figure 3.2 shows the body plan of the ship. Table 3.1 lists the principal dimensions of the container ship with the design draft in the real scale and model scale. Table 3.2 lists the propeller and rudder installed on the ship.



Figure 3.1: Side view of the 1/75.24 KCS model

Table 3.1: Principal dimensions of KCS

Item	Symbol	Real scale	Model scale
Length	L [m]	230	3.057
Breadth	B [m]	32.2	0.428
Design draft	d [m]	10.8	0.1435
Displacement	∇ [m ³]	52043	0.1222
Block coefficient	C_B	0.651	0.651

Table 3.2: Principal dimensions of propeller and rudder

Item	Symbol	Real scale	Model scale
Propeller diameter	D_P [m]	7.9	0.105
Propeller pitch ratio	P/D_P	0.997	0.997
Rudder height	H_R [m]	9.9	0.1316
Rudder cord length	B_R [m ³]	5.5	0.0731
Rudder aspect ratio	Λ	1.8	1.8
Rudder area w/ horn	A_R [m ²]	54.43	0.0096

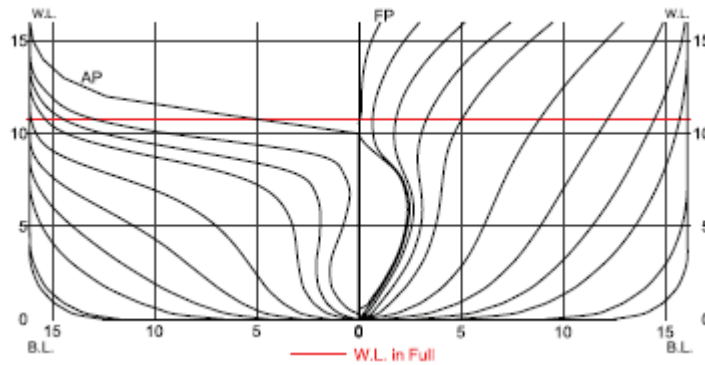


Figure 3.2: Body plan of KCS ship

3.2 Loading conditions of the subject ship

Five loading conditions were set to present the draft conditions and trim. EK is considered the design draft and even keel, which is also used as the basis for comparison for every loading condition. The draft combinations described the loading conditions based on the amount of displacement with an even keel condition. S-EK represented a shallow draft where the displacement decreased by $\pm 14\%$ with an even keel. D-EK represented a deep draft where the displacement $\pm 15\%$ increased with an even keel. The trim combinations have the same draft as EK. TS represented trim by the stern, and TB represented trim by the bow. The radius of the yaw gyration was set to $0.25L_{PP}$ in all loading conditions. Table 3.3 shows those loading conditions for the model scale including the ship drafts, aft, mean, and fore drafts (i.e., d_a , d_m and d_f), along with the related parameters: the displacement ∇ , block coefficient C_B , the longitudinal position of the center of gravity x_G which is defined as the distance from the midship, the metacenter height \overline{GM} and the immersion depths from the water surface to the top

of the propeller and rudder (i.e., $d_{propeller}$, d_{rudder}). Table 3.4 shows the draft and displacement in each loading condition for the real scale. Other parameters are explained in the next section.

Table 3.3: Loading conditions for the model-scale KCS used in the experiment

Symbol	S-EK	TS	EK	TB	D-EK
d_a [m]	0.1276	0.1594	0.1435	0.1276	0.1594
d_m [m]	0.1276	0.1435	0.1435	0.1435	0.1594
d_f [m]	0.1276	0.1276	0.1453	0.1594	0.1594
∇ [m ³]	0.1054	0.1222	0.1222	0.1222	0.1400
C_B	0.631	0.651	0.651	0.651	0.671
x_G [m]	-0.028	-0.100	-0.045	0.005	-0.064
\bar{GM} [m]	0.01	0.008	0.008	0.008	0.007
$d_{propeller}$ [m]	0.020	0.052	0.036	0.021	0.052
d_{rudder} [m]	-0.005	0.026	0.011	-0.005	0.026

Table 3.4: Loading conditions for the real-scale KCS

Symbol	S-EK	TS	EK	TB	D-EK
d_a [m]	9.6	9.6	10.8	11.99	11.99
d_m [m]	9.6	10.8	10.8	10.8	11.99
d_f [m]	9.6	11.99	10.8	9.6	11.99
∇ [m ³]	44890	52046	52046	52046	59327
C_B	0.631	0.651	0.651	0.651	0.671

3.3 Design of the over deck objects in the real scale

The maneuvering simulation of the real-scale ship considering wind disturbance is presented in the following chapter. Because the ship model used in the experiment had no objects on the deck, it was necessary to design the superstructure and arrange the containers according to each loading condition.

KCS is a 3600 TEU (Twenty Foot Equivalent Unit) which was designed to load 1800 FEU (Forty-foot equivalent unit dry containers (12.192(m) \times 2.438(m) \times 2.591(m))). The minimum weight per container was assumed as 3.74 (t) for an empty container (self-weight of a container),

and the maximum weight was assumed as 30.48 (t) for a full-load container. The total weight of the containers was considered as the weight after excluding the lightweight, which was assumed to be 16323 (t), from the displacement. The container arrangement and container weight distribution were designed considering the available space in the hold and on deck, the prescribed draft, trim, longitudinal position of the centre of gravity, and its height position to achieve a positive GM. The maximum height of the stacked containers is adjusted to ensure downward visibility from the bridge.

Figure 3.3 illustrates 3D images of the KCS loading containers, that is, S-EK, EK, and EK without the hull image under the deck. Figure 3.4 shows the weight of the containers on each tier at each bay below the deck (inside the hold) and over the deck in the case of EK; the x -axis indicates the number of container bays in the longitudinal position from the stern and the legend indicates the number of tiers from the deck. For example, the data $x=6$ and “3rd” in the upper figure represent the total weight of the containers positioned on the 3rd tier above the deck at the 6th bay. In the hold, the containers were reduced in the area close to the bow and stern because of the narrow hull width. This results in a reduced container weight in that area. Because of the GM, the number of containers on the higher tier over the deck is also small. For TB and TS, which have the same displacement as EK, their weight distribution was designed to achieve the prescribed trim and the proper position of the center of gravity, assuming the same number of containers, i.e., 1800 FEU, were loaded, and their arrangement was maintained in the same manner as EK. An overloading condition, D-EK, was achieved by arranging overweight containers, of which the per unit weight was assumed to be 1.2 times heavier than a full-load container inside the hold. Meanwhile, S-EK reduced the number of containers to 1025 FEU because of the small displacement, and the arrangement of the containers and their weight distribution were adjusted. Figure 3.5 shows a comparison of the weight distributions of the containers in the longitudinal direction among the five loading conditions designed in this study.

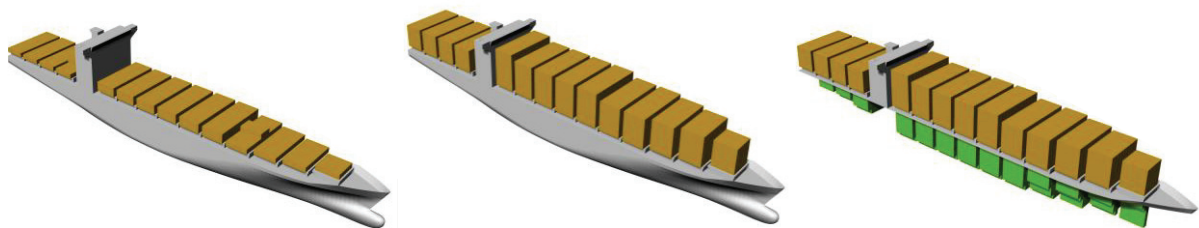


Figure 3.3: Image of KCS with loading containers: S-EK (left), EK (middle), EK with visualization of the containers inside (right)

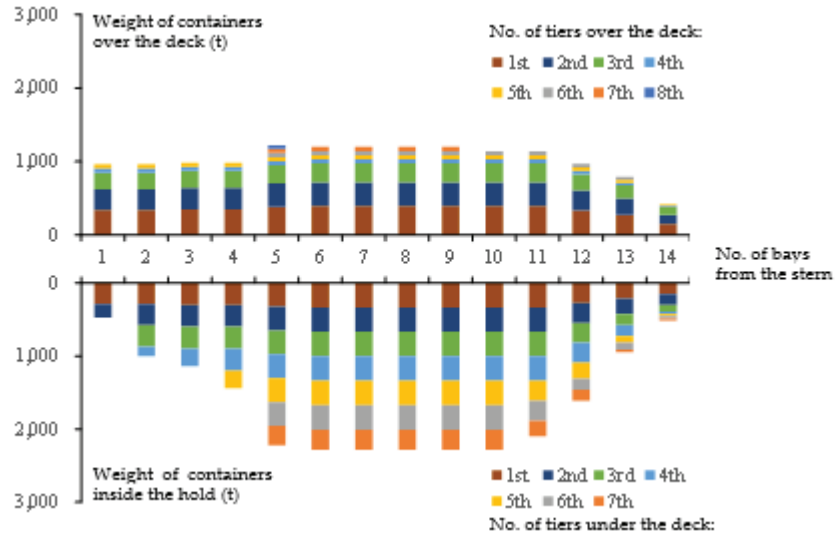


Figure 3.4: Weight of containers on each tier at each bay for EK

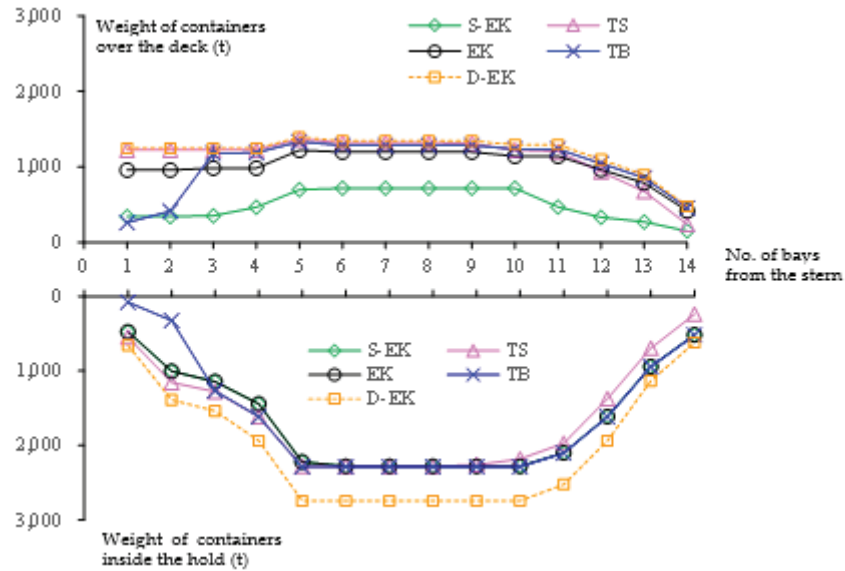


Figure 3.5: Comparison of the weight distribution of containers in the longitudinal direction among the five loading conditions

The radius of gyration, that is, the moment of inertia of the ship around the x and z axes, was calculated based on the weight distribution of containers in each condition, assuming that those of the naked hull were $0.25L_{PP}$ and $0.25B$, respectively. They are listed in Table 3.5, along with the position of the C.G of the ship and the metacenter height GM . The vertical position of the C.G of the naked hull was assumed to be half that of the draft. Note the nondimensional values x_G and \overline{GM} are different from those in Table 3.3 which were used in the experiment and not determined by considering the weight distribution of imaginarily designed containers, then.

Table 3.5: Position of the center of the gravity, \overline{GM} and radius of gyration in the roll and yaw moments

Symbol	S-EK	TS	EK	TB	D-EK
x_G [m]	-2.17	-7.77	-3.41	0.50	-4.86
KG [m]	11.86	14.67	14.32	14.26	14.70
\overline{GM} [m]	3.03	0.60	0.63	0.40	0.36
k_{xx}/B	0.329	0.382	0.378	0.378	0.374
k_{xx}/L	0.238	0.246	0.246	0.234	0.247

3.4 Estimation of wind forces and moments in the real scale

Table 3.6 lists the main parameters related to the windage area under each loading condition. (C_{MC} , H_C) is the geometric centre position of the windage area from the midship above the water surface. These are important for yaw and roll moment levers. Because of the same arrangements of containers on the deck among EK, D-EK, TB, and TS (notably, the weight distribution of containers among them is different), there was no significant difference in the lateral windage area, A_L . On the other hand, S-EK has a smaller lateral windage area because of the small number of containers on the deck. The frontal windage area, A_F , is nearly the same each other because of the common superstructure, which is the tallest structure on board.

Table 3.6: Representative parameters related to the windage area for each loading condition.

Symbol	S-EK	TS	EK	TB	D-EK
A_F [m]	1234	1128	1198	1212	1159
A_L [m]	3934	5665	5676	5670	5391
C_{MC} [m]	-5.40	-2.83	-4.64	-6.37	-4.78
H_C	9.29	13.27	13.31	13.36	12.76

The wind force in the longitudinal and lateral directions, X_{aw} , Y_{aw} , and wind moment in yaw and roll, N_{aw} , K_{aw} , were estimated by Fujiwara et al. [31]. They were divided by U_{aw}^2 to eliminate the effect of the wind speed and remain the difference due to the difference in the windage area. Figure 3.6 shows these against the apparent wind angle ψ_{aw} . The wind surge force and yaw moment vary to take their peaks when the apparent wind blows diagonally in forward or backward directions, whereas the wind lateral force and roll moment appear larger

when the wind blows from the side around $\psi_{aw}=90^\circ$. The magnitudes of the wind force and moment were proportional to the frontal and lateral windage areas.

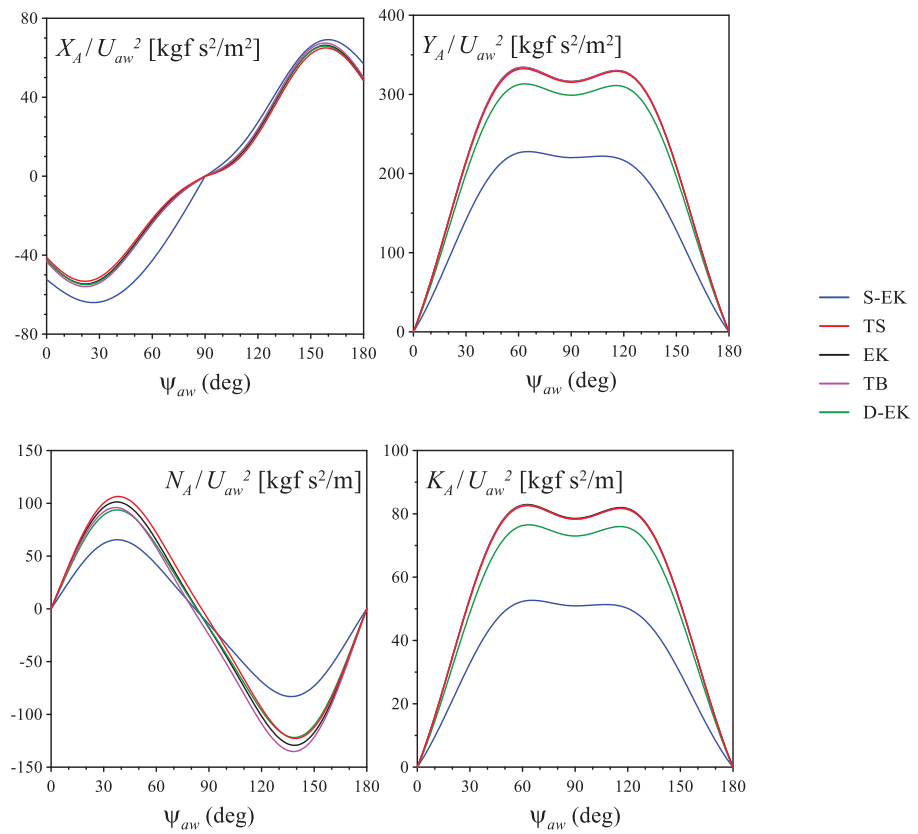


Figure 3.6: Estimated wind force and moment of the subject ship with respect to the apparent wind angle

Chapter 4

Experimental Study: Free-running Model Test

In this chapter, the Free-running model tests are explained, which were conducted in the marine dynamic basin at the Japan Fisheries Research and Education Agency, Japan.

4.1 Outline of free-running model test

Free-running model tests in calm water were conducted in the Marine Dynamics Basin (length: 60 (m), breadth: 25 (m), depth: 3.2 (m)) at the Fisheries Technology Institute of Japan Fisheries Research and Education Agency, Japan. Figure 4.1 shows a photo of the basin.

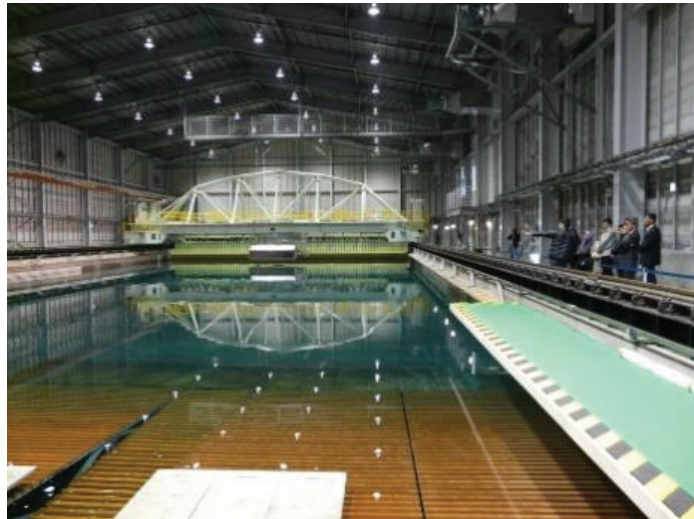


Figure 4.1: Photo of the marine dynamic basin for the free-running model test.

(Source: http://nrife.fra.affrc.go.jp/topics/20101112/topics_20101112.html)

The $\pm 35^\circ$ turning ($\pm 35T$), $10^\circ/10^\circ$ zig-zag (10Z), and $-10^\circ/-10^\circ$ zig-zag ($-10Z$) tests were conducted under every loading condition. The model ship's initial speed was set to 0.86 (m/s) and the steering speed was set to $20.12^\circ \text{ s}^{-1}$. The propeller rotation speed n_p was adjusted to model the self-propulsion point (MSPP) under each loading condition. Table 4.1 lists the value. For example, S-EK had the lowest propeller rotation speed, while TS had the highest. These values reflected resistance and self-propulsive performance. The ship position was measured by tracking prism reflectors on the model ship. This is the same measurement system used by

Matsuda et al. [34] and Hasnan et al. [35]. The ship speed and hull drift angle were calculated based on these data. The angular data was measured with a three-axis fiber optics gyroscope. The measured values were transmitted to an on-land computer by a wireless local area network at 10 Hz and saved.

Table 4.1: Model self-propulsion points under the different loading conditions

Symbol	S-EK	TS	EK	TB	DE
n_p [rps]	10.4	10.8	10.5	10.5	10.7

4.2 Turning test results

4.2.1 Turning trajectory and its indices

Figure 4.2 shows the trajectory of the midship position in the $\pm 35T$ tests. The steering started at $(x_0, y_0) = (0, 0)$ where the ship was heading straight ahead. The S-EK, EK, and D-EK results are on the left side to compare the draft series, and the TS, EK, and TB results are on the right side to compare the trim series. Table 4.2 summarizes the advance A_D , which was defined as the distance advanced until the heading reached 90° from the original initial course and the tactical diameter D_T , which was defined as the lateral distance travelled until the heading reached 180° , for each loading condition. Their parameters are compared between $\pm 35T$ in Figure 4.3.

Table 4.2: Advances and tactical diameters during the $\pm 35T$ test

Symbol	Type	S-EK	TS	EK	TB	D-EK
A_D/L_{PP}	35T	3.10	2.99	3.04	3.08	3.14
	-35T	3.11	2.96	3.03	2.99	2.90
	Average	3.11	3.98	3.04	3.04	2.97
D_T/L_{PP}	35T	3.33	3.17	3.16	3.02	2.95
	-35T	3.18	3.05	2.95	2.81	2.73
	Average	3.26	3.11	3.06	2.92	2.84

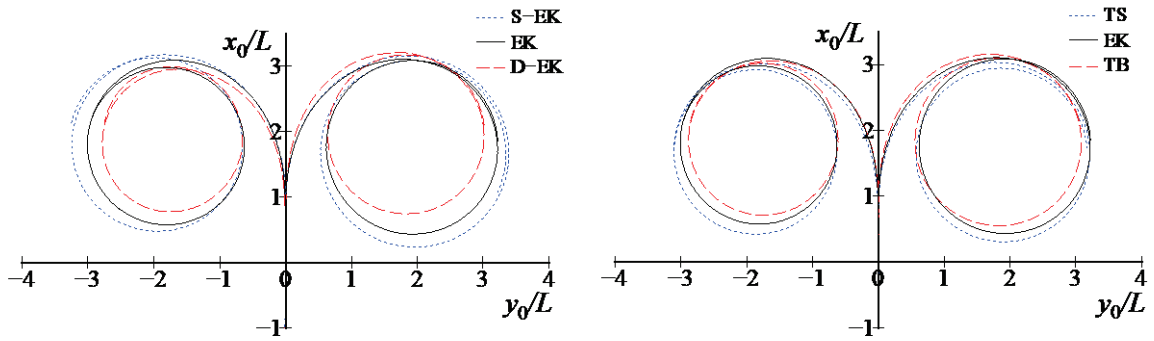


Figure 4.2: Trajectories during the $\pm 35^\circ$ test on the draft (left) and trim series (right)

The advance shows almost the same order of magnitude between them, or the advance in port turning (-35° T) is smaller than in the starboard turning ($+35^\circ$ T). Because the port turning also distinctly shows a smaller tactical diameter, a fast response, and good turning performance are achieved when steering to the port direction regardless of loading conditions. Such an asymmetric turning motion is a common tendency for a ship with a right-handed propeller, e.g., Yasukawa and Sano [36]. This is related to an asymmetry in the straightening phenomena owing to the presence of the hull and rotated propeller, causing an asymmetrical inflow angle at the rudder. As it is seeming to be influenced by the hull draft and trim, the magnitude of the difference in turning performance between the port and starboard turning varies depending on the loading condition. Figure 4.3 indicates the larger asymmetrical turning motion is observed in the deeper bow draft cases, i.e., D-EK and TB, or even draft case, i.e., EK, while the difference becomes smaller in the cases of the shallower draft at the bow, i.e., S-EK and TS.

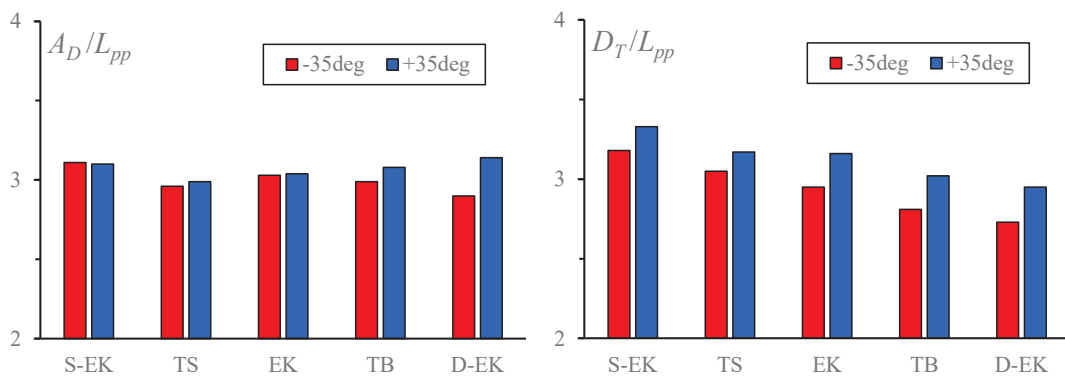


Figure 4.3: Comparison of the advance (left) and tactical diameter (right) between $\pm 35^\circ$ T for each loading condition

The turning parameters are plotted in Figure 4.4 concerning the change in the midship draft (Δd) from EK and trim ($\Delta\tau$), which are defined as follows:

$$\left. \begin{aligned} \Delta d &= 100(d_m - d_{EK})/L_{PP} \\ \Delta\tau &= 100(d_a - d_f)/2L_{PP} \end{aligned} \right\} \quad (4.1)$$

where d_{EK} is the mean draft of EK. Δd changes from -0.52(S-EK) to 0.52(D-EK). It can be considered a small range of change compared with Inoue et al. [14], which Δd was -1.77 between full-load and ballast-load (zero-trim) conditions for a container ship. $\Delta\tau$ changes in the same range from -0.52 (TB) to 0.52(TS). The average values of $\pm 35T$ tests were also calculated and plotted as a line graph in Figure 4.4 below. In order to grasp the overall trend of the draft and trim effect on the turning parameters, the following discussion is based on the average values.

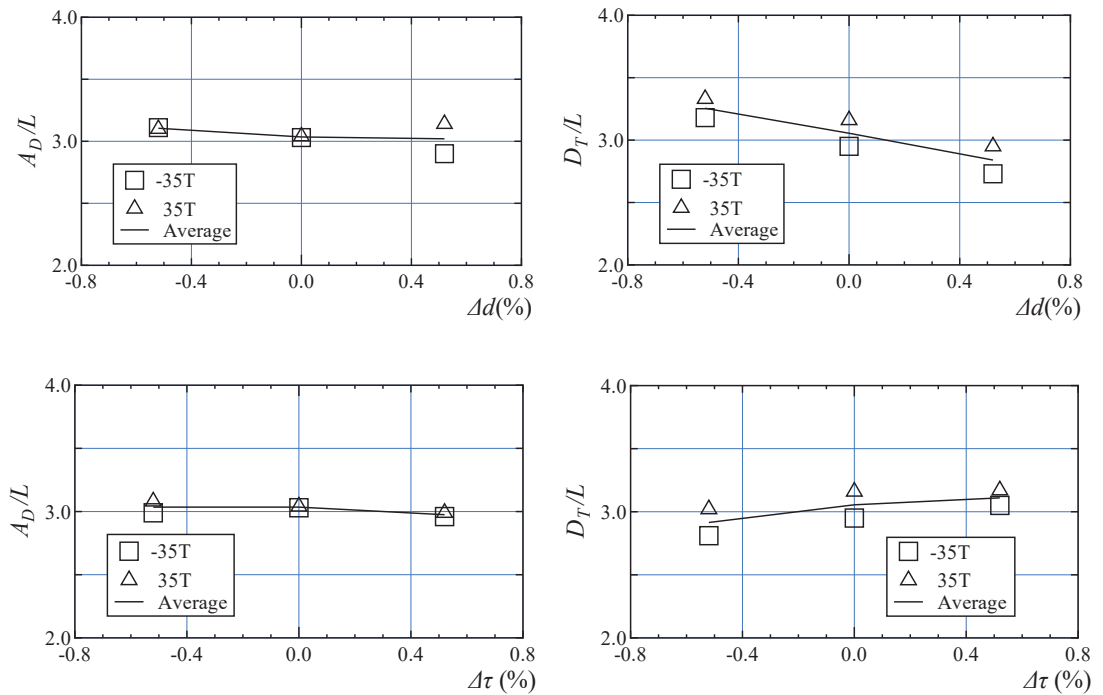


Figure 4.4: Advances and tactical diameters during the $\pm 35T$: draft series (top) and trim series (bottom)

Among the draft series, the turning radius increased in the order of D-EK, EK, and S-EK. Compared with EK, D_T was 3% smaller for D-EK and 6% larger for S-EK. This indicates that a slight shallow draft, which may be caused by a lack of loading containers or a winter voyage, would reduce the turning ability of a container ship. Among the trim series, TS had a larger turning trajectory, while TB had a smaller one. This indicates that trim by the stern would worsen the turning performance. In terms of the advance, there does not seem to be significant differences among the loading conditions. Overall, the turning ability deteriorated with decreasing draft or with increasing trim by the stern, although the changes were not drastic.

4.2.2 Time series of motions

Figure 4.5 shows a comparison of the time series of the non-dimensional yaw rate ($r' = rL_{PP}/U_0$), hull drift angle (applied by 3-point moving average) and roll angle during the 35° turning test among draft series (top) and trim series conditions (bottom), respectively. Because a similar trend was observed in the time series of the left and right turning motions, only the results of the 35° turning test are focused on here.

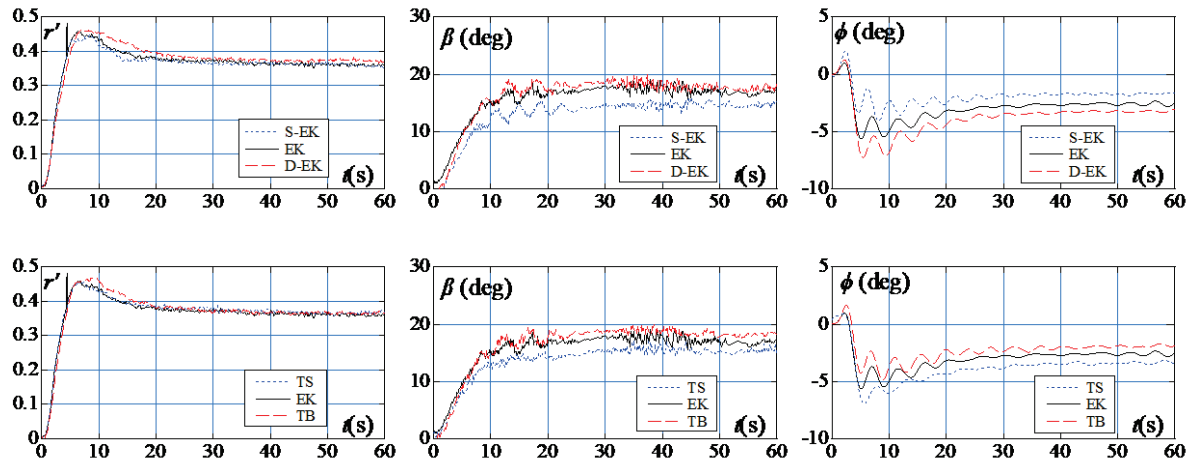


Figure 4.5: Time series of the non-dimensional yaw rate, hull drift angle and roll angle in +35T: draft series (top) and trim series (bottom)

In steady turning, the hull drift angle increases with an increase in the draft, in the order of S-EK, EK, and D-EK. It also increases with an increase in the trim by bow, that is, in the order of TS, EK, and TB. Because a large hull drift angle reduces the forward surge speed, it would

result in a small, steady-state turning. Indeed, the tactical diameter shown in Figure 4.4 or listed in Table 4.2 decreases in the same order.

Regarding the yaw rate, a difference around the transient state of turning is noticeable. Especially in the case of D-EK, the development of the yaw rate seems more than other draft conditions owing to the large inertial force, which indicates the longer advance. In the trim series, a large peak is observed in the case of trim by bow, TB. The shallow draft at the stern may help the stern swing by the rudder force. Thus, it might have resulted in increasing the transient yaw rate. Meanwhile, there is no noticeable difference in the steady yaw rate from the other trim conditions. Because the hull drift angle increases the most in TB, this causes a decrease in the ship speed and might have resulted in a similar steady yaw rate as others.

The outward roll motion occurs due to the roll moment of a couple of centrifugal forces and hydrodynamic forces while turning. Therefore, in the draft series, the roll angle increases in the order of the draft or displacement. Meanwhile, in the trim series, the roll angle increases with an increase in the trim by stern. Because of the smallest hull drift angle in TS, causing the faster ship speed than others, the larger centrifugal force might have acted on the ship under this condition. Yasukawa et al. [37] pointed out the influence of a heel on the turning performance. Therefore, the difference in the roll angle may be one of the reasons for the difference in the turning diameter.

4.3 Zig-zag test results

4.3.1 Time series of motions

Figure 4.6 shows the time series of the heading and rudder angles measured during the $\pm 10Z$ tests. The change in the non-dimensional yaw rate, hull drift angle, and roll angle are also shown in Figure 4.7, in which the time series of $10Z$ are examined.

Both the draft and trim apparently have significant effects on the zig-zag maneuvers. The time series of the yaw rate and hull drift angle shows a quick steering response in S-EK, while a slow response is observed in D-EK. They caused a difference in the achieved heading angle. This can be explained by the difference in the displacement or inertial force. In the trim series, the ship in TS moves quickly and achieves the smallest heading angle, while the ship in TB achieves the largest one. As one reason, it would be related to the magnitude of the rudder force, as discussed in section 4.2 in terms of the roll angle, the difference is not necessarily noticeable.

Nevertheless, the magnitude of the roll angle seems to increase in D-EK and TS. This is consistent with the turning test results.

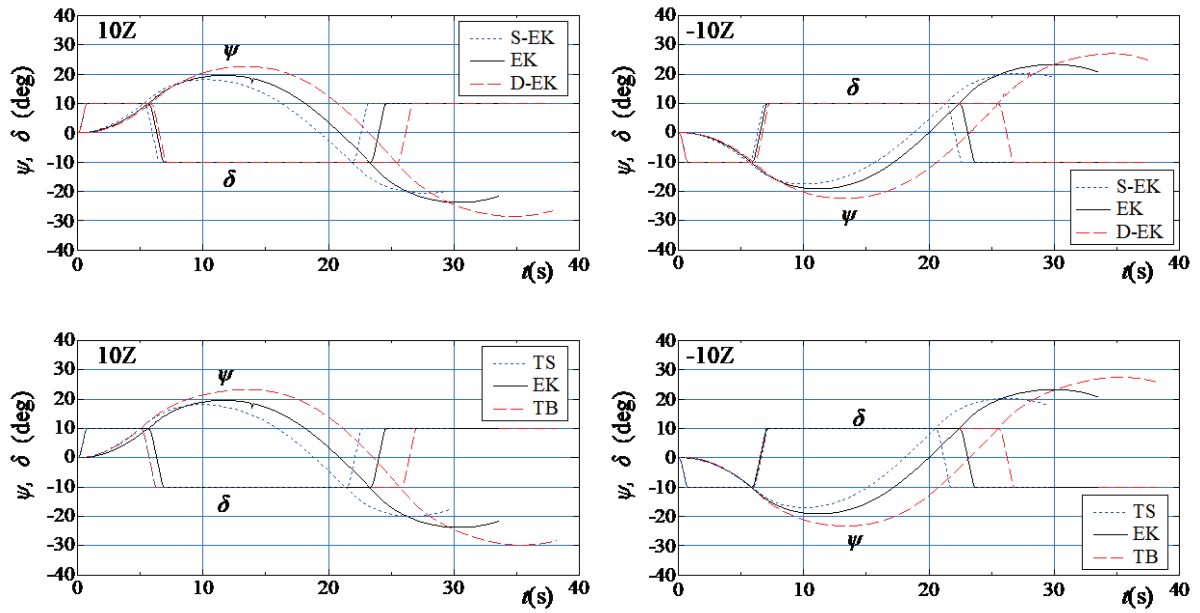


Figure 4.6: Time series of the heading and rudder angles during $\pm 10Z$: draft series (top) and trim series (bottom)

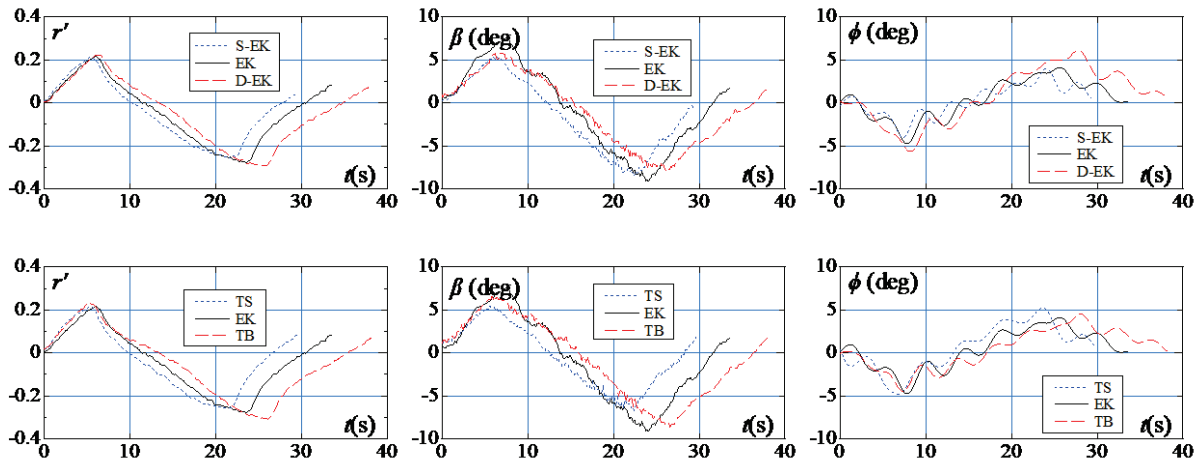


Figure 4.7: Time series of the non-dimensional yaw rate, hull drift angle and roll angle in $+10Z$: draft series (top) and trim series (bottom)

4.3.2 Overshoot angles

The first and second overshoot angles (OSAs) were calculated, and the average OSA $\pm 10Z$ tests were also calculated, as listed in the Table 4.3. They are plotted in Figure 4.8 with respect to Δd for the draft series condition and to $\Delta \tau$ for the trim series conditions.

Table 4.3: Overshoot angle for the $\pm 10Z$ tests

Item	Type	S-EK	TS	EK	TB	D-EK
First OSA ($^{\circ}$)	10Z	8.15	8.19	9.58	13.34	12.62
	-10Z	7.39	6.98	9.12	13.24	12.31
	Average	7.77	7.59	9.35	13.29	12.47
Second OSA ($^{\circ}$)	10Z	10.55	9.91	13.72	19.76	18.48
	-10Z	10.40	10.33	13.33	17.49	17.03
	Average	10.47	10.12	13.53	18.63	17.75

For the draft series, the average first OSA was 17% smaller for S-EK and 33% larger for D-EK than EK. The average second OSA also showed a similar tendency: it was 23% smaller for S-EK and 31% larger for D-EK than EK. This indicates that the yaw-checking ability or course stability deteriorates in the order of S-EK, EK, and D-EK, even though the draft does not change drastically. Assuming a situation such that a container ship is not fully loaded or voyages in winter, the shallow draft then would improve the controllability instead of the worse turning ability as discussed in section 4.2.

For the trim series, the first and second OSAs were 42% and 37% larger, respectively, for TB compared with EK. In contrast, the first and second OSAs were 19% and 25% smaller, respectively, for TS compared with EK. Although trim by the bow is generally preferable for the propulsive power performance e.g., Reichel et al. [11], the increased OSA indicates significant deterioration of the yaw-checking and course stability performances, which is a concern for navigation safety.

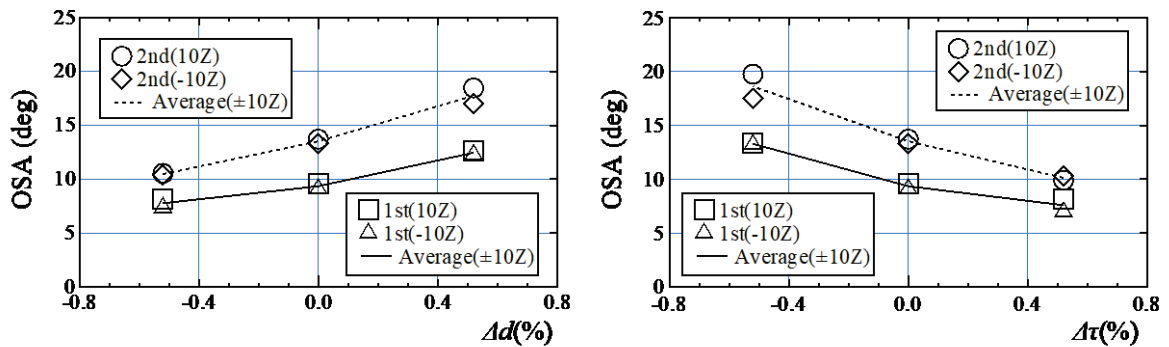


Figure 4.8: 1st dan 2nd overshoot angles for the $\pm 10Z$ tests: draft series (left) and trim series (right)

Chapter 5

Experimental Study: Captive Model Test

The captive model tests were mainly conducted in the Hiroshima University towing tank (length: 100 (m), breadth: 8 (m), depth: 3.5 (m)) and the marine dynamic basin at the Japan Fisheries Research and Education Agency (length: 60 (m), width: 25 (m), depth: 3.2 (m)).

5.1 Outline of captive model tests

A load cell was installed at the midship and was used to measure the surge force (X), sway force (Y), and yaw moment around the midship (N). The setup ship speed U_0 was 0.89 (m/s) (15kn for the full scale), and the propeller was operated at the MSPP. Based on the measured thrust at the self-propelled condition, the thrust deduction factor (i.e., t_p) which is the coefficient of the resistance increase caused by the changes in the pressure distribution due to the propeller operation, was identified and listed in Table 5.1. there does not seem to have a significant influence on the thrust deduction phenomena under these loading conditions on the whole.

Table 5.1: Thrust deduction factor

Symbol	S-EK	TS	EK	TB	DE
t_p	0.119	0.114	0.133	0.167	0.100

In the following section, the results of three kinds of tests are discussed here. In the rudder force test, the ship was moved straight ahead with the rudder at an angle. Rudder angles of -35° to 35° were considered at 5° intervals. In the oblique towing test (OTT), the ship was moved obliquely. The hull drift angle was varied at 5° intervals in the range of -20° to 20° , which corresponded with the non-dimensional sway velocity $v' (= v_m/U_0)$ from -0.35 to 0.35. In the circular motion test (CMT), the ship was moved with steady yawing. The non-dimensional yaw rate defined as $r' = rL_{PP}/U_0$ was set to $\pm 0.1, \pm 0.2$. The rudder was always kept amidship in OTT and CMT. Maneuvering forces such as the sway force Y and yaw moment N were focused on below. Although L_{PP}^2 or $L_{PP}d_m$ is commonly used as the reference area for the non-dimensional coefficient e.g., Bertram [38], $L_{PP}d_{EK}$ where d_{EK} is the mean draft of EK was

adopted in this study to help readers directly compare the magnitudes of the force and yaw moment among different loading conditions. Y and N were non-dimensionalized as follows.

$$\left. \begin{aligned} Y' &= Y / (0.5\rho L_{PP} d_{EK} U_0^2) \\ N' &= N / (0.5\rho L_{PP}^2 d_{EK} U_0^2) \end{aligned} \right\} \quad (5.1)$$

where ρ is the density of water. The prime symbol indicates that the parameter is non-dimensional.

5.2 Rudder force test results

5.2.1 Maneuvering force by steering

Figure 5.1 compares the non-dimensional sway forces and yaw moments acting on the ship during the rudder force test. The results for the draft series and trim series are plotted from a rudder angle. Because of the lift characteristics of the rudder, the sway force of the ship increased linearly at small rudder angles, and the rate of increase decreased at larger rudder angles because of the stall phenomenon. Because the acting point of the sway force by steering should be around the stern, a positive (clockwise) yaw moment was induced by a negative (port direction) sway force. To compare the magnitudes of the rudder force among different loading conditions, the rudder force coefficients Y'_δ and N'_δ were determined with a focus on the linear ranges of Y' and N' with respect to the rudder angles.

$$\left. \begin{aligned} Y' &= Y'_\delta \delta \\ N' &= N'_\delta \delta \end{aligned} \right\} \quad (5.2)$$

The rudder force coefficients are listed in Table 5.2 and plotted with respect to Δd and $\Delta \tau$ in Figure 5.2. The absolute values of Y'_δ and N'_δ generally increased with Δd or $\Delta \tau$. They are primarily determined by the inflow velocity to the rudder. Since D-EK ($\Delta d = 0.52$) had the high number of propeller rotations and the strong wake was assumed due to the underwater blunt hull shape, more accelerated flow was expected at the rudder position. It seems one of the reasons why these values increased and resulted in the smallest turning diameter in D-EK

(Figure 4.2) among draft series. Regarding the trim series, TS ($\Delta\tau = 0.52$) had the highest number of revolutions and the largest rudder force coefficients. The absolute values decreased in the order of EK ($\Delta\tau = 0$) and TB ($\Delta\tau = -0.52$). This was not consistent with the order of the turning diameter (Figure 4.4), where TS resulted in the largest turning circle regardless of the large rudder force coefficient. This may indicate that differences in the rudder forces are not sufficient for explaining the differences in maneuvering observed in the free-running tests.

Table 5.2: Rudder force coefficients

Symbol	S-EK	TS	EK	TB	D-EK
Y'_δ	-0.0513	-0.0595	-0.0584	-0.0496	-0.0578
N'_δ	0.0281	0.0325	0.0301	0.0290	0.0354

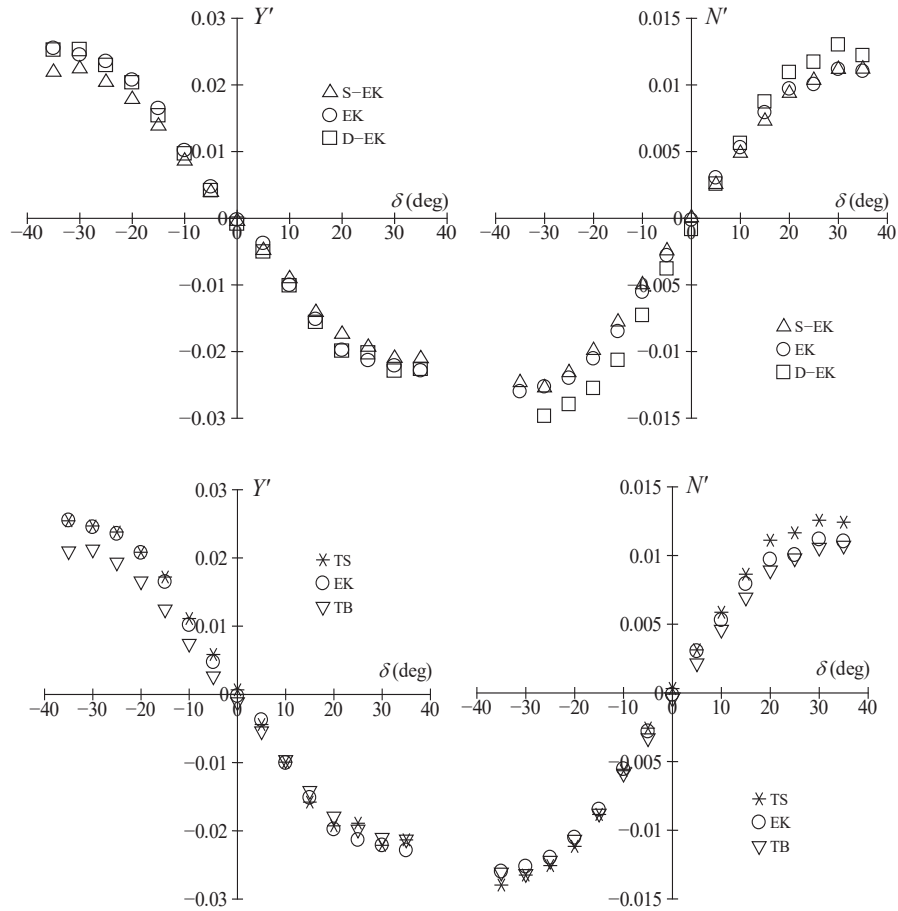


Figure 5.1: Non-dimensional sway force and yaw moment in the rudder force test depending on the draft series (top) and the trim series (bottom)

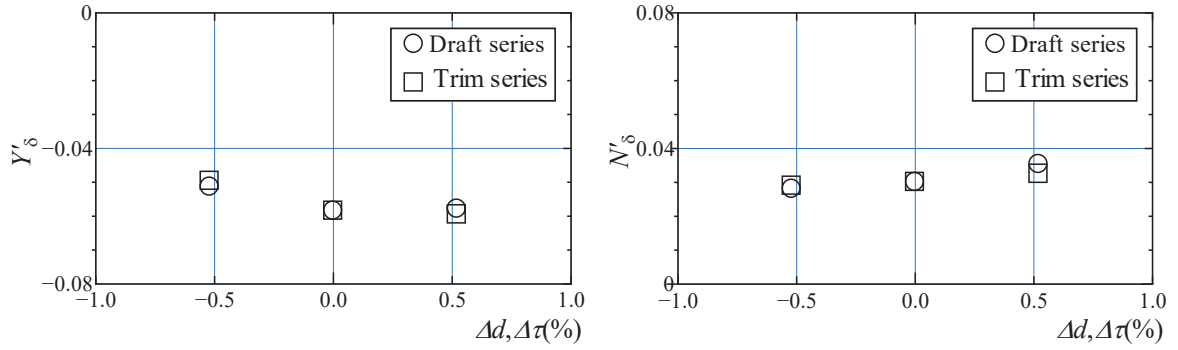


Figure 5.2: Y'_δ (left) and N'_δ (right) among draft-series and trim-series conditions.

5.2.2 Parameters for rudder normal force

Based on the rudder force test in straight motion, ε and κ appearing in Eq. 2.12 were obtained. Table 5.3 shows ε , κ and k_x (the product of ε and κ) in each loading condition. Figure 5.3 shows a comparison of them. When ε decreases with increasing draft and aft trim, κ tend to increase, and their product k_x is almost the same. The k_x value is approximately 0.6, which is consistent with the value for other ships [39]. In the tank tests, the rudder model was always submerged, and the upper part of the rudder model was always submerged, and the upper part of the rudder did not come out to the surface when moving straight, even if the draft or trim changed. For this reason, it is considered that the rudder force parameters such as ε , κ and k_x did not change significantly depending on the loading condition.

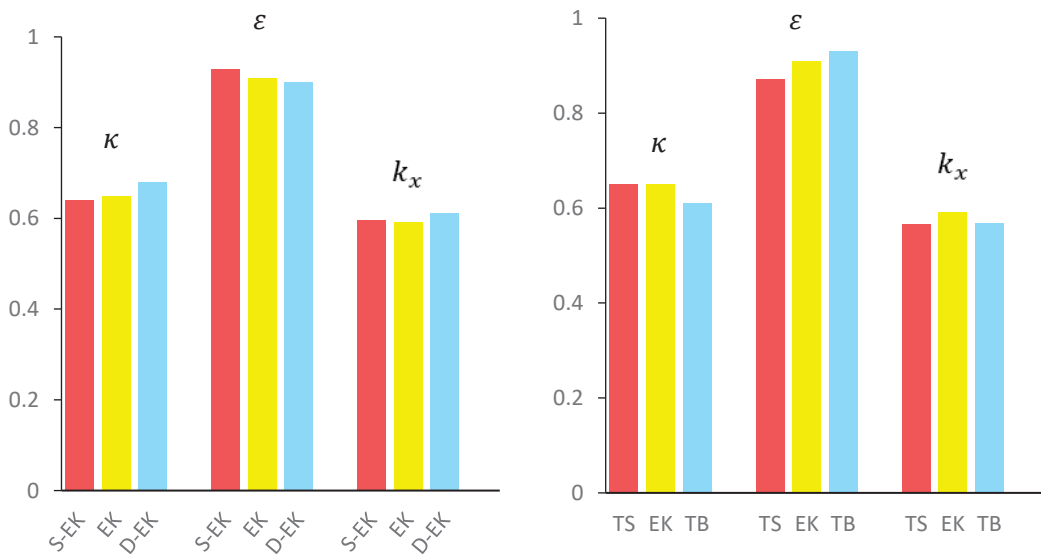


Figure 5.3: Comparison of ε , κ and k_x in draft series (left) and trim series (right)

Table 5.3: ε , κ and k_x in five different loading conditions

Symbol	S-EK	TS	EK	TB	D-EK
ε	0.93	0.87	0.91	0.93	0.90
κ	0.64	0.65	0.65	0.61	0.68
k_x	0.60	0.57	0.59	0.57	0.61

As an example, in Figure 5.4 shows a comparison of the rudder normal force coefficient (F'_N) versus rudder angle, δ , between predicted value (CAL) using the obtained ε and κ , and the test results. In the captive test, F'_N is not 0, even $\delta = 0$, and the check helm with a few degrees is confirmed. Since the check helm is set to 0 in the simulation model, a slight difference is observed in comparison with the experiment. However, the predicted value of the F'_N approximately agrees with the test results.

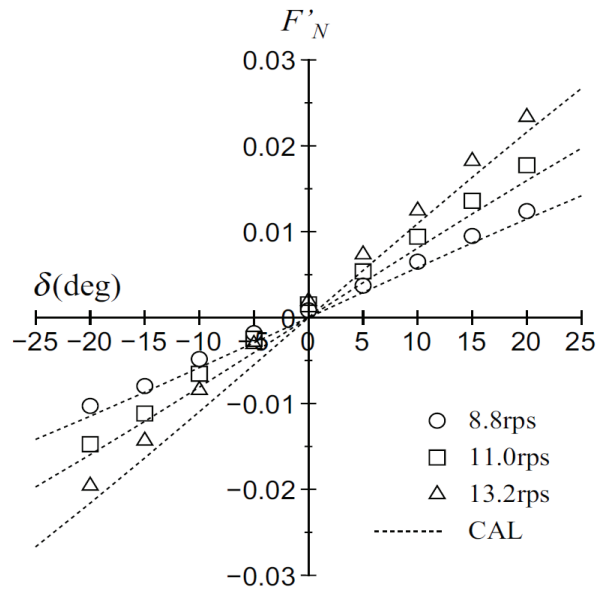


Figure 5.4: Analysis result of rudder normal force coefficient (F'_N) for EK

5.2.3 Hull and rudder interaction coefficients

The hull and rudder interaction coefficient (t_R , a_H , and x'_H) appearing in Eq. 2.10 which were analyzed based on the test results of the rudder force test in straight motion. The analysis results are presented in Table 5.4. Figure 5.5 shows a comparison of them. As an example, Figure 5.6 shows the surge force coefficient (X') acting on the ship versus $-F'_N \sin \delta$ and the lateral force

coefficient (Y') and the yaw moment coefficient (N') versus $-F'_N \cos \delta$. $(1 - t_R)$ is the slope of X' with respect to $-F'_N \sin \delta$, and $(1 + a_H)$ is the slope Y' with respect $-F'_N \cos \delta$. x'_H is obtained from the slope of N' with respect to $-F'_N \cos \delta$. Although the test results for X' fluctuate slightly from the fitting line, the test results for Y' and N' are on the fitting lines. The hull and rudder interaction coefficients do not seem to have a clear correlation with the loading conditions as shown in Figure 5.5.

Table 5.4: Hull-rudder interaction coefficients in five different loading conditions

Symbol	S-EK	TS	EK	TB	D-EK
t_R	0.244	0.209	0.369	0.246	0.212
a_H	0.206	0.317	0.334	0.205	0.302
x'_H	-0.715	-0.658	-0.525	-0.715	-0.848

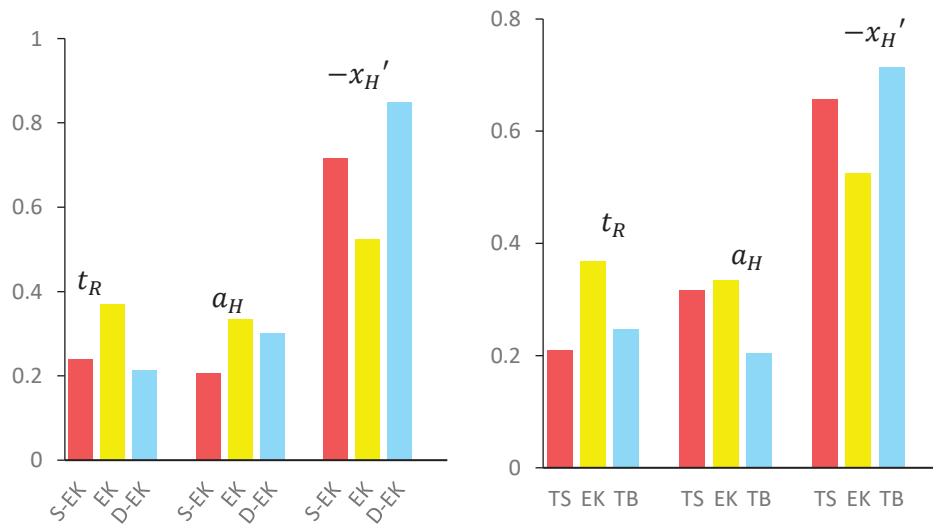


Figure 5.5: Comparison of t_R , a_H and x'_H in draft series (left) and trim series (right)

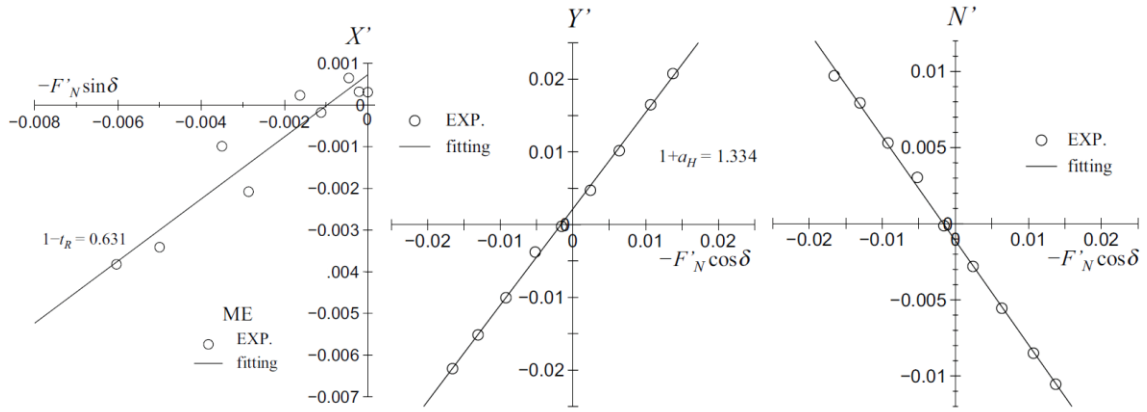


Figure 5.6: Analysis of hull-rudder interaction coefficients for EK

5.3 Flow straightening results

In this subsection, Table 5.5 shows the obtained flow straightening coefficient γ_R in each loading condition. Figure 5.7 shows the comparison of them. As the model of γ_R , a model with different values depending on the positive or negative drift angle β is adopted. γ_R when β is negative is approximately half the value when β is positive. This is because the target ship is a single-shaft ship, and the inflow direction to the rudder differs between the starboard and port side owing to the propeller rotational flow effect. However, when $\beta \geq 0$, there is no clear tendency regarding the magnitude of γ_R with the draft or trim change, it tends to increase with the draft of trim change when $\beta < 0$.

Table 5.5: Flow straightening coefficient (γ_R) in five different loading conditions

Symbol	S-EK	TS	EK	TB	D-EK
γ_R (for $\beta \geq 0$)	0.494	0.538	0.459	0.468	0.542
γ_R (for $\beta < 0$)	0.213	0.275	0.245	0.194	0.274

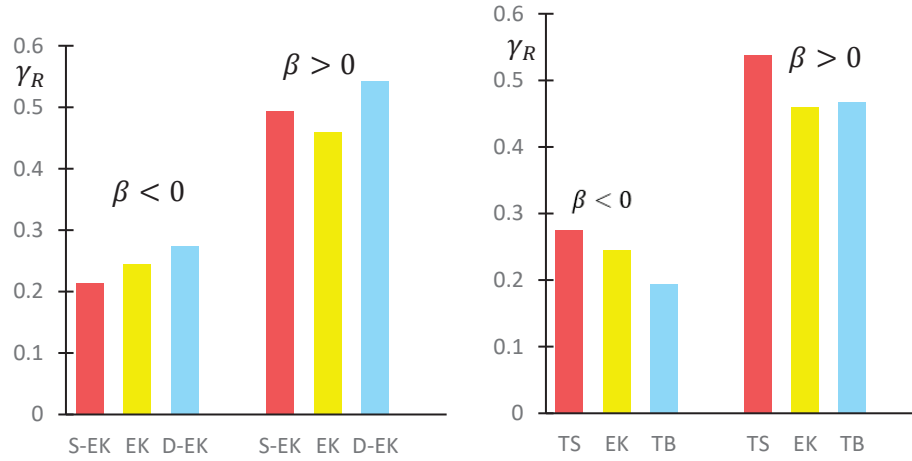


Figure 5.7: Comparison of γ_R in draft and trim series

Figure 5.8 shows the non-dimensional lateral inflow velocity to the rudder $v'_R (\equiv v_R/U_0)$ versus β . As indicated in Eq. 2.13, the slope of v'_R with respect to β is γ_R . The fitting accuracy acceptable.

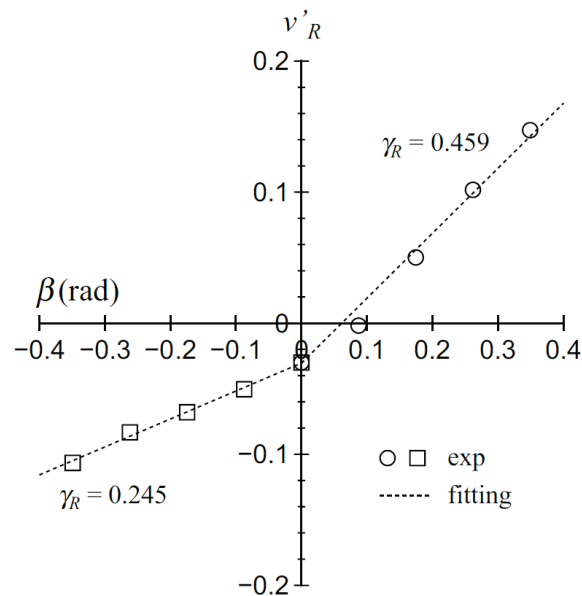


Figure 5.8: Analysis results of lateral inflow velocity to rudder for EK

5.4 OTT and CMT results in Hiroshima University tank test

5.4.1 Maneuvering forces

The results of OTT and CMT are compared in Figure 5.9 for the draft series and in Figure 5.10 for the trim series. The non-dimensional sway force and yaw moment acting on the ship are plotted with respect to the non-dimensional sway velocity and the non-dimensional yaw rate.

The figure contains approximation lines to clarify the trends, which are explained in the next section. The $v' - Y'$ plots in Figure 5.9 shows that the sway force acting on the hull in the pure sway motion increased with the draft, which is apparently correlated with the resultant yaw moment. In terms of the $v' - Y'$ plots in the trim series shown in Figure 5.10, there was no significant difference in the sway force depending on the trim.

In contrast, the resultant yaw moment differed with the trim, which indicates that the acting point of the sway force shifted to some extent. It is assumed to shift forward in TB, which results in a larger yaw moment (i.e., $v' - N'$ plots) because of the longer moment lever. Regarding the pure yaw motion (i.e., $r' - Y'$ and $r' - N'$ plots) in Figures 5.9 and 5.10, the slopes of the sway force and yaw moment were almost linear in the range of target yaw rate on the whole, although this trend was not exactly applied to some cases.

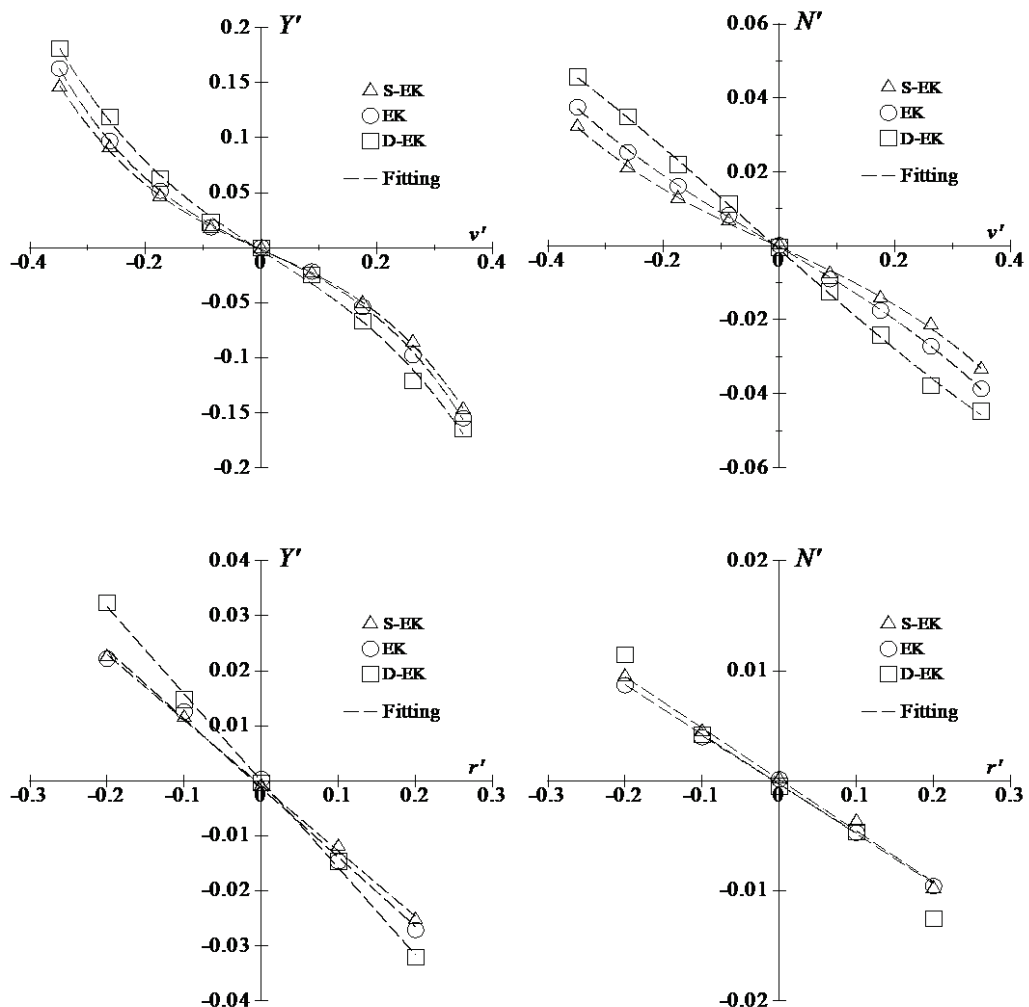


Figure 5.9: Non-dimensional sway force and yaw moment for pure sway motion (top) and pure yaw motion (bottom) depending on the draft

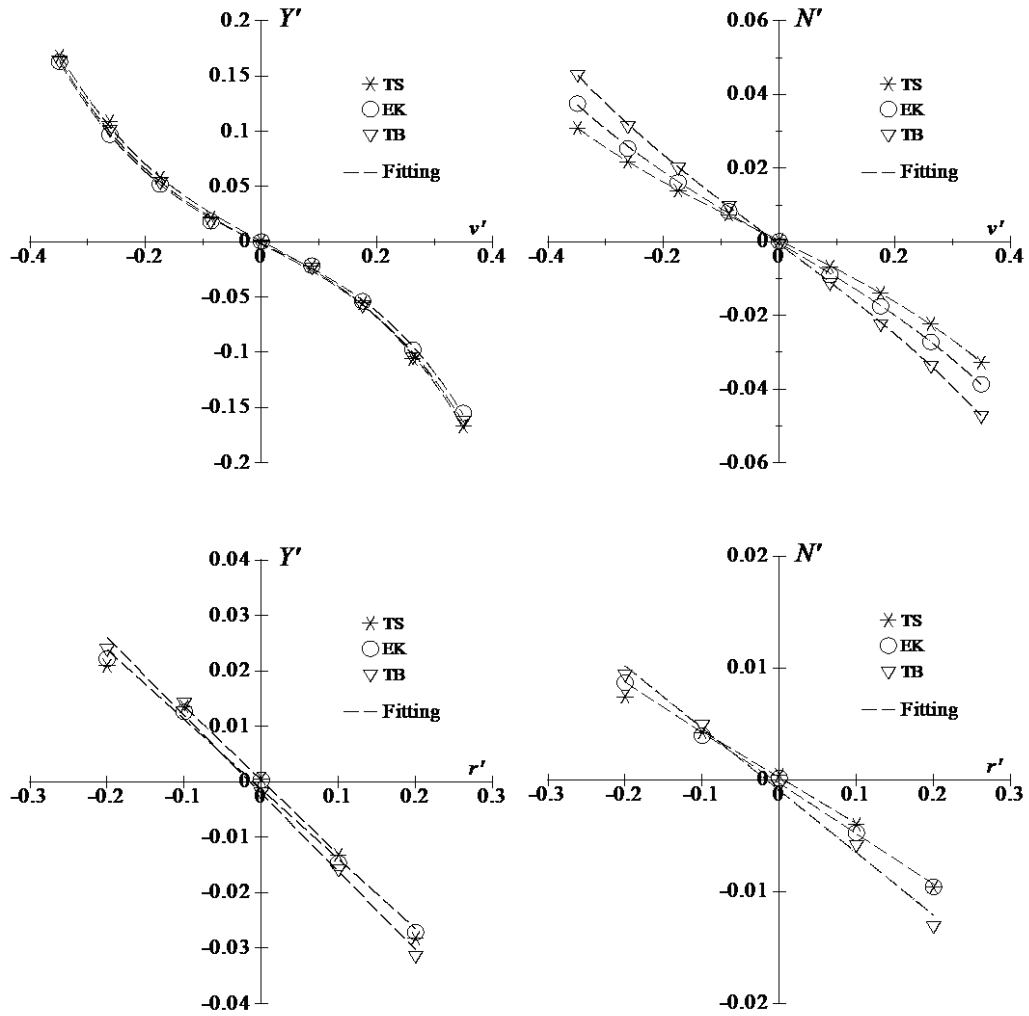


Figure 5.10: Non-dimensional sway force and yaw moment for pure sway motion (top) and pure yaw motion (bottom) depending on the trim

5.4.2 Linear hydrodynamic force derivatives for ship

The linear hydrodynamic force derivatives represent the magnitudes of the sway force and yaw moment proportional to v' and r' . These are the most important components for the yaw-checking on course stability performance, and they are expressed by Y'_v, N'_v, Y'_r^* and N'_r , respectively, where “*” means the derivative includes the centrifugal force component as well. Third-order polynomial equations with respect to v' for the $v' - Y'$ and $v' - N'$ plots and linear equations with respect to r' for $r' - Y'$ and $r' - N'$ plots were assumed to identify these linear derivatives, which were identified by applying the least squares method to the experimental plots. Concerning the $r' - N'$ plot for D-EK and $r' - Y'$ and $r' - N'$ plots for TS, the range of

approximation was adjusted within $|r'| < 0.1$ to improve the approximation accuracy for the linear derivatives. Figures 5.9 and 5.10 contains approximation lines, and Table 5.6 lists the values.

Regarding the draft series, the rates of change in the absolute value of the derivative from EK to S-EK and from EK to D-EK were -7.3% and $+37.3\%$, respectively, for Y'_v . The corresponding rates of change were -22.6% and $+50.9\%$, respectively for N'_v ; -5.4% and $+25.8\%$, respectively, for Y'_r ; and $+3.3\%$ and $+25.7\%$, respectively, for N'_r . Therefore, most of the linear derivatives tended to increase with the draft overall. In particular, N'_v changed significantly with the draft.

Regarding the trim series, the rates of change in the absolute value of the derivative from EK to TB and from EK to TS were 8.8% and 12.9% , respectively, for Y'_v . Meanwhile, the corresponding rates of change were 26.6% and -16.9% , respectively, for N'_v . These results indicate that the longitudinal position of the acting point of the sway force, which was located at the fore of the hull in EK, moved toward the bow with trim by the bow and toward the midship with trim by the stern. The linear derivatives with respect to r' (i.e., Y'_r and N'_r) also showed a correlation with the trim and increased with trim by the bow TB.

Table 5.6: Linear hydrodynamic force derivatives defined at midship.

Symbol	S-EK	TS	EK	TB	D-EK
Y'_v	-0.2288	-0.2788	-0.2469	-0.2686	-0.3389
N'_v	-0.0711	-0.0764	-0.0920	-0.1164	-0.1388
Y'_r	-0.1191	-0.1337	-0.1259	-0.1407	-0.1583
N'_r	-0.0467	-0.0412	-0.0452	-0.0557	-0.0442

5.4.3 Discussion on course stability

The course stability is an important performance indicator related to the ease and safety of ship maneuvering. It is considered as the stability to maintain the straight course while converging a deviation or unsteady motion due to a disturbance at straight running. Therefore, the linear hydro-dynamic force terms acting on the hull plays an important role and the course stability index C'_l which is given by following equation:

$$C'_l = \frac{N'_{rG}}{Y'_{rG}} - \frac{N'_{vG}}{Y'_{vG}} \quad (5.3)$$

This was derived from eigenvalue analysis of the linearized sway and yaw motion equations. If $C_l' > 0$, the ship is considered directionally stable; if $C_l' < 0$, the ship has the unstable course stability. Here, a derivative with the subscript G means that it is defined at the center of gravity. This can be obtained by converting the derivatives at midship:

$$\left. \begin{aligned} Y'_{vG} &= Y'_v \\ Y'_{rG} &= Y'_{r*} + x'_G Y'_v \\ N'_{vG} &= N'_v - x'_G Y'_v \\ N'_{rG} &= N'_r - x'_G Y'_r + x'_G N'_v - x'^2_G Y'_v \end{aligned} \right\} \quad (5.4)$$

The converted derivatives, component terms of Eq. (5.3), and course stability index are listed in Table 5.7.

Table 5.7: Linear hydrodynamic force derivatives defined at the center of gravity, course stability index, and its component terms

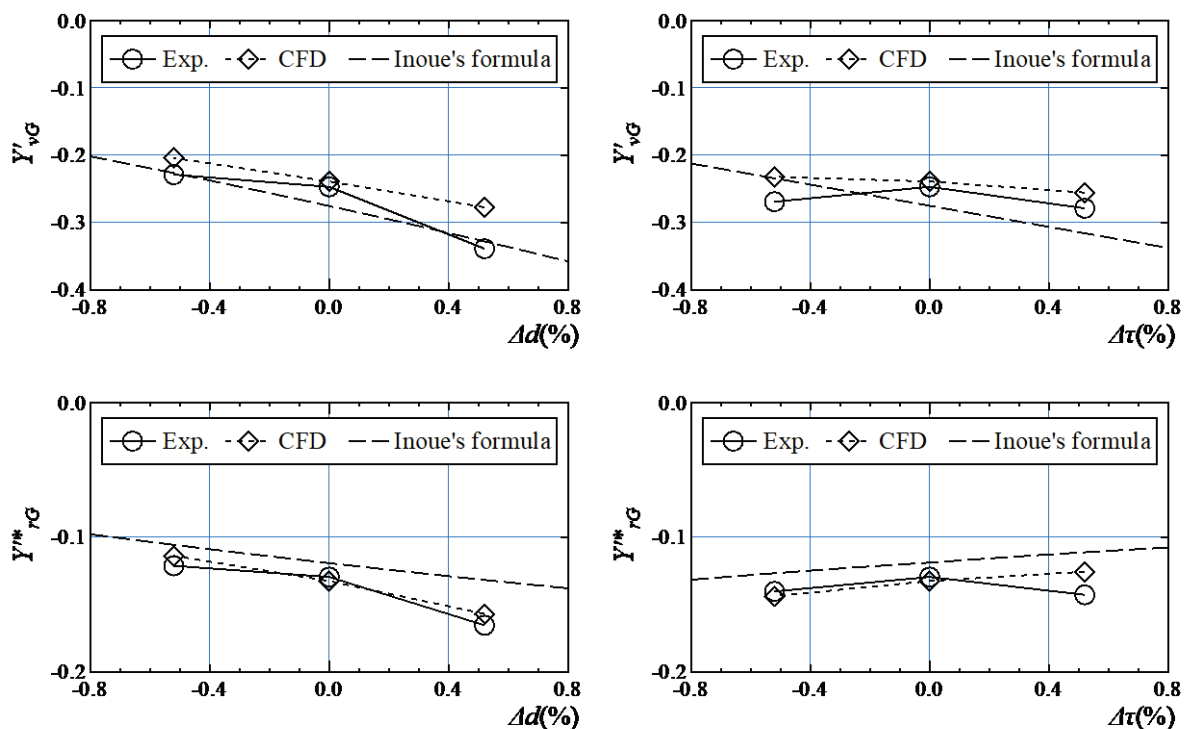
Symbol	S-EK	TS	EK	TB	D-EK
Y'_{vG}	-0.2288	-0.2788	-0.2469	-0.2686	-0.3389
Y'_{rG}	-0.1212	-0.1428	-0.1295	-0.1402	-0.1654
N'_{vG}	-0.0732	-0.0855	-0.0956	-0.1160	-0.1459
N'_{rG}	-0.0485	-0.0484	-0.0485	-0.0553	-0.0506
N'_{rG}/Y'_{rG}	0.3999	0.3391	0.3743	0.3945	0.3058
N'_{vG}/Y'_{vG}	0.3201	0.3067	0.3873	0.4318	0.4304
C_l'	0.0797	0.0324	-0.0130	-0.0373	-0.1246

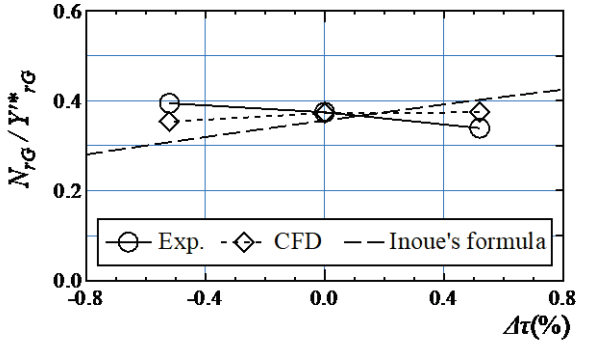
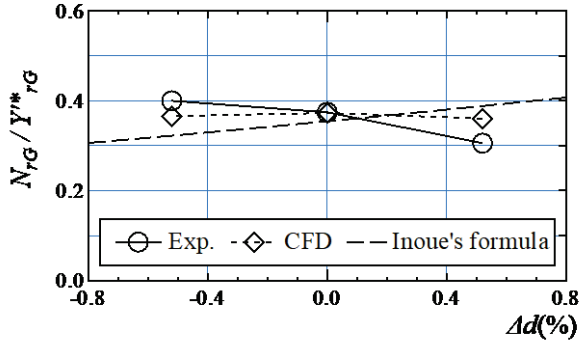
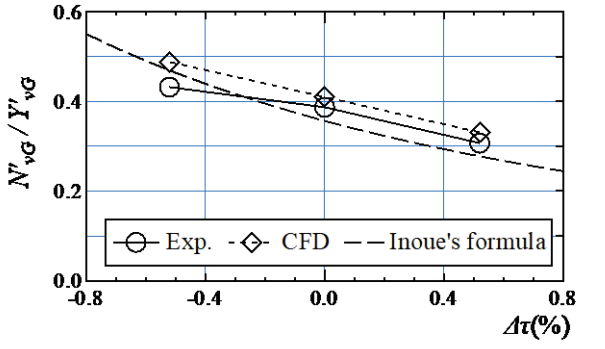
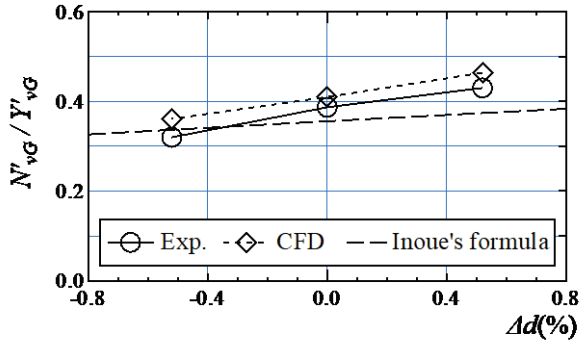
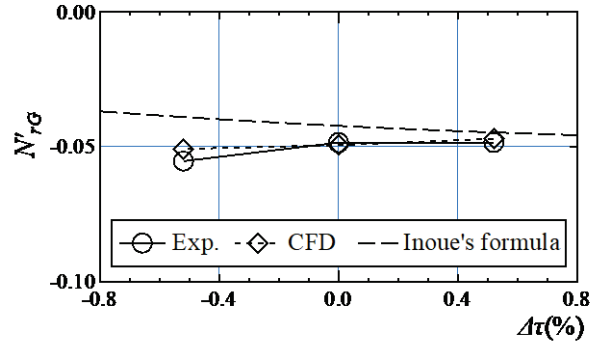
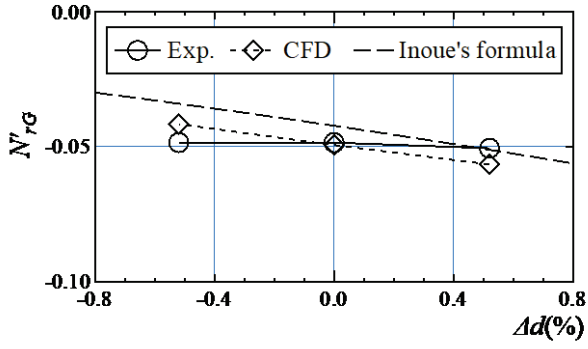
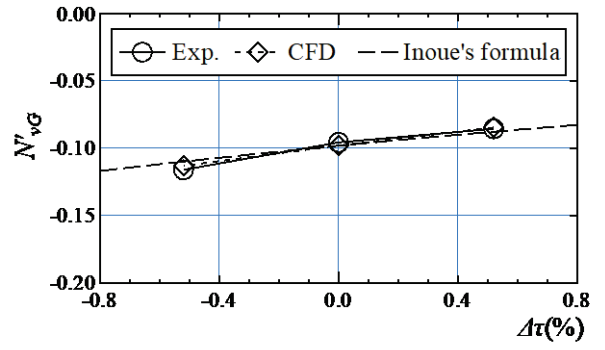
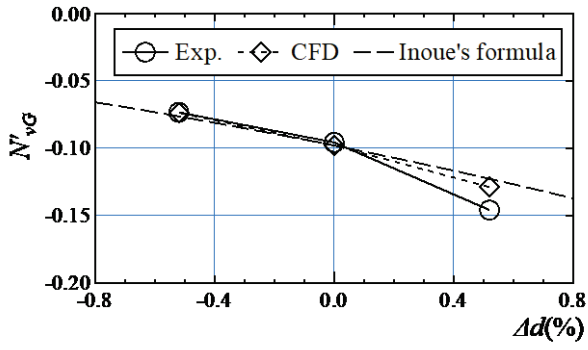
Figure 5.11 plots each linear derivative, the component terms of Eq. (5.3), and the course stability index against Δd or $\Delta \tau$. The results of the above captive model tests are drawn as solid lines with symbols and discussed first. The course stability of ship improved with a shallower draft: S-EK was the most stable, and D-EK was the most unstable. Trim by the stern (TS) also had a positive effect on the course stability, while trim by the bow (TB) had a negative effect. Based on the analysis of Nomoto's formula [40], which expresses the dynamic response of yaw rate to small rudder angle based on the linear equations of motion, the converging yaw rate has been proven to become small as the course stability gets better. Indeed, the results of C_l' for S-EK and TS are consistent with the smaller OSAs observed in the zig-zag tests (indicating better

course stability) and larger tactical diameter in the turning tests (indicating worse turning ability). Thus, even minor changes in the draft and trim that are experienced daily by a container ship affect the maneuverability, which should be kept in mind.

For reference, the result with Inoue et al.'s formula [41] (see Appendix A) are drawn with a thick dashed line in this figure. This is a simplified formula for estimating linear derivatives based only on some principal dimensions and is helpful for immediate estimation. In the case of the trim series, Inoue et al.'s formula indicates that increasing the trim by stern could improve course stability. In the case of draft series, however, Inoue et al.'s formula could not qualitatively capture the experimental tendency (i.e., the course stability deteriorates with increasing draft). This was attributed to the accumulated estimation errors for each derivative. Although Inoue et al.'s formula is a practical approach to estimating the linear derivatives for the maneuvering force and moment, care must be taken when using it to evaluate the course stability in terms of the draft.

Regarding the linear derivatives based on the CFD results, they are drawn as dashed line with symbols and described in the next Chapter 6.





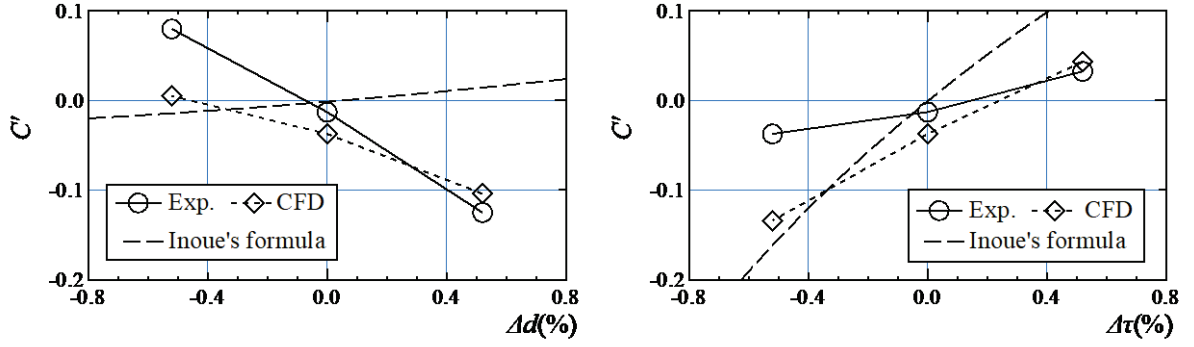


Figure 5.11: Linear hydrodynamic force derivatives, course stability index, and its component terms: draft series (left) and trim series (right)

5.5 OTT and CMT results in JFREA tank

5.5.1 Hydrodynamic forces derivatives for hull

Hydrodynamic derivatives for maneuvering were obtained based on the results of the OTT and CMT. Table 5.8 shows the hydrodynamic derivatives in each loading condition. Figure 5.12 shows the results of X'_H , Y'_H and N'_H versus non dimensional lateral velocity (v'_m) and yaw rate (r'), and the fitting lines by Eq. (2.4). The fitting accuracy is acceptable.

Figure 5.13 shows a comparison of the derivatives for the lateral force (Y) and the yaw moment (N). From Figure 5.13, we can note the following, the absolute value of Y'_{vvr} decreases with increasing draft, but the other derivatives of Y almost the same. On the other hand, there is a clear tendency for some derivatives of N . the absolute values of N'_v and N'_{vvr} increase, and the absolute value of N'_{vvv} decreases with increasing draft. Thus, the effect of the draft appears mainly in the derivatives of N with respect to v'_m . The bow trim tend to increase the absolute value of Y'_{vvv} , Y'_{vvr} and Y'_{vrr} , but the linear term Y'_v and Y'_r do not change significantly. Furthermore, the absolute values of N'_v , N'_r , and N'_{vvv} increase, and the absolute values of N'_{vvr} and N'_{vrr} decrease with an increase in the bow trim. The increase in the absolute value of N'_v owing to the bow trim was remarkable. It is considered that the change of N'_v with the change of the loading condition characterizes the course stability. The effect of the draft and trim changes is significant in N .

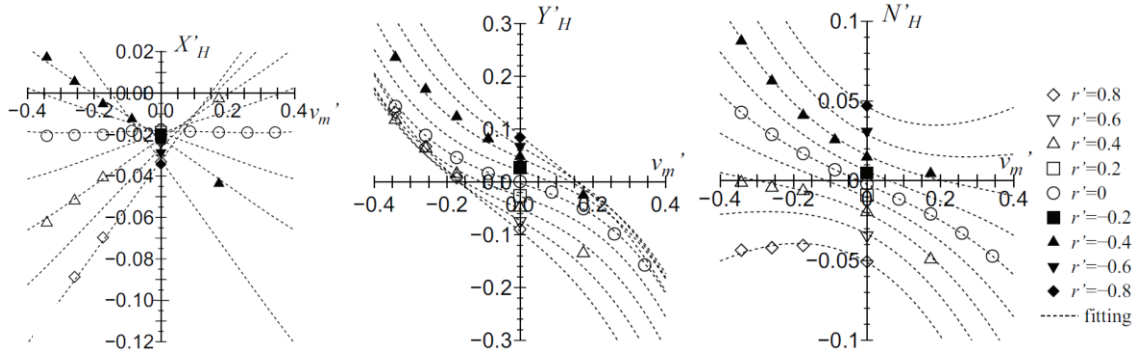


Figure 5.12: Comparison X'_H, Y'_H and N'_H between measured data and the fitting line for EK

Table 5.8: Hull hydrodynamic derivatives on maneuvering in five different loading conditions

Symbol	S-EK	TS	EK	TB	D-EK
X'_{vv}	-0.0252	-0.0219	-0.0185	-0.0265	-0.0426
X'_{vr}	-0.0495	-0.0395	-0.0593	-0.0484	-0.0551
X'_{rr}	-0.0156	-0.0201	-0.0195	-0.0184	-0.0183
X'_{vvvv}	0.1896	0.1538	0.1089	0.1477	0.1077
Y'_v	-0.2254	-0.2298	-0.2246	-0.2250	-0.2419
Y'_r	0.0606	0.0710	0.0664	0.0512	0.0515
Y'_{vvv}	-1.7268	-1.7716	-1.8633	-1.8906	-1.7073
Y'_{vvr}	-0.3790	-0.1545	-0.3691	-0.4291	-0.3342
Y'_{vrr}	-0.5283	-0.4503	-0.5239	-0.5702	-0.6105
Y'_{rrr}	0.0278	0.0318	0.0136	0.0311	0.0316
N'_v	-0.0879	-0.0908	-0.1035	-0.1253	-0.1245
N'_r	-0.0471	-0.0394	-0.0430	-0.0464	-0.0456
N'_{vvv}	-0.2695	-0.1883	-0.2400	-0.2521	-0.1634
N'_{vvr}	-0.5293	-0.5544	-0.5360	-0.5263	-0.5419
N'_{vrr}	-0.0421	-0.0574	-0.0494	-0.0432	-0.0422
N'_{rrr}	-0.0302	-0.0363	-0.0325	-0.0304	-0.0292

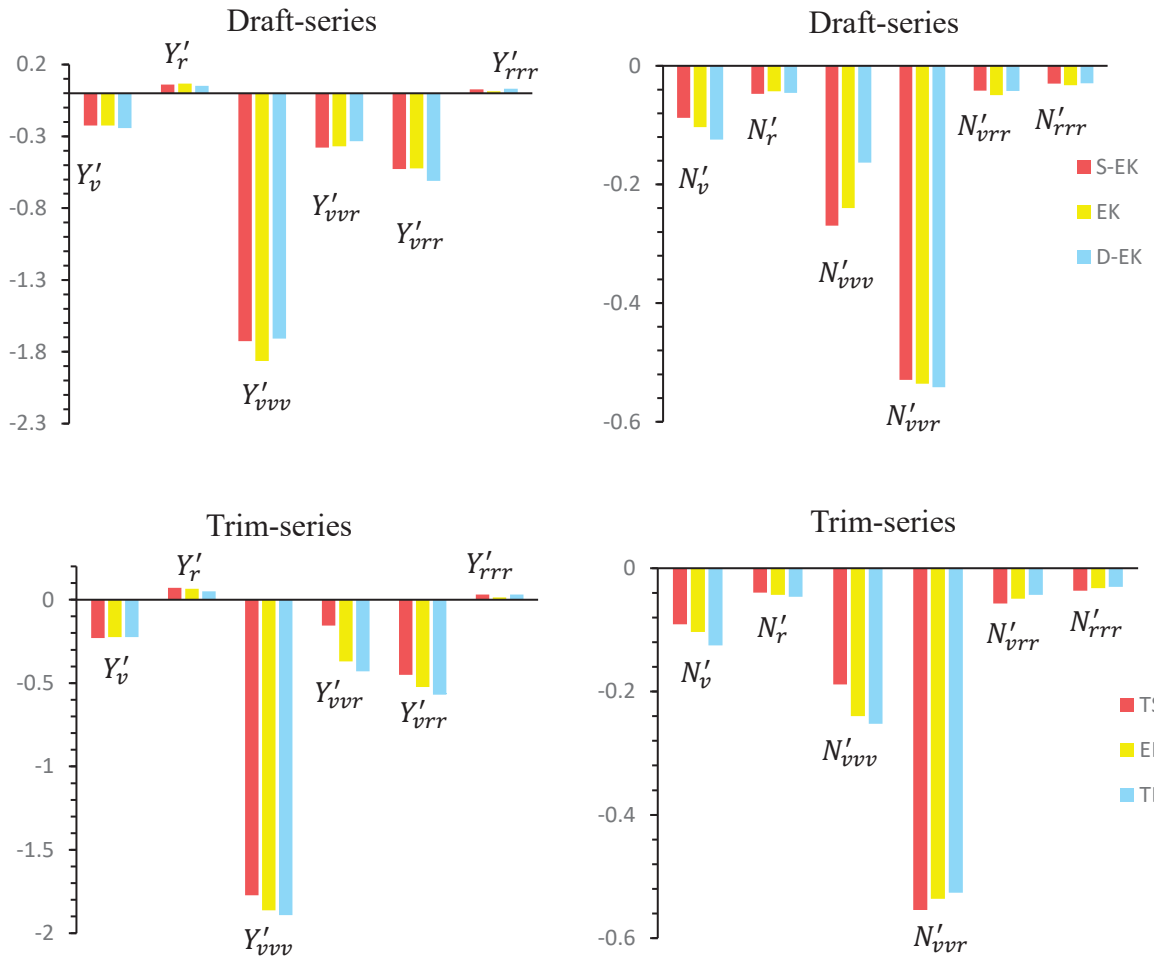


Figure 5.13: Comparison of derivatives of lateral force (Y) and yaw moment (N) in draft series (upper) and trim series (bottom)

Next, Y'_ϕ and N'_ϕ obtained from the hull force test in straight motion are listed in Table 5.9. Figure 5.14 shows a comparison of them. Y'_ϕ is a positive value for the aft trim, but a negative value for the bow trim, which varies greatly depending on the trim. N'_ϕ is negative in any loading condition, which means that the yaw moment with the port turning condition acts on the ship hull when it heels to the starboard side. This tendency is the same as the results for other ships shown by Yasukawa and Yoshimura [42]. There does not seem to be a clear correlation between N'_ϕ and the loading condition.

Table 5.9: Hull hydrodynamic derivatives related to heel angle ϕ in five different loading conditions

Symbol	S-EK	TS	EK	TB	D-EK
Y'_ϕ	0.0074	0.0136	0.0051	-0.0008	0.0112
N'_ϕ	-0.0121	-0.0080	-0.0122	-0.0118	-0.0094

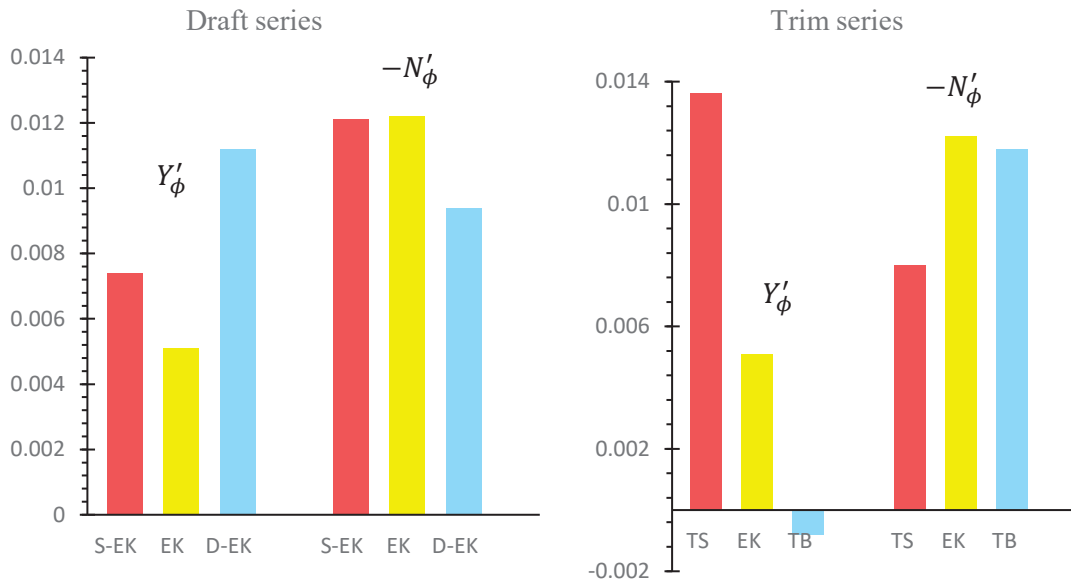


Figure 5.14: Comparison of Y'_ϕ and N'_ϕ in the draft series (left) and trim series (right)

5.5.2 Effective wave fraction in maneuvering motion

Based on the results of the OTT and CMT, the effective wake fraction in the maneuvering motions and the related parameters appearing in Eq. (2.9) were obtained. The obtained coefficients and parameters are shown in Table 5.10. Figure 5.15 shows the comparison of them. The wake fraction in straight motion w_{P0} does not change much with the draft changes but increases when the bow trim is attached. This is a change in the direction of improving ship propulsion performance.

Table 5.10: Parameters for expressing wake fraction in maneuvering motions

Symbol	S-EK	TS	EK	TB	D-EK
w_{P0}	0.360	0.325	0.350	0.375	0.355
w_{Pmin}	0.201	0.170	0.179	0.174	0.157
C_1	-17.9	-18	-19.2	-18.5	-22.4

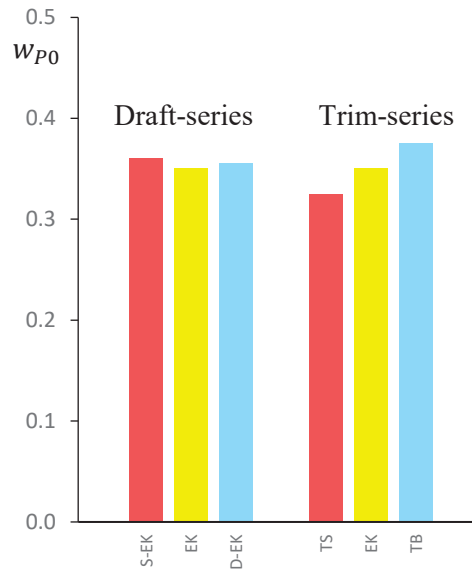


Figure 5.15: Comparison of w_{P0} in draft and trim series

Chapter 6

Numerical Analysis: Mechanism of Course Stability

We performed CFD to understand the mechanism of the course stability, which improved with a shallower draft and larger trim by the stern. Although this may be known empirically, this result has not been explained with consideration of the flow and pressure fields that develop around the hull. The calculation was conducted with the same conditions used in the OTT and CMT experiments.

6.1 Outline of CFD application

6.1.1 Computational domain and boundary conditions

The hydrodynamic forces acting on the ship with the propeller and rudder in pure sway and yaw motions were calculated by CFD. The steady-state solver for incompressible turbulent flow using the SIMPLE algorithm, which is supplied with OpenFOAM ver.5.0: i.e., the open-source CFD toolbox [43] from the OpenFOAM Foundation was adopted. The cell-centered finite volume method was used for discretization in space. The linear-upwind and upwind difference schemes were applied for the convective terms, while the diffusion terms were resolved by second-order central difference scheme. The k - ω SST model was used as the turbulence model. It is a two-equation eddy viscosity model and has been applied popularly in ocean engineering e.g., Chen et.al. [44]. The model variant used in OpenFOAM is based on Menter et.al. [45].

The computational domain with mesh distribution is illustrated in Figure 6.1. A large rectangular domain was discretized for a structured background mesh, and an unstructured hex mesh was generated near the solid object. It was considerably refined, and boundary layer mesh was also added. It resulted in about 10 million for the total number of cells. Because the coordinate system was fixed to the moving hull, the inertial forces generated upon turning, such as the centrifugal and Coriolis forces, were incorporated into the Navier–Stokes equations as body forces. Regarding the propeller effect, a body force model based on a simplified propeller

theory adapted from Yamazaki [46] was considered where the body force distribution was taken from Ohashi et al. [47].

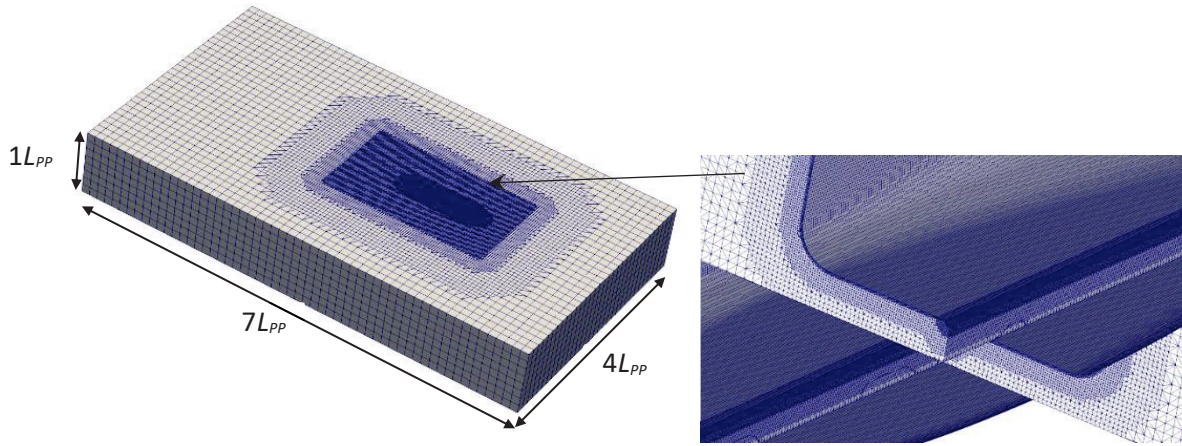


Figure 6.1: Computational domain (Left: Bird's eye view; right: Enlarged view of the hull at the midship)

In terms of boundary conditions, the symmetry plane condition, which specifies that the component of the gradient normal to the plane should be 0, was imposed on the top surface where the free surface elevation was neglected, and the flow below each load waterline was considered. Although it is a simplified assumption, it is rooted in the fact that the lift, which is intrinsically independent of wave-making phenomena, is a primary component of the maneuvering force and moment. Although the CFD results do not include the free surface effect, they can capture the qualitative tendency of the experimental results especially in the range of the small ν' and r' on the whole. Because the linear derivatives of the hydrodynamic force are important to discuss the course stability in the following section, we could expect that this simplified assumption does not have a substantive impact on the discussion.

The flow velocity for each yaw rate was estimated at an arbitrary point and given at the inlet, side, and bottom boundaries. A zero gradient condition was applied to the outlet, and non-slip walls on the hull and rudder surfaces were applied. A wall constraint-type boundary condition was imposed on the turbulent viscosity, a continuous profile to the wall was ensured based on the Spalding's law of the wall.

6.1.2 Calculation condition

The CFD was executed as follows. The ship's speed was set to 0.89 m/s which was the same as the captive model test condition. When determining the MSPP, the wave-making resistance measured in the experiment at the target speed was input and added to the viscous pressure and friction resistances inside the computation. This may be supported by the idea of the three-dimensional method ITTC [48] for a resistance test, in which the total resistance is the sum of independent drag components. We explored the MSPP so as to balance the thrust and total resistance while running straight. This was determined under each loading condition.

Regarding the heel angle, it was set at zero in the calculation. Because the CFD was used to focus on the linear component of hydrodynamic force/moment and to discuss the course stability, the heel angle would not increase within the range of the discussed maneuvers.

6.2 Validation of the hydrodynamic force linear derivatives

The hydrodynamic force derivatives were identified by applying the least-squares method to the calculated data. These are CFD-based derivatives, in contrast to the experiment-based derivatives identified in the captive model tests. They are plotted as "CFD" in Figure 5.11 with dashed lines. The first and second component terms of Eq. (5.1) and the course stability index were calculated using the CFD-based linear derivatives. These are also plotted in the same figure.

Strictly speaking, the CFD-based result could not agree with the experimental results perfectly. There may be several factors, e.g., assumptions or differences in the surface roughness of the model ship. They might have affected the boundary layer development and the stall point on the hull surface, influencing the hydrodynamic forces. Regarding the terms related to yaw motion, the isotropic assumption of $k - \varepsilon$ turbulence model switched in the free stream was a concern for the accuracy because the ship was in the rotational flow. Nevertheless, the CFD-based derivatives apparently capture the overall tendencies of the experimental results, and the resultant CFD-based course stability index also follows the experimental tendencies of the changes in loading conditions. Thus, we could expect the CFD results to be used for explaining the course stability mechanism.

6.3 Effect of draft on hydrodynamic forces and course stability

6.3.1 Longitudinal distribution of the sway force

Figure 5.11 shows that N'_{vG}/Y'_{vG} clearly changes with the draft while N'_{rG}/Y'_{rG} remains almost constant. This indicates that N'_{vG}/Y'_{vG} is key to the deterioration of the course stability with the increasing draft. Because this reflects the longitudinal position of the acting point of the sway force due to pure sway motion, the pure sway case of $\beta = 6^\circ$ or $v' = -0.1$ was discussed here. It was determined as a condition wherein the linear component of the hydrodynamic force terms accounted for the majority of the total force, and as a condition worth discussing the mechanism of linear hydrodynamic force (i.e., linear derivatives) related to the course stability. Figure 6.2 shows the longitudinal distribution of the non-dimensional sway force ($\Delta Y'$). It is related to Y' as follows:

$$Y' = \int \Delta Y' dx' \quad (6.1)$$

A larger sway force acted on every position of the ship hull with a deeper draft (i.e., D-EK). Especially, the peak of the positive force near the bow was significant. Thus, the sway force under the D-EK condition caused a larger clockwise yaw moment (i.e., $N'_{vG}v' > 0$), which explains why N'_{vG} increased in the negative direction. Note that a larger negative value for this derivative is not preferable for course stability because it promotes a yawing motion when the ship sways. Regarding the acting point, it moved closer to the bow with a deeper draft. We also see a positive peak of the sway force around the stern, which was attributed to the rudder in the propeller slipstream. This helped increase the absolute value of $Y'_{vG} (> 0)$ but decrease that of $N'_{vG} (< 0)$ because the rudder force weakens the clockwise yaw moment. Thus, Eq. (5.3) indicates that the rudder presence improved the course stability, but it seems that the effect of the rudder did not differ significantly depending on the draft.

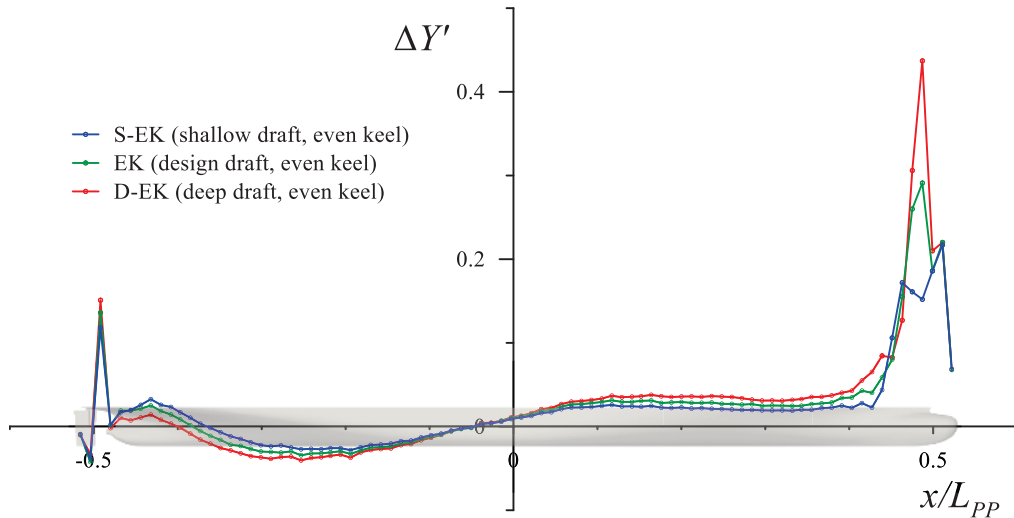


Figure 6.2: Longitudinal distributions of the sway force for the pure sway case of $\beta = 6^\circ$ depending on the draft

6.3.2 Visualization of flow and pressure fields

The friction force component of the sway force must be negligible compared with the pressure force component. To evaluate how a change in the draft affects the hydrodynamic force, Figure 6.3 plots the contours of the fluid pressure coefficient C_p of the pure sway case of $\beta = 6^\circ$ over the hull surface. Positive pressure was spread on the face side around the bow by the incident fluid and the strong pressure acted on the larger area with a deeper draft. Thus, the pressure component in the sway direction $\Delta Y'$ had an impulsive increase around there, as shown in Figure 6.2. A unique difference was observed around the fore shoulder of the hull on the backside, where the negative pressure became intense with an increasing draft. This can be considered as a major component of the lift on the hull, and the reason for the difference of $\Delta Y'$ at the fore of the hull. This phenomenon was evaluated in terms of the flow field. Figure 6.4 illustrates the area in red where the streamlines pass through. It was set at Ord.7 in which the intense negative pressure was observed. The streamlines are drawn in Figure 6.5 and are coloured by the flow speed. Enlarged views of the bow are also drawn in the same figure. The streamlines passing through the specified area seemed to come from above the bow. For D-EK, the flow seemed smooth and greatly accelerated around the fore shoulder of the hull. This indicates intense negative pressure over the hull surface and a large sway force in the positive direction, i.e., $\Delta Y'$ increased. It would be expected to result in a large positive (clockwise) yaw moment. Meanwhile, with a decreasing draft, the bulb seemed to disturb the flow around the

bow. Significant flow separation was observed and ended up weakening the flow acceleration. This caused the small sway force acting there (i.e., $\Delta Y'$ decreased.) and the resultant small clockwise yaw moment. As the results, the absolute values of Y'_{vG} and N'_{vG} decreased in the order of D-EK, EK and S-EK. This result is also correlated with the shift in the acting point, as presented in Table 5.7. This mechanism explains how the draft affects the hydrodynamic forces and moment, ultimately affecting the course stability.

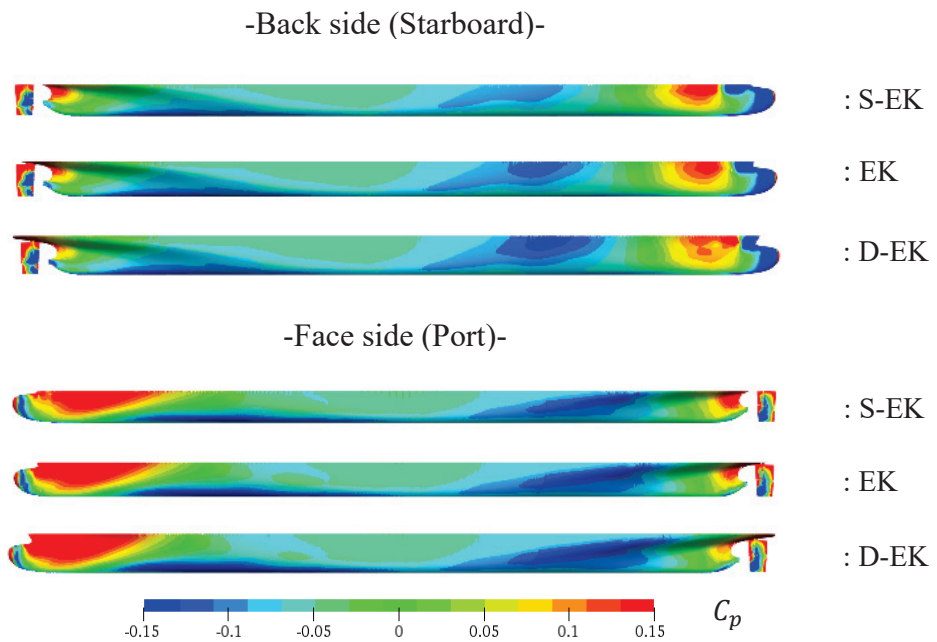


Figure 6.3: Contours of the pressure coefficients over the hull surface for the pure sway case of $\beta = 6^\circ$ depending on the draft

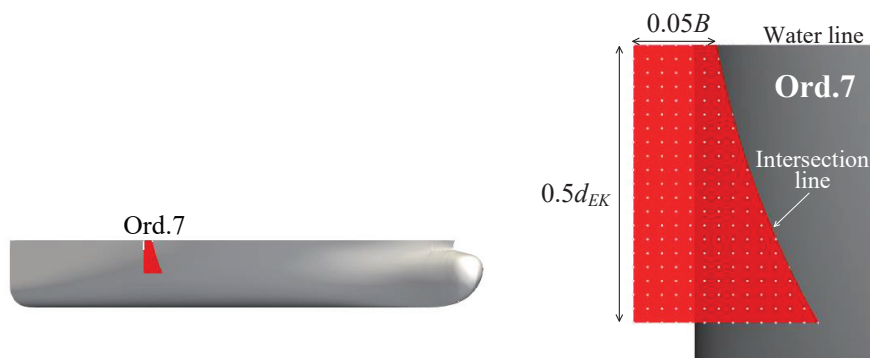


Figure 6.4: Illustration of the area aside the hull where the streamlines pass through (draft series)

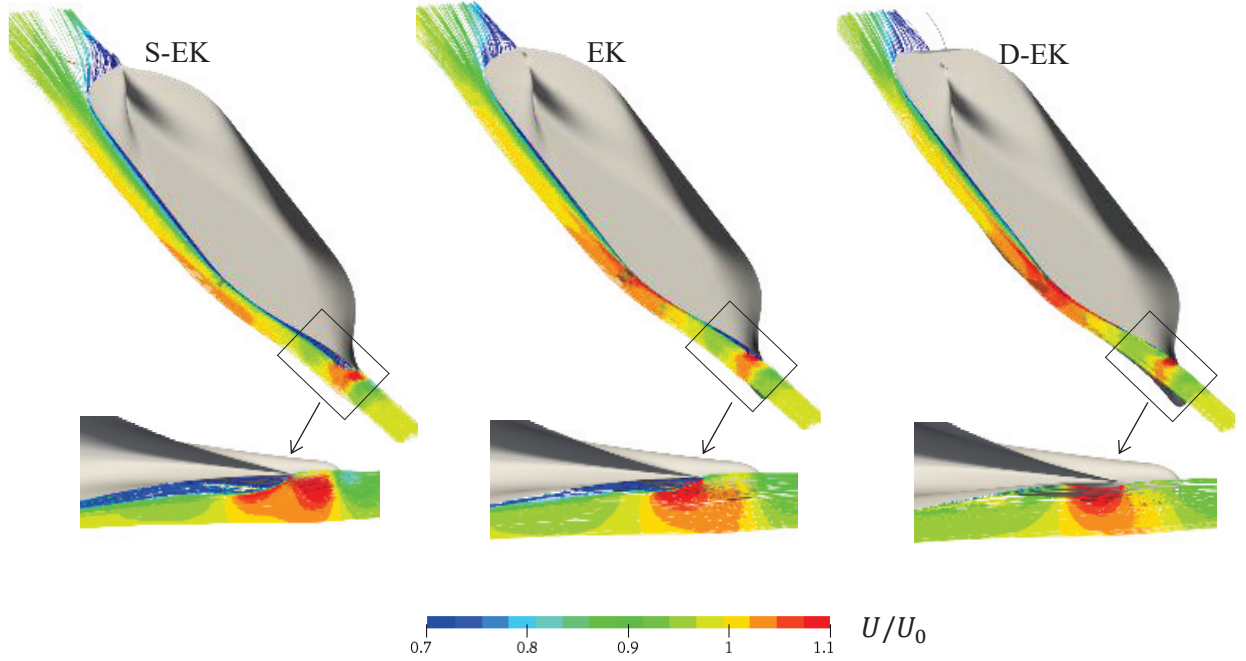


Figure 6.5: Streamlines colored by the flow speed passing near the fore shoulder of the face-side hull in the case of $\beta = 6^\circ$ depending on the draft

6.4 Effect of trim on hydrodynamic forces and course stability

6.4.1 Longitudinal distribution of the sway force

Similar to the draft series, the distribution of the sway force in the longitudinal direction was evaluated among the trim series for the sway case of $\beta = 6^\circ$, as shown in Figure 6.6. $\Delta Y'$ was observed to differ among trim series at the bow, similar to the results for the draft series as shown in Figure 6.2. It depends on the draft at the bow. Because of the large area of the load due to the deep draft at the bow, TB received the largest increase in the sway force there. However, against expectations that $\Delta Y'$ at the fore of the hull would also be largest for TB like D-EK among draft series, it was almost the same for EK and TS at $0.2 < x/L_{PP} \leq 0.4$ and smaller at $0 \leq x/L_{PP} \leq 0.2$. The reason for this is explained in the next section.

At the aft of the hull, the direction of $\Delta Y'$ changed around the midship, and TB had the largest negative value at $-0.3 < x/L \leq 0$. This canceled the positive sway force but increased the clockwise yaw moment. Thus, the ship ended up receiving a nearly equal sway force regardless of the trim, but the difference in the yaw moment increased depending on the trim. This affected N'_{vG} , which had a large negative value for TB that became smaller in the order of

EK and TS, and the acting point of the sway force moved from near the bow for TB towards the midship for EK and TS. This ultimately affected the course stability.

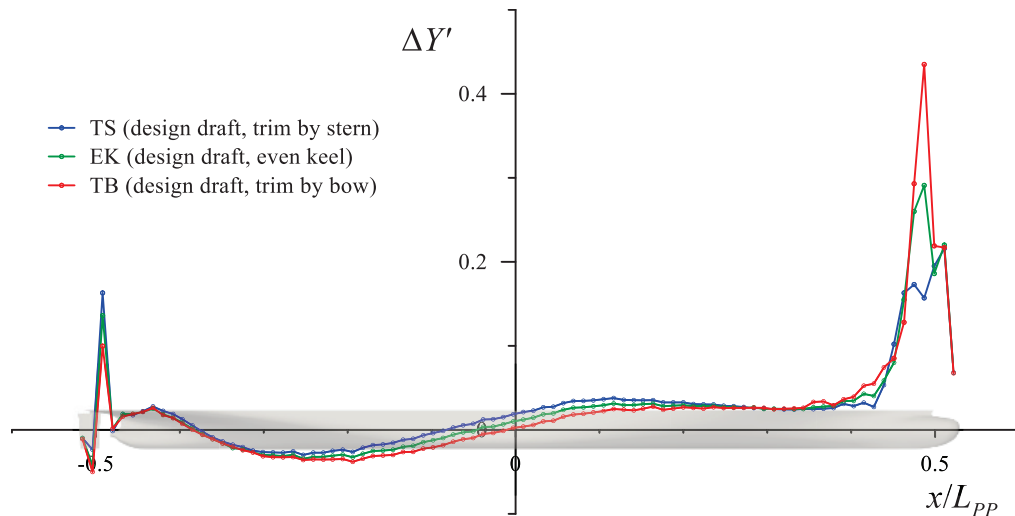


Figure 6.6: Longitudinal distribution of the sway force for the pure sway case of $\beta=6^\circ$ depending on the trim

6.4.2 Visualization of flow and pressure fields

Figure 6.7 plots the contours of the fluid pressure coefficient C_p of the pure sway case of $\beta=6^\circ$ over the hull surface. There were slight differences in the negative pressure area spread over the fore shoulder of the hull on the backside, depending on the trim. The same explanation as Section 6.3.2 is given for the reason why TB, which had a sufficiently submerged bulb like D-EK, had the large negative pressure area there. This must have increased $\Delta Y'$. However, in trim series, it is thought that the negative pressure developed around the bilge in a similar longitudinal range on the face-side was dominant for TB, which reduced the positive sway force. This resulted in $\Delta Y'$ for TB equivalent to other trim conditions or lower than them at $0 < x/L_{PP} \leq 0.4$, as shown in Figure 6.6.

To evaluate the pressure mechanism, we set a certain area at Ord. 7 1/2, as shown in Figure 6.8. This corresponded to the center of the target negative pressure area around the bilge on the face-side, and the streamlines passing through this area are drawn in Figure 6.9. The flow seemed to become fast in the order of TS, EK and TB when going around the bilge. This may be related to the inflow angle to the bottom surface which depended on the bottom depth and its

inclination. Thus, the resultant negative pressure area widened in the same order, especially larger in TB as observed in Figure 6.7.

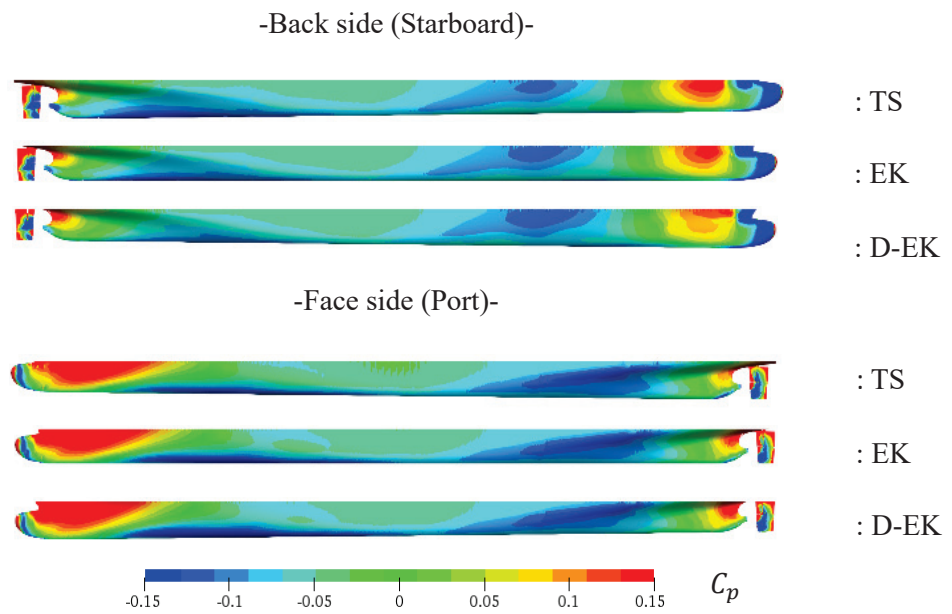


Figure 6.7: Contours of the pressure coefficients over the hull surface for the pure sway case of $\beta = 6^\circ$ depending on the trim

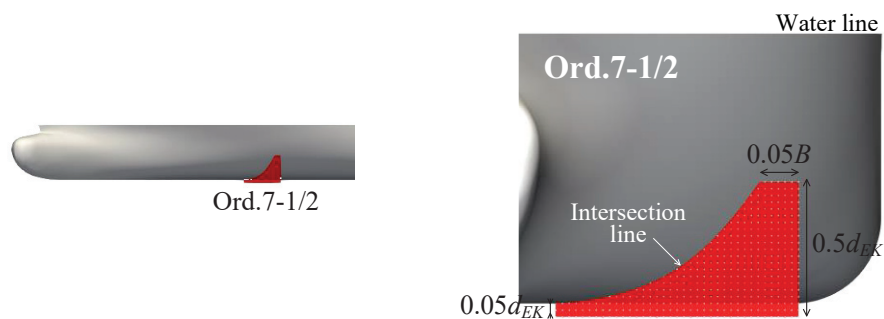


Figure 6.8: Illustration of the area aside the hull where the streamlines pass through depending on the trim

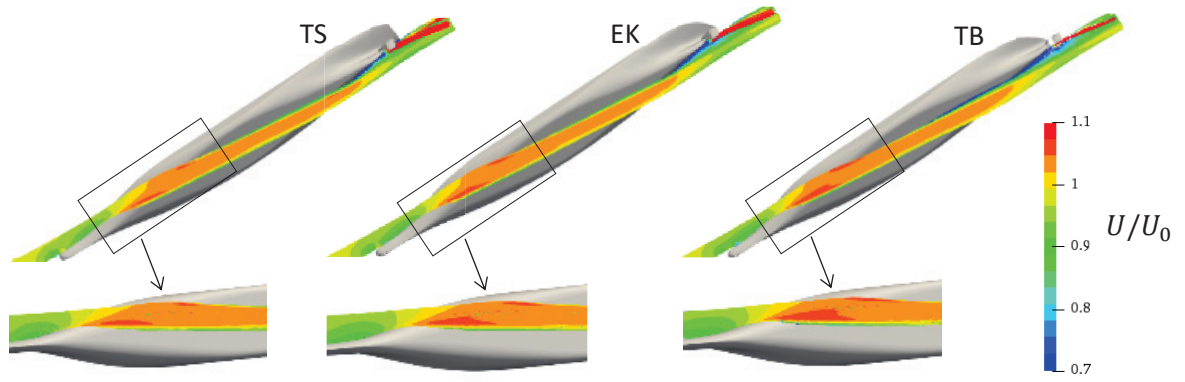


Figure 6.9: Streamlines colored by the flow speed passing around the bilge of the back side in the case of $\beta = 6^\circ$ depending on the trim

Chapter 7

Simulation Study: Maneuvering Simulation

In this chapter, a simulation study for maneuvering was discussed. The parameters used for maneuvering simulations were performed. In order to validate the model-scale simulations, the results were compared to the free-running model tests result. Some real-scale simulations were also presented.

7.1 Parameters and coefficients used for simulations

The captive model test results described in Chapter 5 were used for the maneuvering simulations. Other coefficients and parameters not yet mentioned are as follows:

- Hull resistance was calculated by a 3-dimensional extrapolation method based on Schonherr's frictional resistance coefficient formula. The wave-making resistance coefficient and form factor for the ship hull under different loading conditions were obtained by resistance tests.
- The k_0 , k_1 and k_2 appearing in Eq. (2.7), which represent the open water characteristics of the propeller thrust, were set to 0.4738, -0.3603, and -0.1480, respectively, based on the propeller open water test results.
- The radius of roll gyration including the added moment of inertia component, k_{xx}^* , was determined by the roll decay test. They are shown in Table 7.1.
- The added mass for surge and sway (m_x and m_y), and the added moment of inertia for yaw (J_{zz}) were obtained by the 3D panel method based on the potential theory [49]. They are shown in Table 7.2. the added mass is non-dimensionalized by division of $(1/2)\rho L^2 d_m$, and the added moment of inertia is non-dimensionalized by the division $(1/2)\rho L^4 d_m$.
- The non-linear hydrodynamic derivative terms with respect to ϕ and the vertical height of the lateral force acting on the hull z_H/d_m were estimated using the method described in the paper of Yasukawa et.al [50].

- The effective longitudinal coordinate of the rudder position l'_R was assumed to be -0.8 in all loading conditions referring to the captive model test result for a pure car carrier by Yoshimura [51].

Table 7.1: Radius of roll gyration including added mass component in five different loading conditions for the model-scale ship

Symbol	S-EK	TS	EK	TB	D-EK
k_{xx}^*/B	0.454	0.518	0.494	0.456	0.466

* Added moment inertia component was included.

Table 7.2: Added mass coefficients in five different loading conditions

Symbol	S-EK	TS	EK	TB	D-EK
m'_x	0.0056	0.0055	0.0061	0.0056	0.0066
m'_y	0.1373	0.1382	0.1521	0.1394	0.1676
J'_{zz}	0.0082	0.0082	0.0089	0.0084	0.0097

7.2 Validation of the maneuvering mathematical model

The $\pm 35^\circ$ turning tests were simulated for each loading condition shown in Figure 7.1, which solid line represents the calculation and dashed line represents the experimental result. Their trajectories are compared with the experimental results in Figure 7.2. The initial speed was 0.86 (m/s). Evidently, the simulation results captured the difference in trajectories due to the difference in draft and the difference in trim observed in the experimental results. Thus, confirming the validity of the manoeuvring mathematical model of the subject ship. Meanwhile, Figure 7.3 shows a comparison of advanced A_D , and tactical diameter D_T . The horizontal axis in Figure 7.3 is a change ratio of the draft Δd or a change ratio of the trim $\Delta \tau$.

The simulated trajectory roughly agrees with the free-running test result for different loading conditions, although there is a tendency that the simulated advanced (A_D) is generally smaller than that in the experiment. This tendency is significant for D-EK, so the simulation accuracy becomes worse. However, the simulations correctly capture the tendency of the turning radius to become small with increasing the draft (from S-EK to D-EK) or decreasing the trim (from TS to TB). The simulations also roughly capture the test results for changes in the turning indices

(A_D, D_T) with changes of the draft and the trim. The present simulation method has enough accuracy in practice.

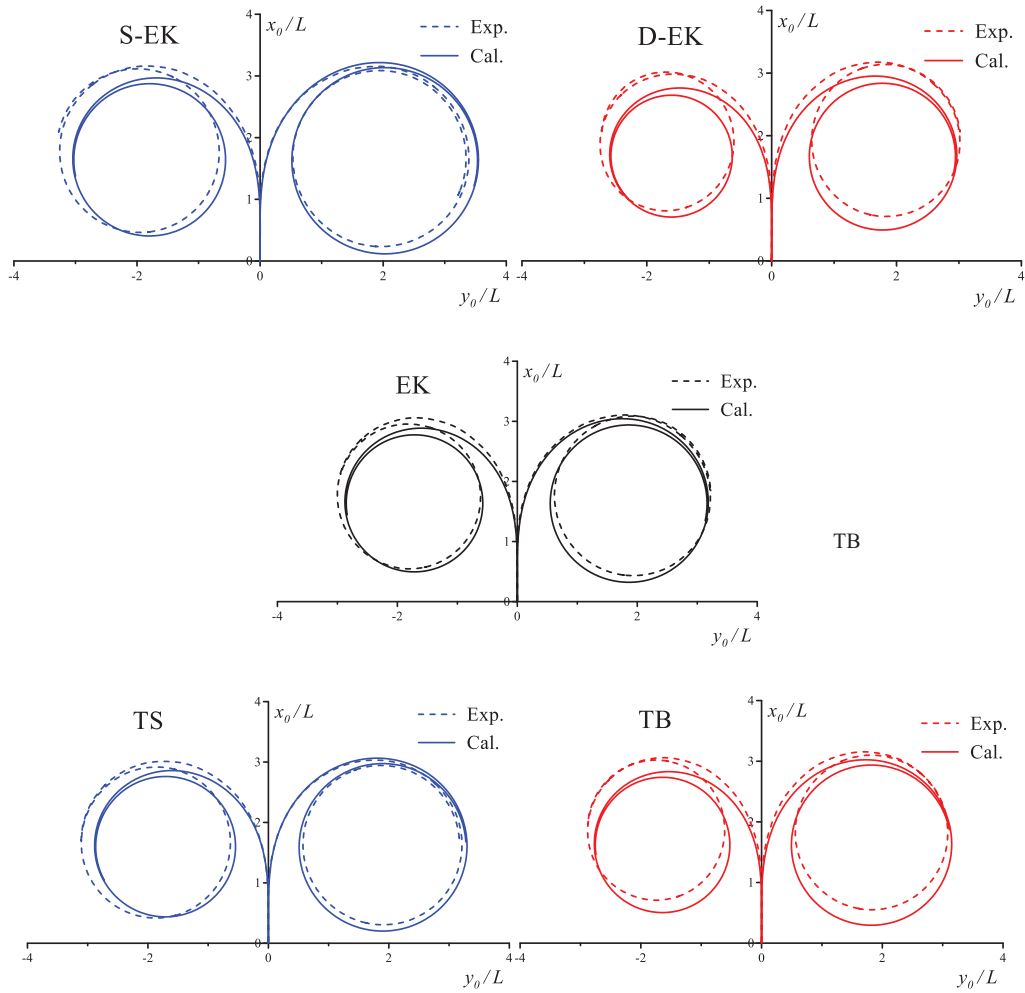


Figure 7.1: $\pm 35^\circ$ turning trajectories of each loading condition.

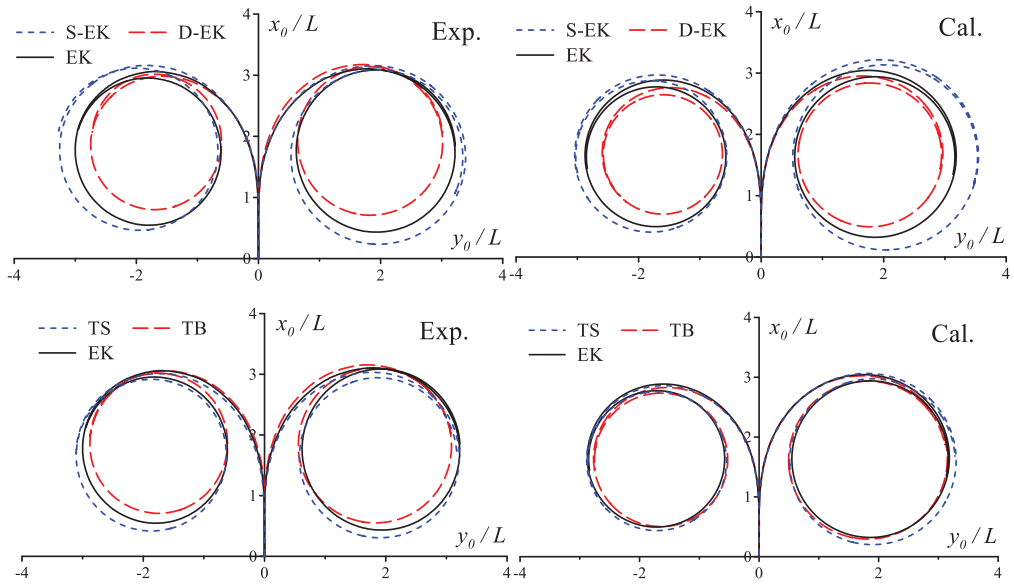


Figure 7.2: Comparison of $\pm 35^\circ$ turning trajectories among draft-series conditions (upper) and trim-series (lower) between the free-running experiment and simulation

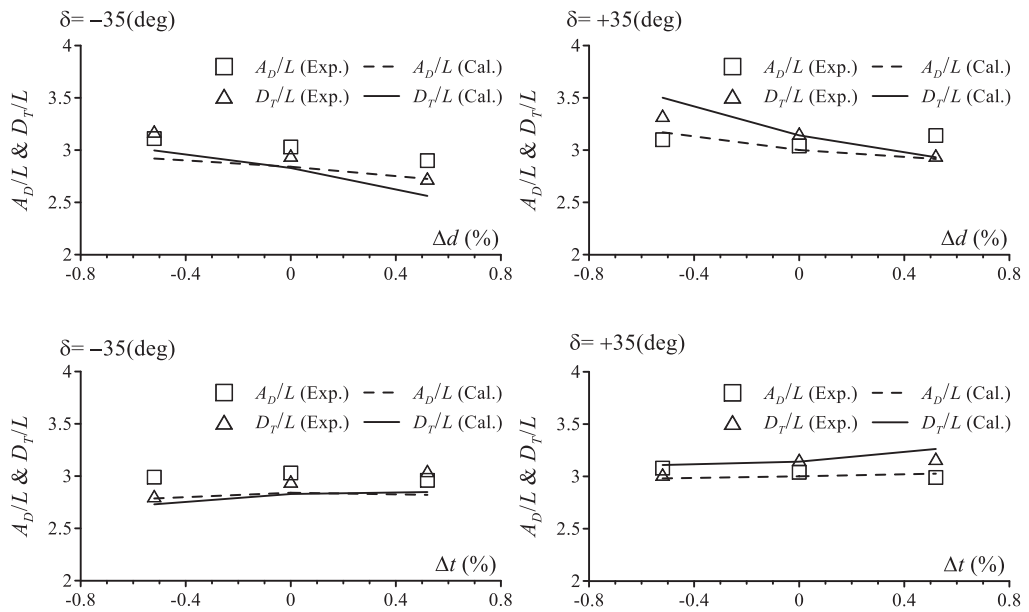


Figure 7.3: Comparison of A_D/L and D_T/L in $\delta = \pm 35^\circ$ turning

Figure 7.4 and 7.5 shows the comparison of time histories of heading angle ψ , rudder angle δ between experiment and calculation of +10Z and -10Z. Figure 7.6 shows the comparison of the overshoot angles (OSAs) of 10Z and -10Z. in the figure, OSA 1 is the 1st overshoot angle, and OSA2 is the 2nd overshoot angle. The simulation results of OSA2 for 10Z and OSA1 for -10Z, during the heading changes from negative to positive, agree well with the free-running test result

under any loading conditions. On the other hand, the simulated OSA during the opposite heading change from zero to positive is smaller than the free-running test result. However, the present simulation captures the tendency of the OSA to increase with increasing draft or trim by bow. The present simulation method also has sufficient accuracy for the zigzag maneuver in practice.

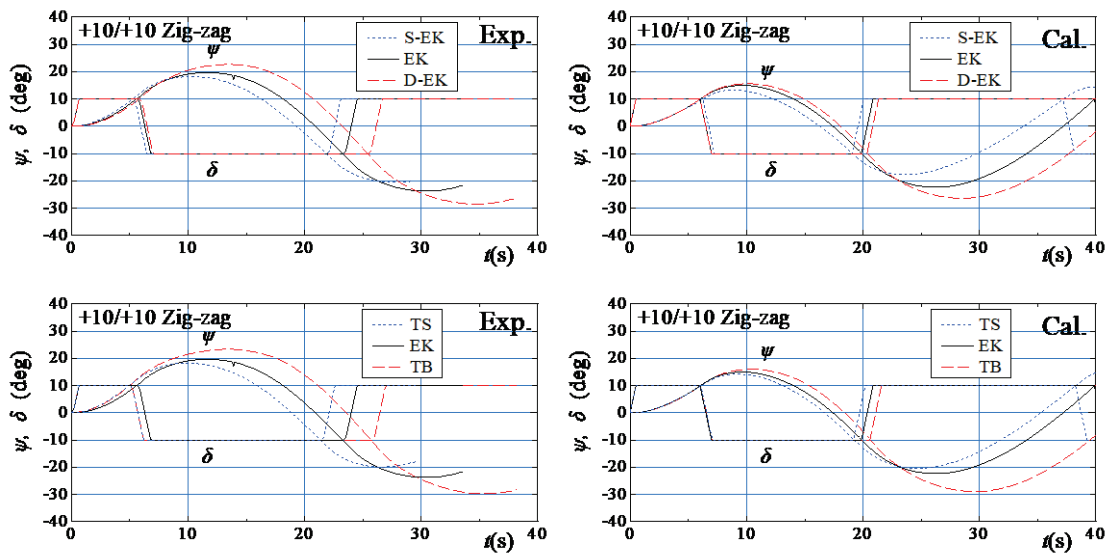


Figure 7.4: Comparison of time histories of ψ and δ of $10^\circ/10^\circ$ zig-zag maneuvers between experimental and calculation

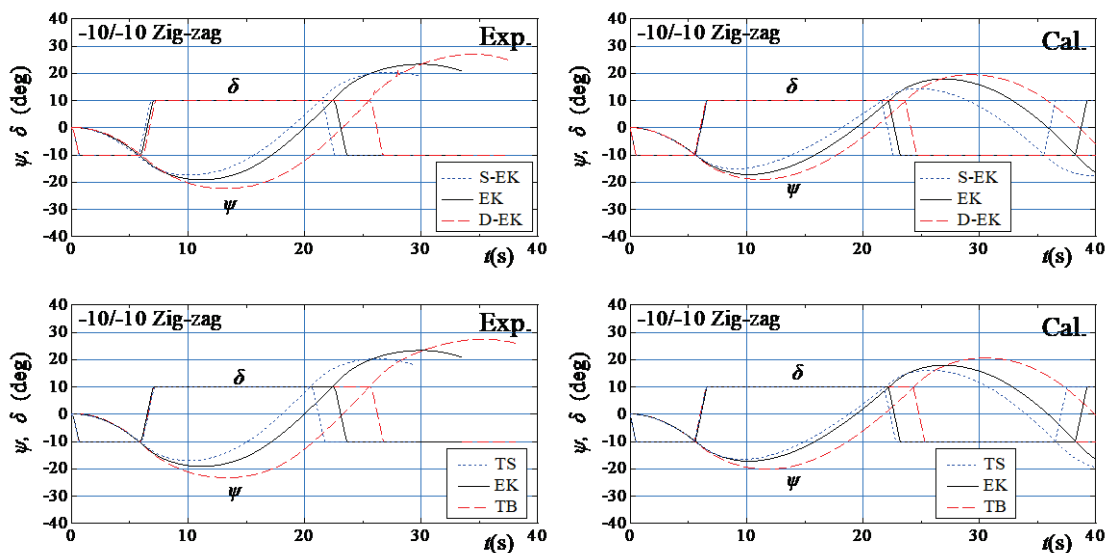


Figure 7.5: Comparison of time histories of ψ and δ of $-10^\circ/-10^\circ$ zig-zag maneuvers between experimental and calculation

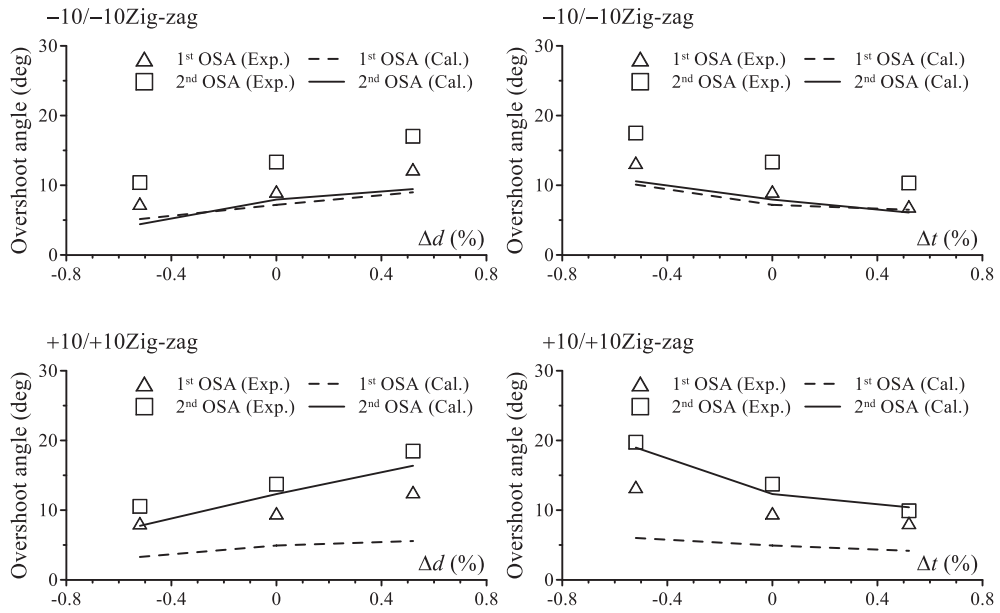


Figure 7.6: Comparison of overshoot angles of $\pm 10^\circ$ zig-zag maneuvers

7.3 Real-scale maneuvering simulations

The maneuvering motions in the real scale are discussed. Every model-scale dimension, including the loading conditions, was converted to the real-scale one. The roll-motion characteristics, such as \overline{GM} and k_{xx} which were designed for the real-scale ship in Chapter 3, were adopted. The total resistance coefficient was calculated using a three-dimensional extrapolation method for the real-scale simulation, considering the viscous resistance based on the Reynolds number of the real-scale ship. The wake fraction factor of the scaled model was also converted to a real-scale value using the ITTC formula [48]. Besides, in the real-scale simulation, the wind force due to self-propulsion was considered. Note the results of the model-scale simulation were cited from sub-section 7.2 just for reference.

7.3.1 Straight motion

Before the maneuvering calculations, a simulation with straight motion was performed. The ship speed was set at 14.5(knot). It corresponded to 0.86 (m/s) in the model scale and was used in the free-running model test. The propeller revolution in each loading condition was determined respectively, so the ship speed would be this target speed. Table 7.3 shows the calculation results

of the number of propeller revolutions. TS with a trim by stern and D-EK with a deeper draft needed to increase the number of propeller revolution to achieve the target speed, while the smaller n_p than that of EK was enough for TB with trim by bow. Since the bow is not fully submerged in S-EK, the expected large wave-making resistance mainly caused a bit more n_p than that of EK. The values shown in Table 7.3 are used as the number of propeller revolutions for the turning and zig-zag maneuver simulations.

Table 7.3: Number of propeller revolution (n_p) in five different loading conditions

Symbol	S-EK	TS	EK	TB	D-EK
n_p [rps]	1.039	1.054	1.025	1.005	1.045

7.3.2 Turning motion

Figure 7.7 shows a comparison of $\delta = \pm 35^\circ$ turning trajectories for the real-scale ship at 14.5 kt. The turning radius increases with decreasing draft. This is because the course stability is improved with decreasing draft, as shown in Figure 5.11. The hull hydrodynamic force characteristics during maneuvering, which determine the course stability, change with the loading condition. The CFD result shows that changes in the bow shape and the hull form curvature with the loading condition changes are deeply involved in the hydrodynamic force characteristics. In addition, the turning radius tends to decrease slightly in the case of bow trim, but this is not remarkable. Analysis of the course stability based on the captive model test results shows a tendency for course instability with the bow trim (Figure 5.11). Since the hull drift angle and the yaw rate are relatively large in turning motion with a rudder angle of 35° , the turning performance changes may not be fully explained by the course stability analysis based on the linear theory. In the trim-series, it is considered that the change of the hull resistance characteristics during maneuvering (X'_{vv}, X'_{vr} , etc. in Table 5.8), which is not accounted in the course stability analysis, is influenced by the turning characteristic change.

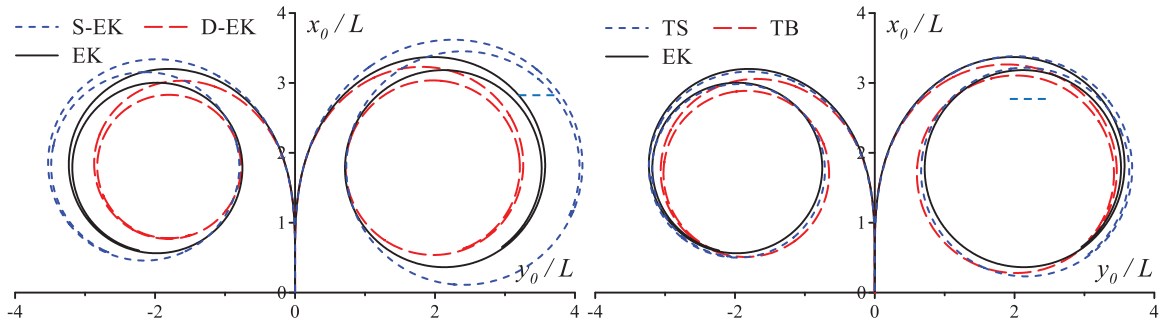


Figure 7.7: Trajectories of $\delta = \pm 35^\circ$ turning in the real scale

Figure 7.8 shows a comparison of advance A_D , and tactical diameter D_T at 14.5(kt). In the figure, the simulation results of both the real-scale and model-scale ships are plotted. They are obtained from the results of Fig. 7.7 and Fig.7.2, respectively. Note their differences are caused by the scale effect on the friction resistance and the wake. Besides, since the real-scale ship has considered a realistic superstructure and container arrangement, the difference in the roll-motion characteristics such as \overline{GM} and k_{xx} affects the results.

The tendency of the draft and trim effects on the advance and tactical diameter is similar between the real-scale and model-scale ships. In the draft series, A_D/L and D_T/L decrease linearly with the draft increase (Δd), improving the turning performance. Meanwhile, in the trim series, it does not change significantly with respect to the trim ($\Delta\tau$). The results of the real-scale ship indicate larger A_D/L and D_T/L than those of the model-scale ship overall. It is because the propeller load at the self-propulsion point of the real-scale ship is smaller than that of the model-scale ship. It results in decreasing the propeller slipstream to the rudder, and the resultant rudder force is reduced.

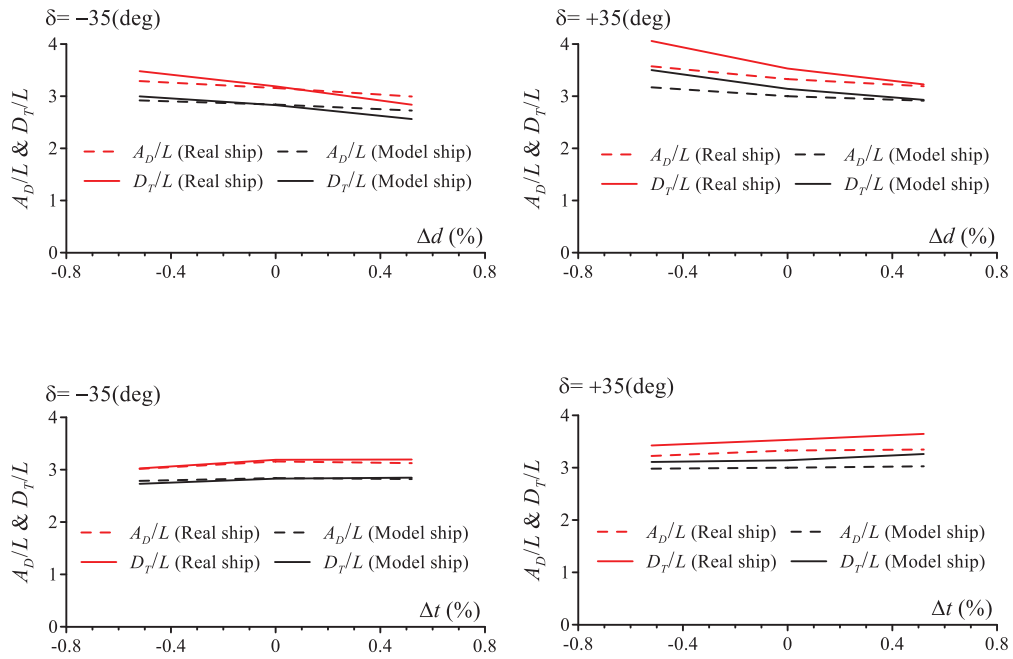


Figure 7.8: Comparison of advance and tactical diameter of $\delta = \pm 35^\circ$ turning between the real-scale and model-scale ship

Figure 7.9 shows the time history of the roll angle ϕ during $+35^\circ$ turning of the real-scale ship. The negative value means outward roll. The peak of ϕ appears immediately after steering, and it converges to a certain outward heel angle during the steady turning. D-EK shows the large absolute value of ϕ because of the small \overline{GM} (designed in Table 3.4). The bow-trim TB also indicates the large absolute value of ϕ . This is because not only the \overline{GM} is small but also Y'_ϕ becomes negative with the trim by bow, as shown in Table 5.9: and the resultant restoring moment calculated by $(mg\overline{GM} + Y_\phi z_H)$ decreases. Regarding S-EK, the roll angle does not occur so much during turning because of the large \overline{GM} .

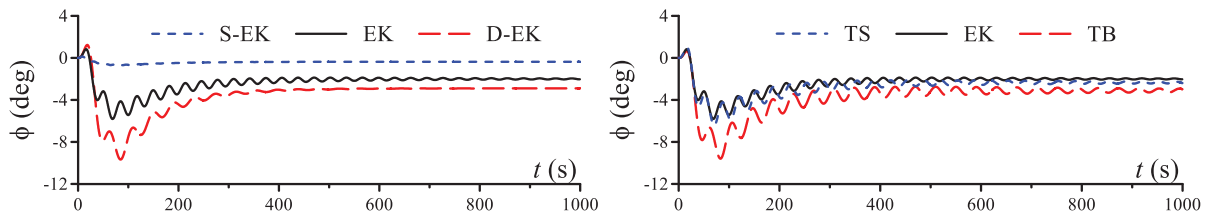


Figure 7.9: Time histories of the roll angle of $\delta = +35^\circ$ turning in the real scale

7.3.3 Zig-zag maneuver

Figure 7.10 shows a comparison of the time histories of heading angle ψ and rudder angle δ of 10Z and -10Z for the real-scale ship at 14.5(kn). To capture the characteristics, the 1st and 2nd overshoot angles (OSAs) were obtained and compared in Figure 7.11, in which the simulation results of both the real-scale ship (Fig.7.10) and model-scale ship (Figs.7.4 and 7.5) are plotted. From this figure, the deeper draft and the bow trim make the OSA large. This tendency is the same in the results for both the real-scale and model-scale ships. But the OSAs of the real-scale ship are larger than the model-scale ship especially, in D-EK and TB. This is because the roll angle increased in D-EK and TB since their \overline{GM} in the real scale were designed small, and the ship became course unstable due to the coupling effect with the roll [42].

Thus, when the draft is deeper, or when the bow trim is attached to the ship, the controllability may deteriorate to the extent that the OSA increases. The ship operator should be aware that the maneuverability of large container ship changes significantly due to the loading condition changes.

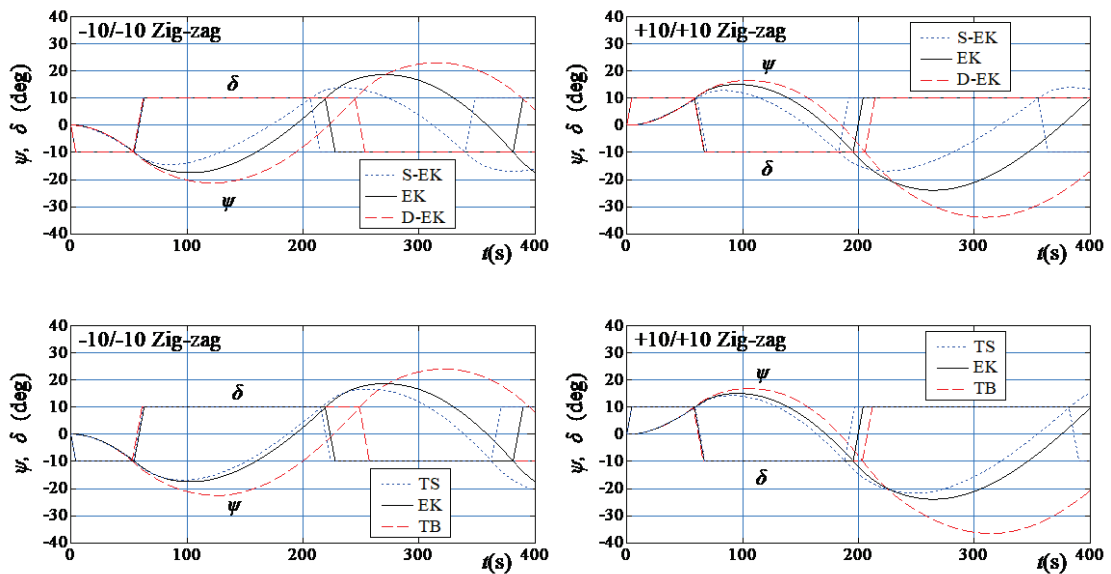


Figure 7.10: Time histories of ψ and δ of $\pm 10^\circ/\pm 10^\circ$ zig-zag maneuvers in the real scale

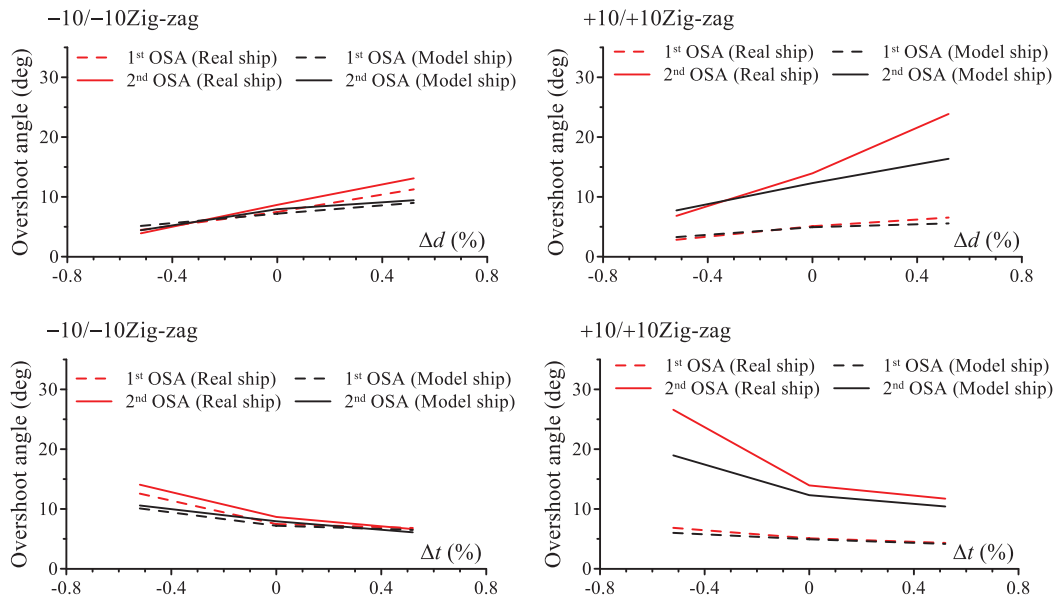


Figure 7.11: Comparison of overshoot angles of $\pm 10^\circ/\pm 10^\circ$ zig-zag maneuvers between the real-scale and model-scale ship

Chapter 8

Simulation Study: Course-keeping Simulation Under Wind Disturbance

The authors have discussed the influence of loading conditions on course stability based on eigenvalue analysis, considering the linear hydrodynamic force terms acting on the hull. It was found that even a slight change in the draft and trim from the standard EK impacted the course stability. In this chapter, based on a real-scale, a course-keeping simulation was executed to investigate how the ship maneuvers according to the loading conditions and how the motion changes depending on the wind disturbances. PD (Proportional-Derivative) control with respect to the heading angle and yaw angular velocity was adopted. All the calculations were conducted in real scale. The way to run the real-scale simulation can refer to section 7.3.

8.1 No true wind condition

First, only the wind due to self-propulsion was considered, that is, the no true wind condition. The situation in which the ship with the initial heading angle (ψ_0) of 5° at the initial ship speed (U_0) of 24 (kt) attempted to adjust the heading angle to 0° using the PD controller was considered. Figure 8.1 shows the time series of the heading angle (ψ) of the ship under different loading conditions, where the black line shows the result of the proportional control, that is, proportional gain 1 and derivative gain 0. Because this is the most basic steering pattern, the ship's inherent course stability is intensely reflected in the resultant maneuvering motions.

The initial heading angle converges in EK, S-EK, and TS. Especially, it converges soon in the case of S-EK. Meanwhile, it gradually diverges in the deep-draft condition, D-EK, and the trim by bow condition, TB. The authors previously discussed the influence of the loading conditions (i.e., draft and trim) on the maneuvering force and the resultant course stability based on eigenvalue analysis, where the course stability tends to deteriorate as the ship's draft deepens or the trim by bow becomes larger. These characteristics can be confirmed from the results of the simulations. The red line shows the result of the PD control, where both the P and D gains were set to 1. In general, the derivative gain acts as a damper, and the oscillation is suppressed. Indeed, the heading angles in D-EK and TB converge successfully.

In conclusion, it becomes difficult for the operator to maneuver the ship in a deep-draft condition (D-EK) or in a trim-by-bow condition (TB). However, it seems possible to maneuver the ship stably by considering a derivative control, that is, quick and sensitive steering against the disturbance of motions, so that the overshoot angle is suppressed, and the ship can run on the target course smoothly.

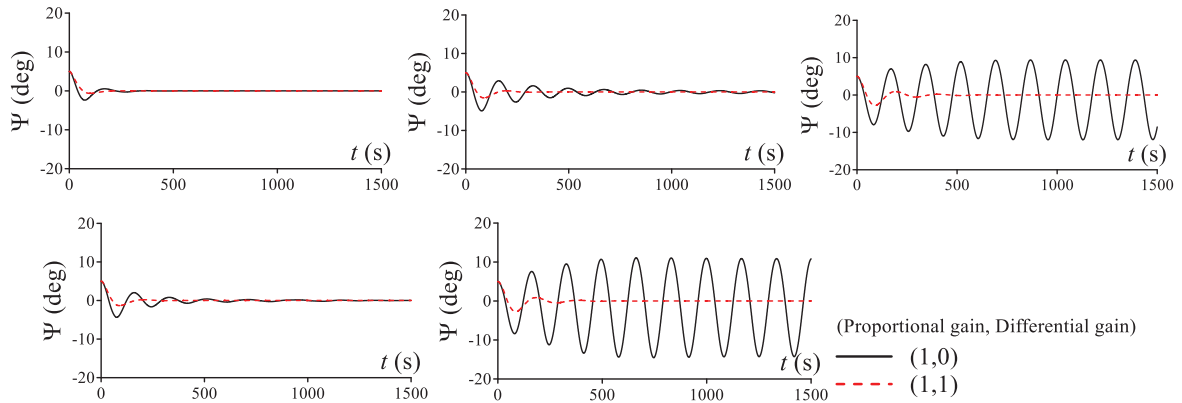


Figure 8.1: Influence of the rudder control gains on the convergence of the heading angle when keeping the course under no true wind

8.2 Influence of the ship speed and true wind angle

EK under true wind conditions is focused on. The black line in Figure 8.2 shows the result of the course-keeping simulation where the ship with $\psi_0=5^\circ$ attempted to maintain the course through PD control while running at $U_0=24$ (kt) under the wind condition of $U_w=9.26$ (m/s) and $\psi_w=90^\circ$. Both the proportional and derivative gains were set to one. Owing to its high speed, the rudder force seems enough to countermeasure the wind force. Thus, the initial disturbances of the motions converged smoothly. The red line represents the simulation results of the ship at $U_0=6$ (kt) which was assumed as the harbour speed, under the same wind conditions. Focusing on the yaw rate (r'), it takes a longer time for the initial disturbance to converge because the rudder force becomes small owing to the small inflow velocity when moving at the slow speed of the ship. The rudder angle (δ) and hull drift angle (β) also increased after their convergence. The roll angle (ϕ) when running at 24 (kt) was larger than 6 (kt), which may be due to the larger roll moment induced by the wind because of the faster apparent wind speed. The blue and green lines show the simulation results where $U_0=6$ (kt), $U_w=9.26$ (m/s) and $\psi_w=45^\circ$ and 135° , respectively. By comparing these lines and the red line, the influence of the true wind angle on the course-keeping performance can be discussed. Because of the heading wind when $\psi_w=45^\circ$,

the air drag increased with an increase in the apparent wind speed. Thus, a drop in the surge speed (u') and the resultant increase in the hull drift angle were observed. The opposite tendency was observed when $\psi_w=135^\circ$ where the wind blew to the ship from the behind, that is, following wind condition.

Notably, the heading and hull drift angles do not coincide. This indicates that the ship drifts downwind. To maintain a straight course without any deviation, PD control for the lateral displacement should be considered. This is discussed in detail in section 8.4.

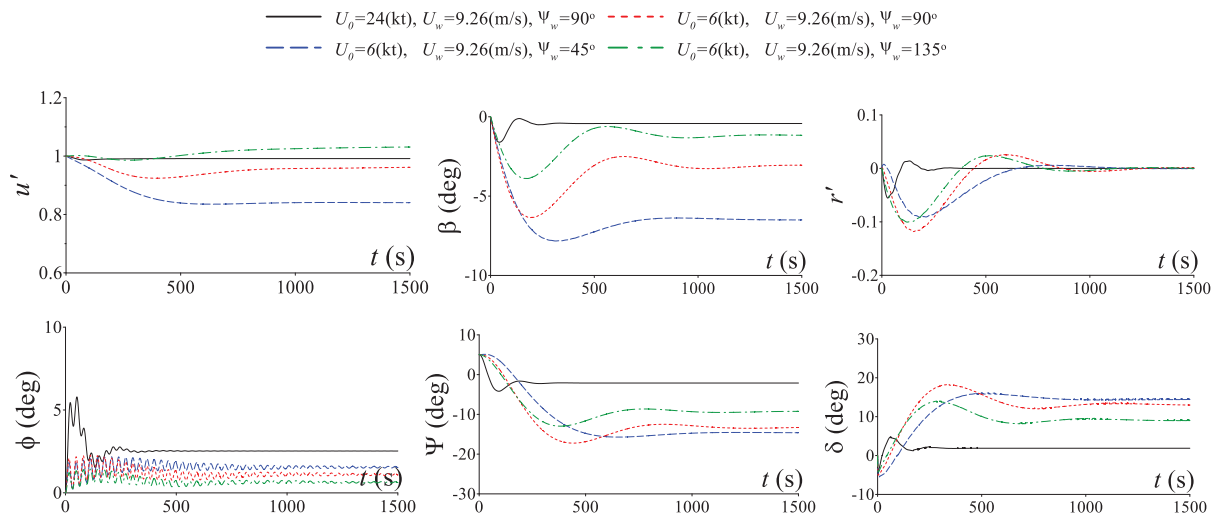


Figure 8.2: Influence of the ship speed and true wind angle on the states of EK when keeping the course under wind

8.3 Influence of trim and draft conditions

Figure 8.3 shows the results of the draft series, EK, S-EK, and D-EK, where they run at $U_0=6$ (kt) with $\psi_0=5^\circ$ under the wind condition, i.e., $U_w=9.26$ (m/s) and $\psi_w=90^\circ$, using both the proportional and derivative control gains 1. S-EK, which has a small windage area owing to the small number of containers, demonstrated a remarkable difference from EK and D-EK. D-EK, which has a larger displacement or inertia force, had larger oscillation in motion than EK.

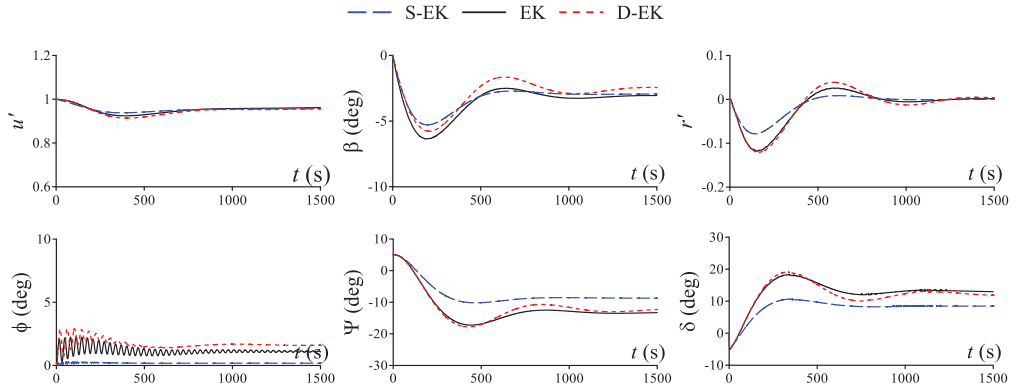


Figure 8.3: Comparison of the states while course keeping by PD control among the draft series, i.e., EK, S-EK and D-EK under wind; $U_w=9.26$ (m/s) and $\psi_w=90$ ($^\circ$)

Figure 8.4 shows the results of the trim series, EK, TB, and TS, in the same situation as that in Figure 8.3. The oscillation of the motions is larger in TB, which is characterized as a loading condition with unstable course stability. The yaw angular velocity increased quickly, and the resultant motions tended to be overshoot. This indicates that sensitive steering against the ship motions, which implies an increase in the derivative control gain, is important for steady navigation. Compared to D-EK, which also has unstable course stability, the large roll motion continues longer in TB. This is because the submerged hull of TB is smaller than that of D-EK, causing a small damping of the roll motion. When the ship takes the trim by bow, such unstable course stability and large continuous roll motions should be carefully considered.

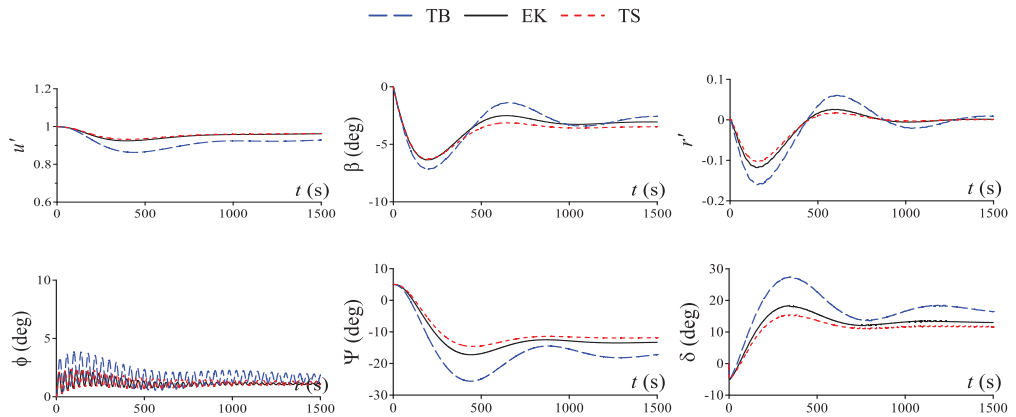


Figure 8.4: Comparison of the states while course keeping by PD control among the trim series, i.e., EK, TB and TS under wind; $U_w=9.26$ (m/s) and $\psi_w=90$ ($^\circ$)

8.4 PD control designed to maintain the straight course

As discussed in Section 8.2, the autopilot based on PD control for yaw motion cannot stop drifting downwind under wind pressure. Therefore, to maintain a straight course, PD control for the lateral displacement must be additionally considered. As an example, Figure 8.5 shows the states of EK while performing course keeping by the PD control with and without considering the feedback gains for the lateral displacement and its time derivative, that is, the lateral velocity. The initial conditions were $\psi_0=5^\circ$ and $U_0=6$ (kt), and wind conditions were $U_w=9.26$ (m/s) and $\psi_w=90^\circ$.

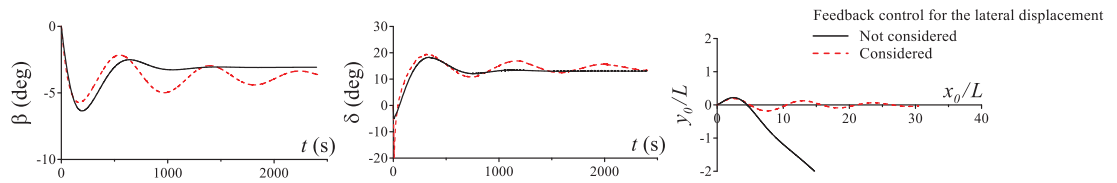


Figure 8.5: Comparison of the hull drift angle, rudder angle and trajectory of EK while course keeping by the PD control for yaw motion (in black) and the PD control for yaw and lateral displacement (in red) under wind; $U_w=9.26$ (m/s) and $\psi_w=90^\circ$

In the case of no consideration, that is, the PD control only for yaw motion with control gains of 1, the ship's track gradually deviated from the original course (the x -axis). On the other hand, in the case of consideration, that is, the PD control for yaw and lateral displacement whose gains were tuned properly, the ship was able to maintain a straight course through steering dynamically. The resultant hull drift angle appears to be larger than that in the case without consideration.

8.5 Equilibrium state under wind

An equilibrium state under wind is defined as the steady state while maintaining an original straight course without any deviation, wherein every external force and moment are balanced. The check helm angle (rudder angle), hull drift angle, and roll angle in the equilibrium state were identified based on course-keeping simulations. The PD control for yaw and lateral displacement was considered so as to avoid deviation from the original course. Each control gain was tuned for this purpose.

8.5.1 Influence of the apparent wind speed under the constant ship speed

EK sailing at a constant speed of $U_0=6$ (kt), assuming navigation near a coast or harbour, was considered. At such a slow speed, the influence of the wind on the ship's maneuverability is relatively strong. Figure 8.6 shows the check helm (δ_{0w}), hull drift (β_{0w}) and roll angles (ϕ_{0w}) in the equilibrium state with respect to the apparent wind angle from 0° to 180° . The three lines in each subfigure represent the results of the different ratios of the apparent wind speed to the ship speed, that is, 1, 2, and 3. For example, in the case of $U_{aw}/U_0 = 3$, the true wind speed (U_w) is equivalent to the Beaufort scale (BF) from 4 to 6, that is, a moderate breeze (BF4) at $\psi_{aw} = 0^\circ$ and strong breeze (BF6) at $\psi_{aw} = 180^\circ$.

The result of $U_{aw}/U_0 = 1$ indicates that each angle required for course keeping increases when the apparent wind blows against the hull from the side. Their angles drastically increase with an increase in the apparent wind speed; for example, in the case of $U_{aw}/U_0 = 3$ and $\psi_{aw} = 90^\circ$, the check-helm angle is 13.8° , in spite of only 1.4° in the case of $U_{aw}/U_0 = 1$ and the same ψ_{aw} as above. Particularly, the largest check-helm angle is required at approximately $\psi_{aw}=125^\circ$. As shown in Figure 3.6, a lateral wind force exhibits a positive peak around this wind angle, which causes the ship to drift away in the starboard direction (see the coordinate system in Figure 2.1). Additionally, a large negative moment in yaw caused by the wind causes the ship to turn in the counterclockwise direction. Thus, the ship requires a large positive check helm angle which moves it in the port direction, and a clockwise moment to maintain balance.

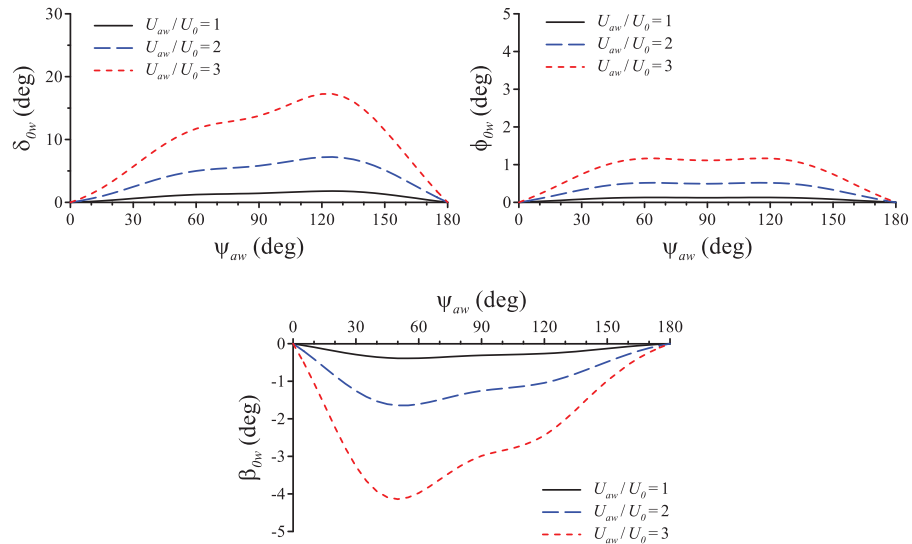


Figure 8.6: Equilibrium states of EK sailing at $U_0=6$ (kt) under different apparent wind speeds, i.e., $U_{aw}/U_0=1, 2, 3$

However, the absolute hull drift angle shows the largest angle around $\psi_{aw} = 50^\circ$ at which the large lateral wind force to the starboard and clockwise wind moment act on the ship. To reduce the starboard movement, a positive rudder angle is required to generate a rudder force in the port direction. Because the direction of the yaw moment due to the rudder force is clockwise and in the same direction as that due to the wind force, the ship must take negative oblique towing to cancel these yaw moments by the hydrodynamic yaw moment acting on the hull. Therefore, the peak of the hull drift angle appeared around this apparent wind angle.

The roll angle in the equilibrium state did not exhibit a significant peak. Eq. (2.2) signifies that it is influenced by the rudder force (Y_R), which correlates with the rudder angle and reaches a maximum around $\psi_{aw}=125^\circ$, and the hull force (Y_H), which correlates with the hull drift angle and takes a maximum value around $\psi_{aw}=50^\circ$. Because the apparent wind angle around which Y_H and Y_R peak does not overlap, the roll angle tends to be flat without any significant peaks and takes a small value overall.

8.5.2 Influence of the ship speed under the constant apparent wind speed

Assuming the apparent wind speed to be constant, $U_{aw}=9.26$ (m/s), the equilibrium states of EK at ship speeds of $U_0=6, 12,$ and 24 (kt) are shown in Figure 8.11, where the apparent wind angle is taken as the horizontal axis. Notably, the results for $U_0=6$ (kt) are the same as those for $U_{aw}/U_0 = 3$ in Figure 8.7.

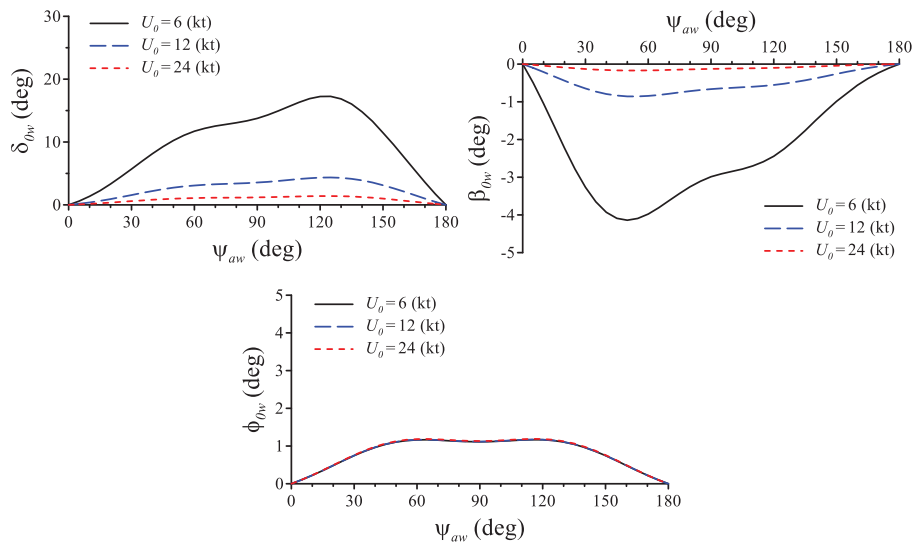


Figure 8.7: Equilibrium states of EK sailing at different ship speeds, i.e., 6, 12, 24(kt), under the apparent wind speed, i.e., $U_{aw}=9.26$ (m/s)

When the ship speed is high, the check-helm angle becomes significantly smaller. This appears to be because the propeller rotation speed for self-propelling increases when the ship speed is high. This caused the flow speed at the rudder to be much faster, resulting in a larger rudder force. Similarly, the oblique angle was also affected by the speed of the ship. Because the hydrodynamic force acting on the hull increased as the ship speed increased, and even a small hull drift angle could be balanced by the wind moment. Meanwhile, the influence of the ship speed on the roll angle was not significant. This may be because the direction of the hull force, Y_H , and rudder force, Y_R , are opposite, and the increments of both forces associated with the increase in ship speed may cancel each other.

These results indicate that one must be careful of an expected large check helm and the ship's attitude for course keeping when navigating a harbor or coastal areas in which the ship speed is commonly slow. However, it is also possible to reduce these values by slightly increasing the ship speed under such circumstances. Thereby, a greater safety margin for maneuvering could be expected. If sailing at a navigation speed of 24 (kt), the ship is supposed to be able to maintain the course with a sufficiently small check helm and oblique angles under the wind conditions considered here.

The influence of the loading conditions on the equilibrium states was investigated. The apparent wind speed was assumed to be $U_{aw}=9.26$ (m/s), whereas the ship speed was $U_0=6$ (kt). The results of the draft series are arranged on the left, and those of the trim series are shown on the right in Figure 8.8.

8.5.3 Influence of loading condition under the constant ratio of the apparent wind and ship speeds

Focusing on the draft series, the check-helm angle of S-EK was smaller than that of EK. This resulted from the small windage area owing to the small number of containers, as shown in Figure 3.6. It seems that D-EK requires a slightly smaller check-helm angle than EK. Because of the deeper draft and larger drag, a higher propeller rotational speed, in which a larger rudder force is expected, is required for self-propelling. Thus, even a small check-helm angle may have been enough. The hull drift angles of S-EK and D-EK are smaller than those of EK. The reason for this difference can be discussed in the same way as above. The roll angle for course keeping under the same apparent wind angle seems to increase in the order of S-EK, EK, and D-EK. The significant small roll angle of S-EK is due to the large GM because of the low position of the

centre of gravity. On the other hand, the large roll angle of D-EK is due to the small GM, as listed in Table 3.5.

Focusing on the check helm angle in the trim-series condition, the ship with the trim by bow requires a larger check helm angle, that is, 22.5° in TB, 17.3° in EK, and 16° in TS around $\psi_{aw} = 125^\circ$. The author has presented the rudder force and resultant rudder moment increase in the order of TB, EK, and TS. They were correlated with the propeller rotation speed for self-propulsion, owing to their resistance and self-propulsive performance. Because TB runs at a lower propeller load, it needs to take a larger check helm angle to increase the rudder force to balance the wind force. In terms of the hull drift angle in the equilibrium state, TS had a larger absolute value overall. As discussed, because of the deep draft at the stern in TS, the acting point of the hull drift force, which is positioned at the fore of the hull, moves backward toward the midship. This results in a smaller yaw damping moment in oblique towing. Therefore, a large hull drift angle is required to balance the yaw moment caused by wind. Meanwhile, the influence of the loading conditions on the roll angle in the equilibrium state can be explained by the difference in the GM. In the case of TB, in which the draft at the stern is shallow, the hull shape around the stern underwater becomes thin, which results in a smaller 2nd moment of the water surface area than EK and TS. Because the radius of the metacenter is proportional to this moment of area, the vertical position of the metacenter is lower, resulting in the smaller GM. It caused the large roll angle of TB.

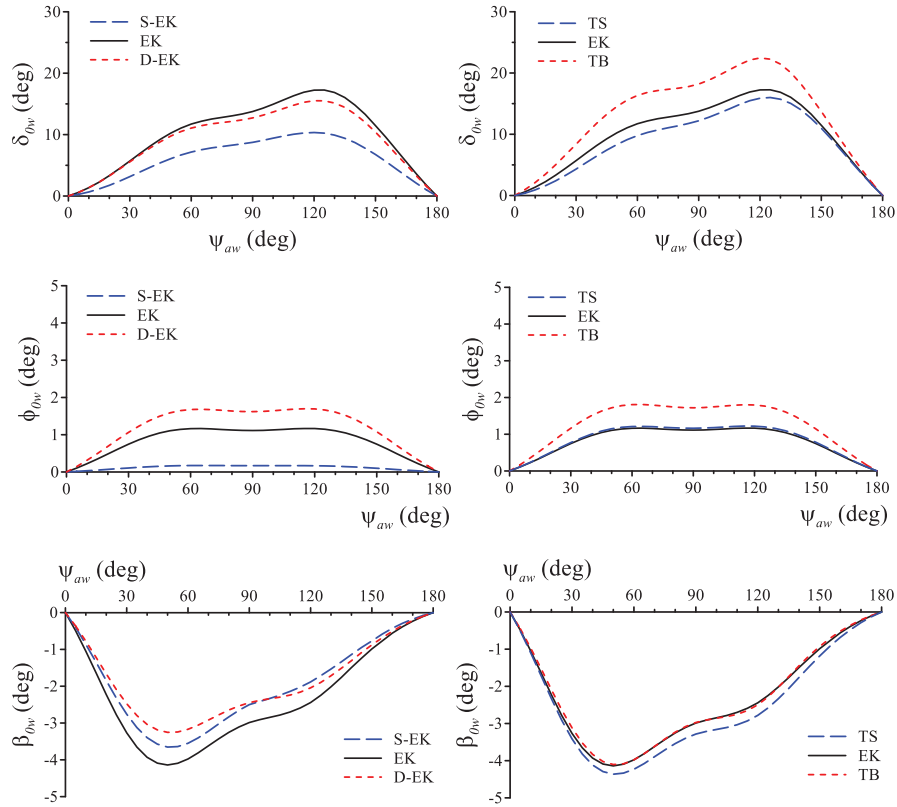


Figure 8.8: Equilibrium state of EK, S-EK and D-EK (draft series) and EK, TB and TS (trim series) sailing at $U_0=6$ (kt) under the same apparent wind speed, i.e., $U_{aw}=9.26$ (m/s) which corresponds to $U_{aw}/U_0 = 3$

8.5.4 Discussion of the equilibrium state based on the polar chart

Although discussions based on apparent wind, defined as the sum of head wind that a running ship faces and true wind, are useful for immediate knowledge, it may be difficult to know which direction the true wind blows against the ship and how fast the true wind blows. Therefore, in this section, a polar chart of the equilibrium state is illustrated based on the true wind direction and speed. This chart has the advantage of allowing users to intuitively grasp the relationship between their ship speed, true wind conditions, and the resultant equilibrium states of the ship. The results of the draft series are shown in Figure 8.19.

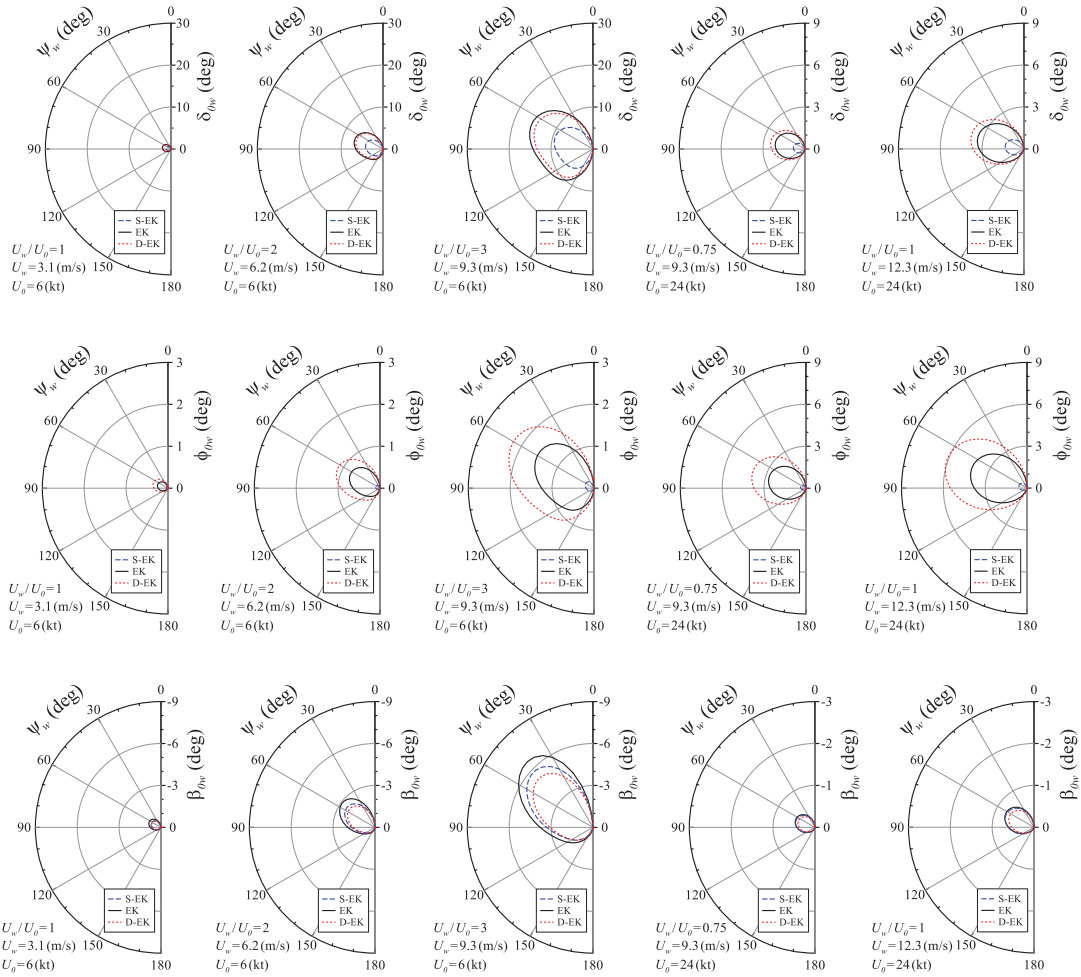


Figure 8.9: Polar chart of the equilibrium states of EK, S-EK and D-EK (draft series) in various combinations of the true wind and ship speed

The check helm, roll, and hull drift angles in the equilibrium state are plotted in polar charts, where the direction of the angle of the true wind is taken in the circumferential direction. The subfigures arranged in the 1st, 2nd, and 3rd columns show the results when the ship runs at $U_0=6$ (kt) under the wind condition in which the true wind speeds are $U_w=3.1, 6.2$ and 9.3 (m/s). These are equivalent to the ratio of the true wind speed to the ship speed, that is, $U_w/U_0=1, 2,$ and 3 . In these cases, the check helm angle becomes maximum when the true wind blows against the ship from diagonally forward, that is, around $\psi_w=70^\circ$. A similar trend is observed for every loading condition, and the order of magnitude of each absolute angle is the same as in the discussion in Figure 8.6. In the 4th column in Figure 8.7, the results of the condition where the ship speed is $U_0=24$ (kt) and the speed of the true wind is $U_w=9.3$ (m/s) are shown. The speed effect on the equilibrium state can be observed by comparing the results of the 3rd and 4th columns. With an increase in the ship speed, the ring size illustrated on the polar chart

significantly shrinks because of the expected larger rudder force, indicating that the ship could maintain the course with a small check-helm angle without a large change in the ship's attitude. The 5th column shows the results when the ship speed is $U_0=24$ (kt) and the true wind speed is $U_W=12.3$ (m/s). Notably, the only difference from the 4th column is the speed of the true wind blowing against the ship. Although the ring size increases, this ship could maintain its course at 24 (kt) even under a strong breeze (BF 6), regardless of the draft condition.

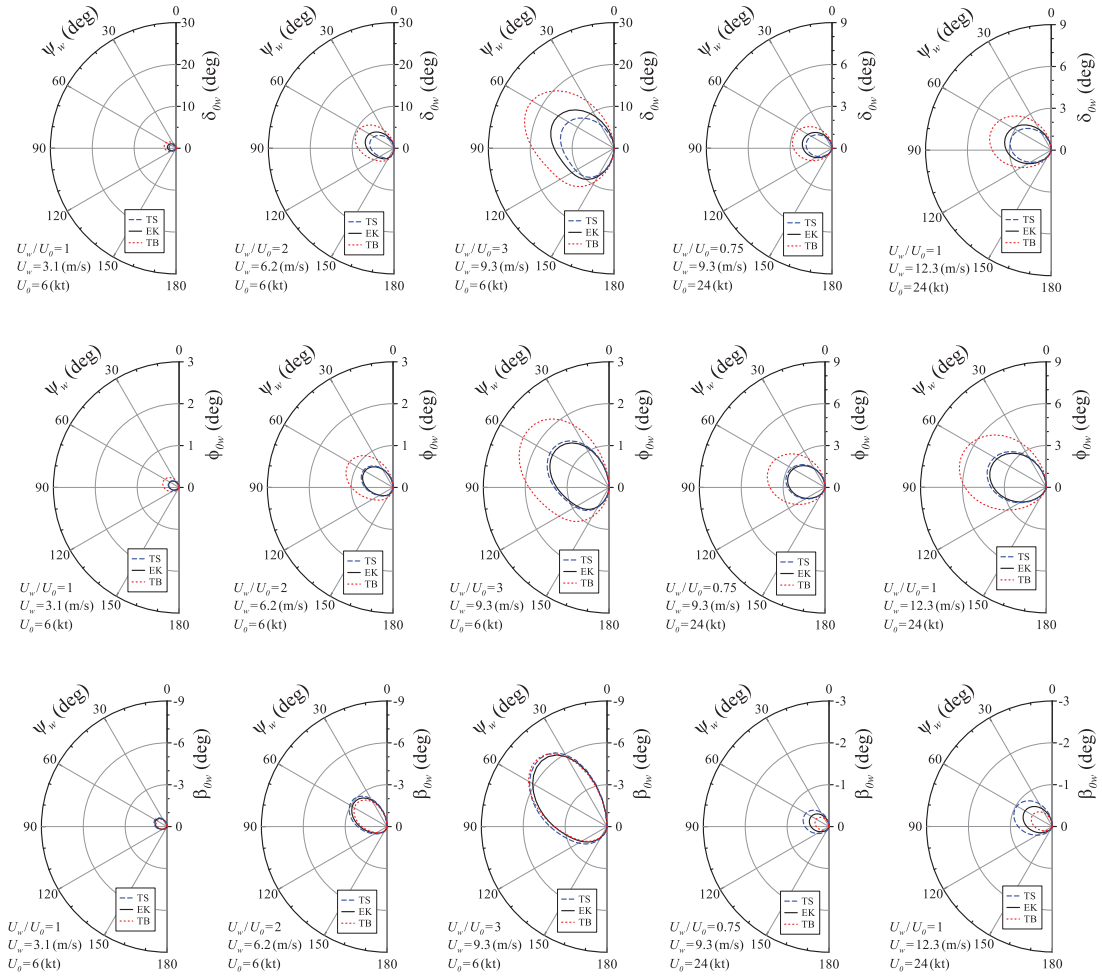


Figure 8.10: Polar chart of the equilibrium states of EK, TS and TB (trim series) in various combinations of the true wind and ship speed

Here, Figure 8.8 shows the results for the trim-series condition. Although the almost same consideration can be made as in Figure 8.19, a unique phenomenon was observed in the case of $U_W = 9.3$ (m/s) and $U_0 = 6$ (kt), only in which the ring size of the hull drift angle of TB was a large as that of TS. Because it is case of $U_W/U_0 = 3$ that the wind effect on the ship motions is stronger than other cases, the check helm angle increased overall. As can be seen from Figure

8.20, since TB tended to take a larger check helm angle than TS, the larger surge-speed drop was expected due to the larger steering drag, especially under such a strong wind. It caused the influence of the sway motion to be relatively large and resulted in the increase of the hull drift angle of TB.

Chapter 9

Conclusion

In this study, five loading conditions with different displacements (drafts) and trims of a container ship KCS were considered and the effect on those loading conditions on the ship's maneuverability were comprehensively analysed. Free-running maneuvering tests were conducted to investigate the turning, yaw-checking, and course stability performances. Captive model tests were performed to understand the differences in hydrodynamic force characteristics among different loading conditions. Especially, the course stability, which is the fundamental performance of ship navigation. Was discussed based on the hydrodynamic force data. CFD was also performed to analyse the mechanism for changes in course stability according to the loading conditions. They are concluded as follows.

- The turning diameter becomes smaller (i.e., turning ability improves) with an increasing draft or trim by the bow. The smaller turning diameter causes a larger OSA during zig-zag maneuvers. It indicates lower yaw-checking ability and course stability. These changes occur even if the change in the loading condition is not necessarily drastic.
- The course stability of the ship deteriorates with an increasing draft. A major factor was that the acting point of the sway force in the sway motion moved close to the bow. This was primarily attributed to the large positive pressure by incident fluid at the bow on the face-side, and the large negative pressure by the smooth accelerated flow around the fore shoulder of the hull on the backside. The latter was affected by the flow disturbance caused by the bulb.
- The course stability decreased in the trim order by the stern, even keel, and trim by the bow when the displacement was kept constant. This was attributed to the increase in the pressure-based sway force around the bow with increasing trim. The negative pressure distribution around the bilge on the face-side was also concerned with trim by the bow and its magnitude influenced the course stability.
- The tendencies and magnitude of the effects of loading conditions on the hydrodynamic forces and resultant course stability would depend on the ship foam. This is because the presence of the bulb or curvature of the hull surface sensitively affects the flow and pressure fields around the ship even when minor changes occur in the draft and trim. We intend to investigate other ships and conduct comprehensive analyses.

Besides, maneuvering simulations were performed using the MMG-model. A series of hydrodynamic force coefficients used for the simulation were captured by captive model tests. The main conclusion of the maneuvering simulation are as follows.

- Through comparison with the free-running test results, the maneuvering mathematical model of KCS was validated. The results of the simulation show good agreement with the free-running test results.
- The maneuvering motions in the real scale were conducted. Every model-scale dimension including the loading conditions was converted to the real-scale one, and the roll-motion characteristics were update for the real-scale ship. Mainly because the roll-motion characteristics became more realistic through the realistic design of the container arrangement, there were some difference in the maneuverability from the model ship one. As the conclusion, when the draft is deeper, or when the bow trim is attached to the ship, the controllability may deteriorate to the extent that the overshoot angle increases. The ship operator should be aware that the maneuverability of such a container ship changes due to the loading condition changes.

Finally, the loading conditions and wind effects on the course-keeping performance of KCS, were investigated. The windage section on the upper deck was designed under five loading conditions which had various draft and trim combinations, and the wind forces and moments acting on the ship were estimated. Based on the developed mathematical model, the course-keeping performance under wind was investigated by simulation. The following conclusions are obtained.

- The check helm angle under wind conditions, which is defined as the rudder angle required to maintain the specified course without deviation, was significantly different among the loading conditions. Meanwhile, the difference in the hull drift angle and roll angle in the equilibrium state was relatively small among them.
- In all cases, maintaining the specified course straight when a wind blew diagonally from behind was the most severe condition, wherein the largest check helm angle was required, and the steering margin was reduced.
- Among the trim-series conditions, the trim by bow required a larger check helm angle, while the trim by stern had a smaller angle. This is related to the essential course stability determined by the hydrodynamic water forces acting on the hull under each loading condition.

- A shallow-draft ship requires a significantly small check helm angle. This is because of the small windage area as well as the better course stability.
- An increase in ship speed is an effective way to reduce the check helm angle by increasing the rudder force.
- A polar chart of the equilibrium state was presented based on the true wind direction and speed. This type of chart has the advantage of allowing users to intuitively grasp the relationship between their ship speed, true wind conditions, and the resultant equilibrium states of the ship.

The recommendations for the future works include the following items.

- The CFD calculation was simplified through certain assumptions regarding some items such as heel effect and free surface that were considered to have few impacts on the course stability; thus, were omitted in this study. For future research, the CFD method will be advanced to discuss a variety of maneuvers, considering the omitted components for a more thorough analysis.
- More consideration at the service speed of approximately 24 kt will be necessary. The speed effect on the hydrodynamic force and maneuvering motions will be studied.

References

1. IMO: ANNEX 6 RESOLUTION MASC.137(76). 2002. Standard for Ship Maneuverability.
2. Delgado, A., Jensen, R.M., Janstrup, K., Rose, T.H., and Andersen, K.H. 2012. A constraint programming model for fast optimal stowage of container vessel bays. *Eur. J. Oper. Res.* 220(2), 251-261.
3. Chou, C.C., and Fang, P.Y., 2021. Applying expert knowledge to container ship stowage planning: an empirical study. *Maritime Economics & Logistics.* 23, 4-27.
4. Aye, W. C., Low, M. Y. H., Ying, H. S., Jing, H. W. and Min, Z., 2010. Visualization and simulation tool for automated stowage plan generation system. In: *Proceedings of the International Multiconference of Engineers and Computer Scientists 2010 (IMECS 2010) 2*, Hong Kong, pp.1013-1019.
5. Lyu, X., Tu, H., Xie, D. and Sun, J., 2018. On resistance reduction of a hull by trim optimization. *Brodogradnja.* 69(1), 1-13.
6. Sun, J., Tu, H., Chen, Y., Xie, D. and Zhou, J., 2016. A study on trim optimization for a container ship based on effects due to Resistance. *Journal of Ship Research.* 60(1), 30-47.
7. Gao, X., Sun, K., Shi, S., Wu, B. and Zuo, Z., 2019. Research on Influence of Trim on a Container Ship's Resistance performance. *Journal of Physics: Conference Series.* 1300, Article ID 012105.
8. Islam, H. and Soares, C. G., 2019. Effect of trim on container ship resistance at different ship speeds and drafts. *Ocean Engineering.* 183, 106-115.
9. Larsen, N. L., Simonsen, C. D., Nielsen, C. K., Holm, C. R., 2012. Understanding the physics of Trim. In: *Proceedings of the 9th Annual Green Ship Technology Conference*, Copenhagen, pp.1-10.
10. Hirata, H., Yasukawa, H., Ukita, H. 2012. Maneuvering full-scale trial of a ship with azimuth propellers to capture the trim effect. In: *Proc. The International Conference on Marine Simulation and Ship Maneuverability (MASRSIM'12)*, Singapore.
11. Reichel, M., Minchev, A. and Larsen, N. L., 2014. Trim Optimization - Theory and Practice. *The International Journal on Marine Navigation and Safety of Sea Transportation.* 8(3), 387-392.
12. Vasileva, A., 2015. Study of the effect of trim on ship powering performance. In: *Scientific Proceedings XXIII International Scientific-Technical Conference "trans & MOTAUTO '15"*, 3, 151-154.

13. Sogihara, N., Tsujimoto, M., Fukasawa, R. and Ohba, H., 2018. Investigation on trim optimization to enhance the propulsive performance of fine ships. *Journal of the Japan Society of Naval Architects and Ocean Engineers*.
14. Inoue, S., Hirano, M., Kijima, K. and Takashina, J., 1981. A practical calculation method of ship maneuvering motion. *International Shipbuilding Progress*. 28(325), 207-222.
15. Kijima, K., Katsuno, T., Nakiri, Y. and Furukawa, Y., 1990. On the manoeuvring performance of a ship with the parameter of loading condition. *Journal of The Society of Naval Architects of Japan*. 168, 141-148.
16. Kose, K., Sakamoto, M., Kobatake, Y., Hirao, S. and Wada, S., 1991. Studies on the effect of loading condition on the maneuverability of ships. *Transactions of the West-Japan Society of Naval Architects*. 82, 155-165 (in Japanese).
17. Sannomiya, K., Sueyoshi, A., Arihama, K., 2000. Effect on coefficient of manoeuvrability in difference of ship conditions. *Transactions of the West-Japan Society of Naval Architects*. 99, 103-113 (in Japanese).
18. Sannomiya, K., Sueyoshi, A., Arihama, K., 2001. Effect on coefficient of manoeuvrability in difference of ship conditions (follow-up report). *Transactions of the West-Japan Society of Naval Architects*. 101, 103-112. (in Japanese)
19. Suez Canal Incident. https://simple.wikipedia.org/wiki/2021_Suez_Canal_incident. (Accessed in December 2022).
20. Zhou, Y., Daamen, W., Vellinga, T., Hoogendoorn, S.P. 2020. Impacts of wind and current on ship behavior in ports and waterways: A quantitative analysis based on AIS data. *Ocean Eng.* 213, 107774.
21. Yoshimura, Y., Nagashima, J. 1985. Estimation of the maneuvering behaviour of ship in uniform wind. *J. Soc. Nav. Archit. Jpn.* 158, 125–136. (in Japanese)
22. Hasegawa, K., Kang, D.H., Sano, M., Nagarajan, V., Yamaguchi, M. 2006. A study on improving the course-keeping ability of a pure car carrier in windy conditions. *J. Mar. Sci. Technol*, 11, 76–87.
23. Nagarajan, V., Kang, D.H., Hasegawa, K., Nabeshima, K. 2008. Comparison of the mariner Schilling rudder and the mariner rudder for VLCCs in strong winds. *J. Mar. Sci. Technol*, 13, 24–39.
24. Paroka, D., Muhammad, A.H., Asri, S. 2016. Maneuverability of ships with small draught in steady wind. *Makara J. Technol.*, 20, 24–30.
25. Im, N.K.; Tran, V.L. 2008. Ship's maneuverability in strong wind. *J. Navig. Port Res. Int.* Ed, 32, 115–120.

26. Lee, C.K., Lee, S.G. 2007. Hydrodynamic forces between vessels and safe maneuvering under wind-effect in confined waters. *J. Mar. Sci. Technol.*, 21, 837–843.
27. Silva, A.S., Oleinik, P.H., Kirinus, E.P., Costi, J., Guimaraes, R.C., Pavlovic, A., Marques, W.C. 2019. Preliminary study on the contribution of external forces to ship behavior. *J. Mar. Sci. Eng.*, 7, 72.
28. Andersen, I.M.V. 2013. Wind loads on post-panamax containership. *Journal of Ocean Eng.* 58, 115–134.
29. Janssen, W.D., Blocken, B., Wijhe, H.J. 2017. CFD simulations of wind loads on a container ship: Validation and impact of geometrical simplifications. *J. Wind. Eng. Ind. Aerodyn.*, 166, 106–116.
30. Seok, J., Park, J.C. 2020. Comparative study of air resistance with and without a superstructure on a container ship using numerical simulation. *J. Mar. Sci.*, 8, 267.
31. Fujiwara, T., Ueno, M., Ikeda, Y. 2005. A new estimation method of wind force and moments acting on ships on the basis of physical component models. *Journal of Japan Society of Naval Architect, Ocean Engineering.* 2, 243-255. (in Japanese).
32. ITTC Quality System Manual – Recommended Procedures and Guidelines: Preparation, Conduct and Analysis of Speed/ Power Trials. Available online: <https://itc.info/media/98-74/75-04-01-011.pdf> (accessed on 9 April 2023).
33. FORCE Technology and Iowa Institute of Hydraulic Research (IIHR). 2008. Part B: benchmark test cases, KCS description. In: *Proceedings of the Workshop on Verification and Validation of Ship Maneuvering Simulation Methods. (SIMMAN2008)*, pp. B11-B14. Copenhagen.
34. Matsuda, A., Hashimoto, H., Terada, D., and Taniguchi, Y., 2016. Validation of free running model experiments in heavy seas. In: *Proceedings of the 3rd International Conference on Violent Flows*, Kobe.
35. Hasnan, M. A. A., Yasukawa, H., Hirata, N., Terada, D. and Matsuda, A., 2020. Study of ship turning in irregular waves. *Journal of Marine Science and Technology*, 25(4), 1024-1043.
36. Yasukawa, H. and Sano, M. 2008. Maneuvering simulation of MOERI container ship. In: *Proceedings of the Workshop on Verification and Validation of Ship Manoeuvring Simulation Methods (SIMMAN2008)*, Copenhagen, pp. E68-E73.
37. Yasukawa, H., Suzuki, T., Yoshimura, Y. 2020. Turning of a heeled ship. *J. Jpn. Soc. Nav. Archit. Ocean Eng.* 32; 35-46.
38. Bertram, V. 2000. *Practical ship hydrodynamics*. Butterworth-Heinemann, Oxford.

39. Yoshimura, Y., Nomoto, K. 1978. Modelling of manoeuvring behaviour of ships with a propeller idling, boosting, and reversing. *Journal of Society of Naval Architect, Japan.* 144:57-69. (in Japanese)
40. Nomoto, K. 1960. Analysis of kempf's standard maneuver test and proposed steering quality indices. *Proceedings of 1st Symposium on Ship Maneuverability*, pp. 275-304.
41. Inoue, S., Hirano, M., Kijima, K. 1981. Hydrodynamic derivatives on ship manoeuvring, *International Shipbuilding Progress.* 28(321), 112-125.
42. Yasukawa, H., Yoshimura, Y. 2014. Roll-coupling effect on ship maneuverability. *Ship Technol. Res* 61(1):16-32.
43. The open source CFD toolbox. OpenFOAM. The OpenFOAM foundation. <http://openfoam.org/>. (Accessed 30 April 2021)
44. Chen, J., Zou, Z.J., Chen, X., Xia, L., Zou, L. 2017. CFD-based simulation of the flow around a ship in turning motion at low speed. *Journal of Marine and Science Technology.* 22, 784-796.
45. Menter, F.R., Kuntz, M., Langtry, R., 2003. Ten years of industrial experience with the SST turbulence model. *Turbulence, Heat and Mass Transfer* 4, 625-635.
46. Yamazaki, R. 1998. Deduction of the simplified propeller theory. In: *Transactions of West-Japan Society of Naval Architects.* Vol. 95, pp. 251-271. (in Japanese)
47. Ohashi, K., Hirata, N., Hino, T. 2003. A comparative study of body force models representing effects of contrarotating propellers. In: *Transactions of West-Japan Society of Naval Architects*, vol. 105, pp. 55-64.
48. ITTC. 2017. 1978 ITTC Performance Prediction Method. *ITTC Quality System Manual - Recommended Procedures and Guidelines-*. 7.5-02-03-01.4, Revision 04.
49. Yasukawa, H., Kawamura, S., Tanaka, S., Sano, M. 2009. Evaluation of ship-bank and ship-ship interaction forces using a 3D panel method. In: *International Conference on Ship Maneuvering in Shallow and Confined Water, Bank Effects*, Antwerp, Belgium, pp. 127-133.
50. Yasukawa, H., Sakuno, R., Yoshimura Y. 2019. Practical maneuvering simulation method of ships considering the roll-coupling effect. *J Marine Sci Technol* 24(4):1280-1296.
51. Yoshimura, Y. 1984. Mathematical model for the manoeuvring ship motion in shallow water. *Journal of Kansai Society of Naval Architect Japan*, 200: 41-51. (in Japanese).

Appendix A

Formula to estimate hull hydrodynamic force derivatives

Inoue's formula [41] is known as a simple method for estimating the linear hydrodynamic derivatives with respect to the ship hull. Here, to verify the estimation accuracy of Inoue's formula, the linear derivatives calculated using the formula are compared with the present captive model test results. Inoue's formula predicts the linear hydrodynamic derivatives ($Y'_v, Y'_r, N'_{v0}, N'_{r0}$) from the principal particulars of the ship, and in the case of even keel condition, this is expressed as follows:

$$\left. \begin{aligned} Y'_{v0} &= -0.5\pi k - 0.7m' \\ Y'_{r0} &= 0.25\pi k \\ N'_{v0} &= -k \\ N'_{r0} &= -0.54k + k^2 \end{aligned} \right\} \quad (\text{A.1})$$

When trim is added, Eq. 1 becomes:

$$\left. \begin{aligned} Y'_v &= Y'_{v0}(1 + 0.67\tau') \\ Y'_r &= Y'_{r0}(1 + 0.8\tau') \\ N'_v &= N'_{v0} - 0.27\tau'Y'_{v0} \\ N'_r &= N'_{r0}(1 + 0.3\tau') \end{aligned} \right\} \quad (\text{A.2})$$

where $k = 2d_m/L$, and $\tau' = \tau/d_m$ where τ represents the trim amount, and the stern is positive. m' is defined as $m' \equiv m/((1/2)\rho L^2 d_m)$ and is the non-dimensionalized mass coefficient of the ship. The advantage of this expression is its simplicity; the derivatives can be determined using only the three parameters of k , τ' , and m' . It should be noted that derivatives of yaw moment (N'_v, N'_r) are defined about the midship.

Appendix B

Formula to estimate wind forces and moments acting on hull

An estimation equation of wind forces and moment acting on ship is adapted from Fujiwara et al. [31].

The fundamental equations based on attack angle ψ defined as follows:

$$X_A = X_0 + X_1 \cos\psi + X_3 \cos 3\psi + X_5 \cos 5\psi \quad (\text{B.1})$$

$$Y_A = Y_1 \sin\psi + Y_3 \sin 3\psi + Y_5 \sin 5\psi \quad (\text{B.2})$$

$$N_A = N_1 \sin\psi + N_2 \sin 2\psi + N_3 \sin 3\psi \quad (\text{B.3})$$

$$N_A = K_1 \sin\psi + K_2 \sin 2\psi + K_3 \sin 3\psi + K_5 \cos 5\psi \quad (\text{B.4})$$

Each term on X_A is expressed as follows;

$$X_0 = x_{00} + x_{01} \frac{BH_{BR}}{A_T} + x_{02} \frac{C}{H_c} + x_{03} \frac{A_{0D}}{L^3} \quad (\text{B.5})$$

$$X_1 = x_{10} + x_{11} \frac{A_L}{LB} + x_{12} \frac{LH_c}{A_L} + x_{13} \frac{LH_{BR}}{A_L} + x_{14} \frac{A_{0D}}{A_L} + x_{15} \frac{A_T}{LB} + x_{16} \left(\frac{A_T}{L^2}\right)^{-1} + x_{17} \left(\frac{H_c}{L}\right)^{-1} \quad (\text{B.6})$$

$$X_3 = x_{30} + x_{31} \left(\frac{LH_{BR}}{A_L}\right)^{-1} + x_{32} \frac{A_L}{A_T} + x_{33} \frac{LH_c}{A_L} + x_{34} \frac{A_{0D}}{A_L} + x_{35} \frac{A_{0D}}{L^2} + x_{36} \frac{C}{H_c} + x_{37} \frac{C_{BR}}{L} \quad (\text{B.7})$$

$$X_5 = x_{50} + x_{51} \left(\frac{A_{0D}}{A_L}\right)^{-1} + x_{52} \frac{C_{BR}}{L} + x_{53} \frac{A_L}{LB} \quad (\text{B.8})$$

Each term on X_A is expressed as follows;

$$Y_1 = y_{10} + y_{11} \frac{C_{BR}}{L} + y_{12} \frac{C}{L} + y_{13} \left(\frac{A_{0D}}{A_L}\right)^{-1} + y_{14} \frac{C}{H_c} + y_{15} \left(\frac{BH_{BR}}{A_T}\right)^{-1} \quad (\text{B.9})$$

$$Y_3 = y_{30} + y_{31} \frac{A_L}{LB} + y_{32} \frac{LH_c}{A_L} + y_{33} \frac{C_{BR}}{L} + y_{34} \left(\frac{H_{BR}}{B}\right)^{-1} + y_{35} \frac{A_{0D}}{A_L} + y_{36} \left(\frac{BH_{BR}}{A_T}\right)^{-1} \quad (\text{B.10})$$

$$Y_5 = y_{50} + y_{51} \frac{A_L}{LB} + y_{52} \left(\frac{H_{BR}}{L}\right)^{-1} + y_{53} \frac{C_{BR}}{L} + y_{54} \left(\frac{A_T}{B^2}\right)^{-1} + y_{55} \frac{C}{L} + y_{56} \frac{LH_c}{A_L} \quad (\text{B.11})$$

Each term on N_A is expressed as follows;

$$N_1 = n_{10} + n_{11} \frac{C}{L} + n_{12} \frac{LH_C}{A_L} + n_{13} \left(\frac{A_L}{A_T} \right)^{-1} + n_{14} \frac{C}{H_C} + n_{15} \frac{A_L}{LB} + n_{16} \frac{A_T}{L^2} + n_{17} \left(\frac{A_T}{B^2} \right)^{-1} + n_{18} \frac{C_{BR}}{L} \quad (\text{B.12})$$

$$N_2 = n_{20} + n_{21} \frac{C_{BR}}{L} + n_{22} \frac{C}{L} + n_{23} \left(\frac{A_{0D}}{A_L} \right)^{-1} + n_{24} \frac{A_T}{B^2} + n_{25} \left(\frac{H_{BR}}{L} \right)^{-1} + n_{26} \left(\frac{BH_{BR}}{A_T} \right)^{-1} + n_{27} \frac{A_L}{LB} + n_{28} \frac{A_L}{L^2} \quad (\text{B.13})$$

$$N_3 = n_{30} + n_{31} \frac{C_{BR}}{L} + n_{32} \left(\frac{BH_{BR}}{A_T} \right)^{-1} + n_{33} \frac{A_L}{A_T} \quad (\text{B.14})$$

Each term on K_A is expressed as follows;

$$K_1 = k_{10} + k_{11} \frac{H_{BR}}{L} + k_{12} \frac{A_T}{LB} + k_{13} \frac{LH_C}{A_L} + k_{14} \frac{C}{L} + k_{15} \frac{C_{BR}}{L} + k_{16} \left(\frac{H_{BR}}{B} \right)^{-1} + k_{17} \left(\frac{A_T}{B^2} \right)^{-1} + k_{18} \left(\frac{B}{L} \right)^{-1} \quad (\text{B.15})$$

$$K_2 = k_{20} + k_{21} \left(\frac{H_{BR}}{B} \right)^{-1} + k_{22} \frac{A_T}{B^2} + k_{23} \left(\frac{LH_C}{A_L} \right)^{-1} + k_{24} \frac{C_{BR}}{L} + k_{25} \frac{H_{BR}C}{A_L} + k_{26} \left(\frac{B}{L} \right)^{-1} + k_{27} \left(\frac{A_L}{L^2} \right)^{-1} \quad (\text{B.16})$$

$$K_3 = k_{30} + k_{31} \left(\frac{A_T}{B^2} \right)^{-1} + k_{32} \frac{C_{BR}}{L} + k_{33} \frac{H_C}{L} + k_{34} \frac{A_T}{LB} + k_{35} \left(\frac{A_L}{LB} \right)^{-1} + k_{36} \frac{A_{0D}}{L^2} \quad (\text{B.17})$$

$$K_5 = k_{50} + k_{51} \left(\frac{LH_C}{A_L} \right)^{-1} + k_{52} \left(\frac{A_{0D}}{A_L} \right)^{-1} + k_{53} \left(\frac{A_L}{A_T} \right)^{-1} + k_{54} \left(\frac{B}{L} \right)^{-1} + k_{55} \frac{A_L}{LB} \quad (\text{B.18})$$

The coefficient such as $x_{00}, x_{01}, y_{11}, n_{12}, k_{20}$, etc., are listed in Table 1. Below

Table B.1: Each coefficient for every variable

m=		0	1	2	3	4	5	6	7	8
X_A	x_{0m}	-0.330	0.293	0.0193	0.682					
	x_{1m}	-1.353	1.700	2.87	-0.463	-0.570	-6.640	-0.0123	0.0202	
	x_{3m}	0.830	-0.413	-0.0827	-0.563	0.804	-5.67	0.0401	-0.132	
	x_{5m}	0.0372	-0.0075	-0.103	0.0921					
Y_A	y_{1m}	0.684	0.717	-3.22	0.0281	0.0661	0.298			
	y_{3m}	-0.400	0.282	0.307	0.0519	0.0526	-0.0814	0.0582		
	y_{5m}	0.122	-0.166	-0.0054	-0.0481	-0.0136	0.0864	-0.0297		
N_A	n_{1m}	0.299	1.71	0.183	-1.09	-0.0442	-0.289	4.24	-0.0646	0.0306
	n_{2m}	0.117	0.123	-0.323	0.0041	-0.166	-0.0109	0.174	0.214	-1.06
	n_{3m}	0.0230	0.0385	-0.0339	0.0023					
K_A	k_{1m}	3.63	-30.7	16.8	3.270	-3.03	0.552	-3.03	1.82	-0.224
	k_{2m}	-0.480	0.166	0.318	0.132	-0.148	0.408	-0.0394	0.0041	
	k_{3m}	0.164	-0.170	0.0803	4.92	-1.780	0.0404	-0.739		
	k_{5m}	0.449	-0.148	-0.0049	-0.369	-0.0109	-0.0726			